solidify completely to δ but the volume fraction of austenite at ambient temperature is different for each case and increases with the nitrogen content. The austenite content can vary considerably with slight variations in composition [42].

3.4.2 Cooling rate

The effect of cooling rate on the weld microstructure has been approached in different ways. Van-Nasua [43] recommended that the welding conditions should be controlled to ensure a cooling time between 800 and 500°C $\Delta t_{(800-500°C)}$ of between 8-30 seconds, the upper limit imposed to minimise carbides and other precipitation reactions, and the lower limit to ensure that the δ to γ transformation is not suppressed. But in reality, the δ to γ reaction occurs at much higher temperatures and it has consequently been suggested [44] that a critical cooling time $\Delta t_{(1200-800°C)}$ should be defined instead over a temperature range of 1200-800°C. It has also been suggested that if the $\Delta t_{(1200-800°C)}$ is short enough it will suppress γ formation significantly, sometimes giving a single phase ferritic weld deposit and a very narrow heat affected zone. Duplex stainless steels are prone to grain coarsening after the complete dissolution of austenite at high temperatures since there is then nothing to prevent grain growth. Increased arc energy in welding is expected to increase the time that the weld deposit experiences at a temperature above 1200°C so that the tendency towards the development of a coarse HAZ grain macrostructure increases [28].

The effect of heat input on cooling time$\Delta t_{(1200-800°C)}$ as measured experimentally for duplex stainless steel weld metals for different welding processes (Table 3.2) is shown in Fig 3.9. The cooling time $\Delta t_{1200-800°C}$ increases with higher heat inputs, which results in coarser columnar grains [45].

3.4.3 Effects of nitrogen and carbon on weld microstructure

Investigations [46] of the effects of carbon and nitrogen on welds made on the surfaces of duplex stainless alloys with increasing C and N contents, using the tungsten inert gas process without the use of filler metal, reveals that the increase of

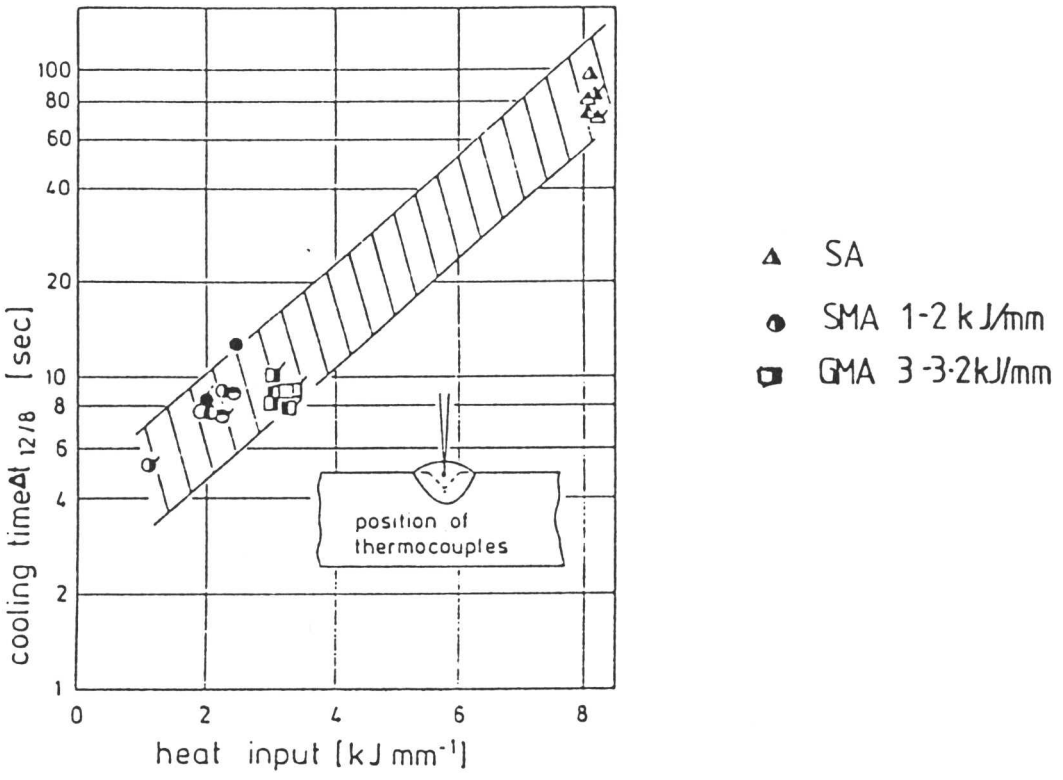

Fig. 3.9: The effect of heat input on $\Delta t_{1200-800°C}$ cooling time of austenitic and duplex stainless steel weld metals [45]. Welding processes, welding parameters and material compositions are shown in Table 3.2.

Table 3.2: After ref. [45], composition in wt.%.

Process	Material	C	Si	Mn	P	S	Cr	Ni	T^*_{mm}
	X8CrNiMo 27 5♣	.04	.46	1.55	0.03	0.016	26.0	4.9	32
	X5CrNi 18 9	.07					17.9	9.5	
	21/10 E	.01					22.0	10.0	5
	L 25/14	.01					24.5	14.0	5
SMA	L 25/4	.12					25.6	5.8	5
	30/10	.10					28.9	10.0	5
	C 25/20	.12					26.3	20.5	5
	21/10 E	.02					21.9	9.8	1.6
GMA	25/14 E	0.02	.35	1.87			23.6	13.6	1.6
	L 25/4	.07	.63	.71			25.8	4.9	1.6
	30/10	.10	.32	1.76			29.3	9.0	1.6
	21/10 E	.02	.50	1.47			21.6	10.8	4
SA	25/14 E	0.02	1.1	1.27			24.5	14.2	4
	30/10	.11	.56	1.48			30.4	9.4	4

Process	current (A)	voltage (V)	WS (cm/min)
SMA	200	28	13 – 28
GMA	250 – 275	30 – 29	15
SA	475	27	9.4

♣ =Mo concentration is 1.5, *= plate thickness and WS = welding speed.

carbon content from 0.017 wt.% to 0.4 wt.% results in a change from fully ferritic to fully austenitic microstructure at room temperature for constant welding and cooling conditions. It also increases the δ-eutectoid precipitation. Above 0.35 wt.% C, eutectic carbide $Cr_{23}C_6$ occurs due to microsegregation of Cr during solidification. The same effect was produced by nitrogen, starting with a fully ferritic structure at 0.002 wt.% N, a complete breakdown to austenite was achieved at 0.6 wt.% N. Such a high content of N causes porosity as a result of supersaturation. The effect of C and N on δ-ferrite content and the grain size of weld metal is shown in Fig 3.10.

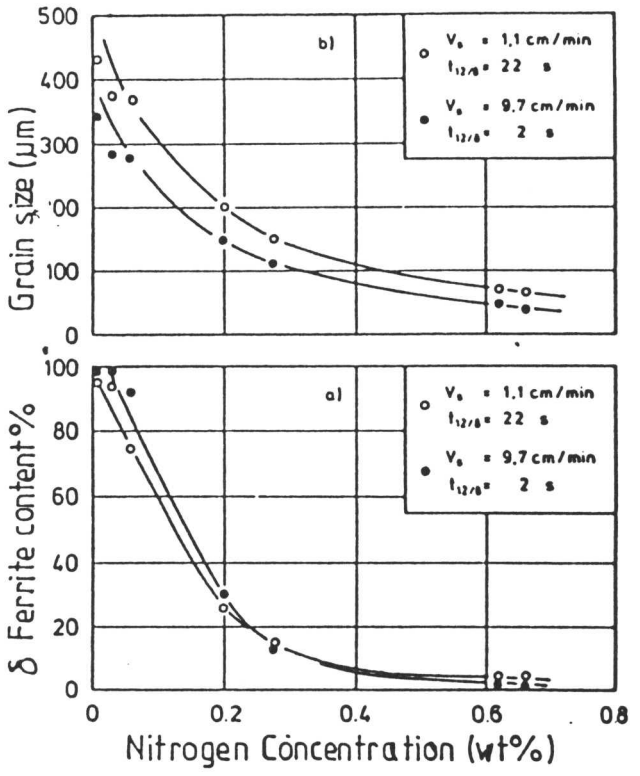

Fig. 3.10 a: Influence of nitrogen on δ-ferrite content and primary grain size of TIG weld metal (bases composition $\approx$ 24.4 Cr, 7 Ni wt.%), [46].

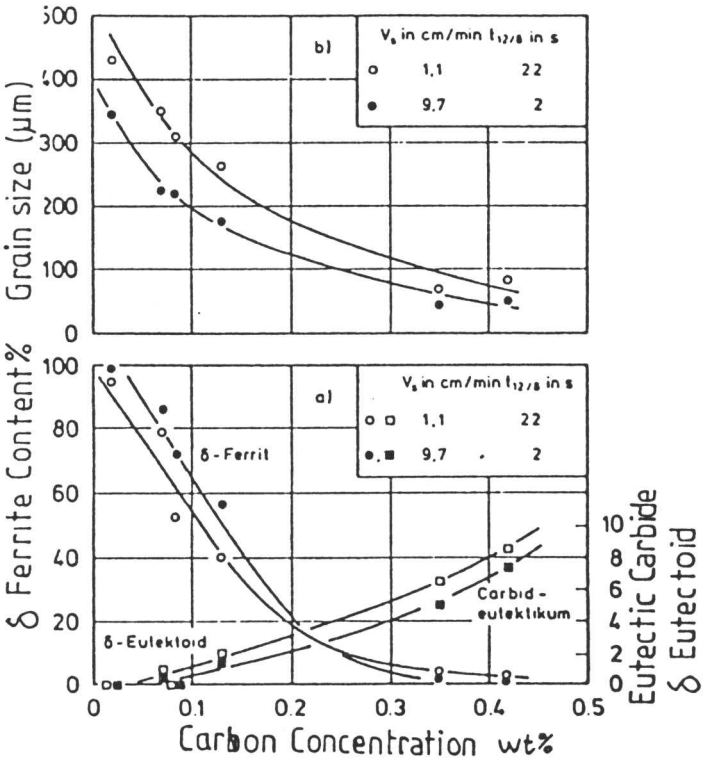

Fig. 3.10 b: Influence of carbon on δ-ferrite content and primary grain size of TIG weld metal (bases composition $\approx$ 24.4 Cr, 7 Ni wt.%), [46].

Hertzman *et al.* [47] studied the microstructure and properties of nitrogen alloyed duplex stainless steel after welding treatments; the compositions of the base metal and electrodes are shown in Table 3.3 below in wt.%.

Table 3.3: Composition of base plate and filler material in wt.%.

Element	C	Si	Mn	P	S	Cr	Ni	Mo	Cu	Al	N
Base metal	0.018	0.36	1.58	0.02	0.003	21.8	5.6	2.96	0.07	0.02	0.15
Consumable	0.018	-	1.68	0.018	0.003	27.6	8	2.99	0.06	-	0.15

They suggested that the reformation of γ during cooling is controlled by the diffusion of nitrogen in δ, the rate of transformation being conditioned by composition, temperature, time at maximum temperature and the cooling rate. They investigated nitride (Cr_2N and CrN) precipitation. EDS analysis, electron energy loss spectroscopy (EELS) and electron diffraction reveal that precipitates are CrN rather than Cr_2N, the stable nitride for the whole temperature range according to the thermodynamic calculations, Fig. 3.11. Based on the orientation relationship;

$$(001)_\delta \; //(001)_{CrN}$$
$$[100]_\delta \; //[100]_{CrN}$$

established for CrN as a plate like morphology [48], they concluded that CrN is favoured by ferrite than austenite because of its low nucleation activation energy with respect to the former. They also found that nitride precipitation is increased when γ reformation is low because of supersaturation of ferrite with nitrogen. Nitrogen is partitioned strongly between γ (high solubility) and δ (low solubility). Its partitioning increases with temperature, Fig. 3.12. The increase of nitrogen content at 1050°C was found to decrease the partitioning of Cr, Ni and Mo between δ and γ, Fig. 3.13.

Valtierra-Gallardo *et al.*, [27] investigated the effect of nitrogen additions to the shielding gas on the austenite content of tungsten inert gas autogenous weld metals of Fe-0.016C-0.4Si-22Cr-5Ni-3Mo-0.16N-0.15V-0.13Cu-0.03Nb wt.% duplex stainless steel. The γ volume fraction could be increased from 0.36 corresponding to 0.16 wt.% N (the same as the base metal) to 0.76 corresponding to 0.45 wt.% N in a weld fabricated using a pure nitrogen shielding gas, Fig. 3.14. They estimated the Ni equivalent values for a fixed Cr equivalent for different weld beads, and deduced that 1 wt.% of N is equivalent to 13.5 wt.% of Ni, Fig. 3.15.

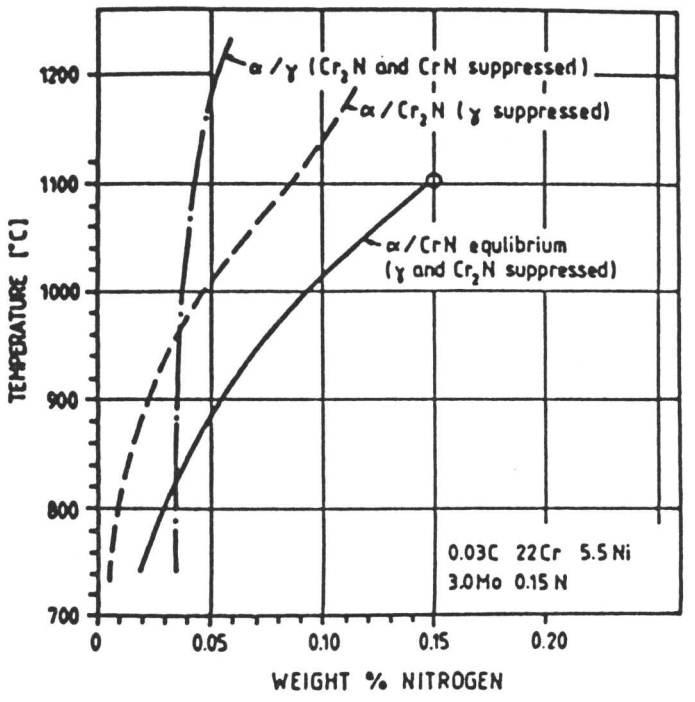

Fig. 3.11: Solubility of various phases in ferrite as function of temperature calculated for equilibrium conditions [47].

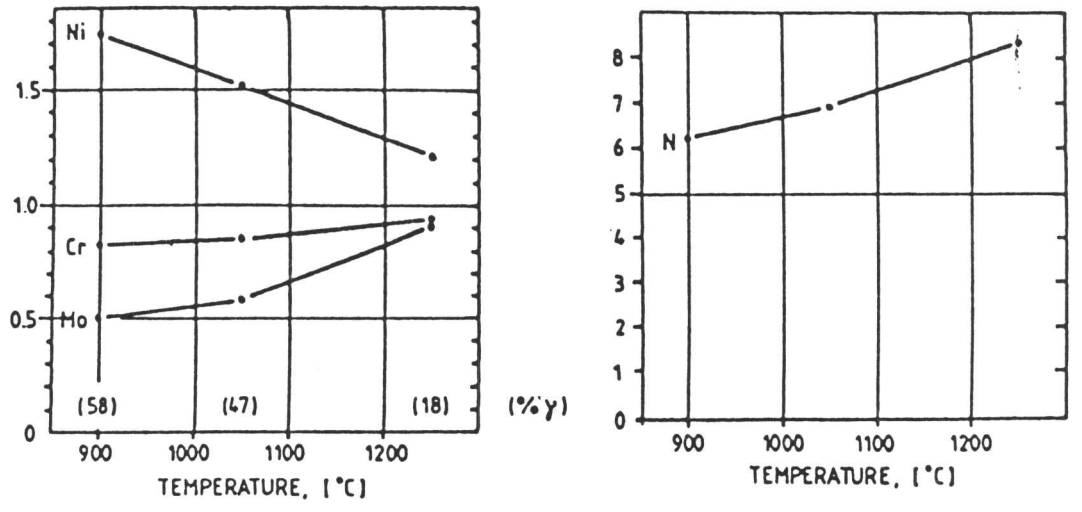

Fig. 3.12: Temperature dependence of the distribution coefficients for N, Cr, Ni and Mo in Fe-0.03C-23Cr-5.5Ni-3Mo-0.15N wt.% duplex stainless steel [47]. The vertical axis is the distribution coefficient defined as the ratio of the concentration in wt.% of the alloying element in austenite to that in δ-ferrite.

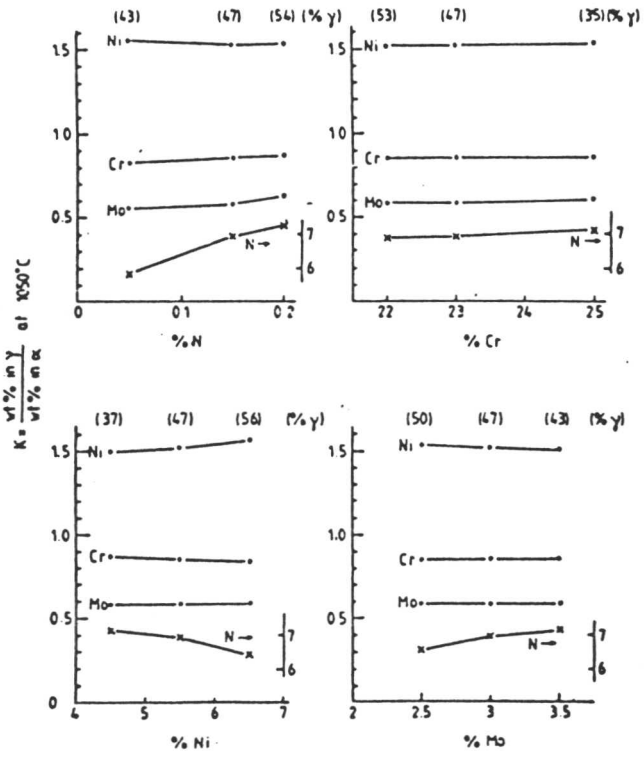

Fig. 3.13: Distribution coefficients at 1050°C as function of N, Cr, Ni, and Mo concentrations in Fe-0.03C-23Cr-5.5Ni-3Mo-0.15N wt.% duplex stainless steel [47].

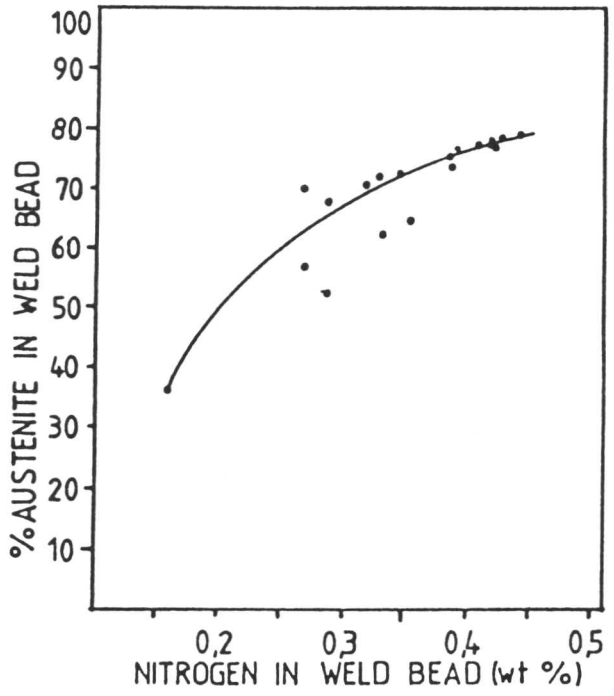

Fig. 3.14: Plot of nitrogen content of the weld bead (wt.%) versus the content of austenite in the weld bead microstructure (%), [27].

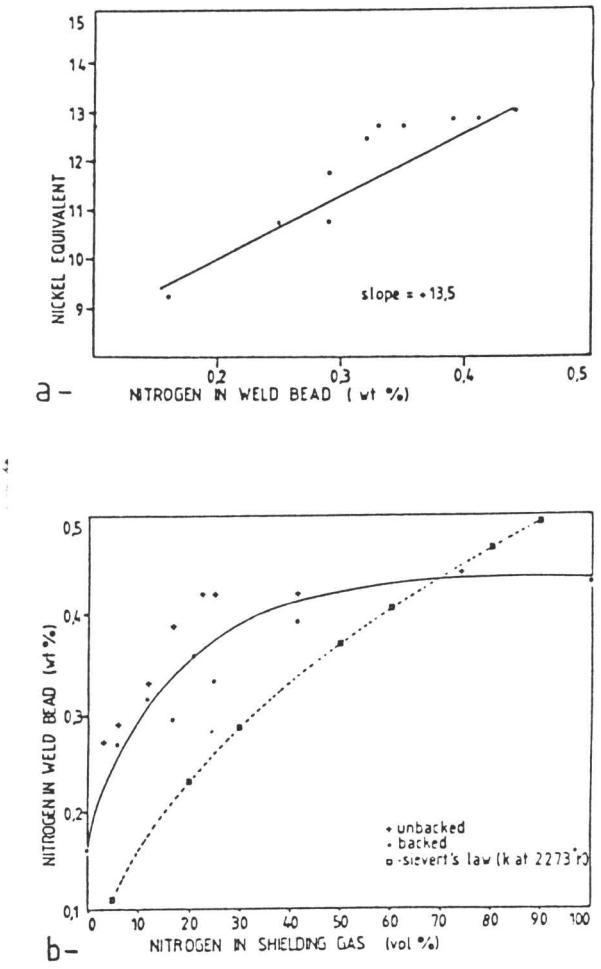

Fig. 3.15:

(a) Plot of nitrogen content (wt.%) in the weld bead versus nickel equivalents obtained from the Schaeffler diagram as modified according to Espy *et al.* [69].

(b) Plot of nitrogen (wt.%) in the weld bead, for both backed and unbacked weld runs, versus nitrogen content (vol%) of the shielding gas. The dashed curve is a Sievert's law plot, at a pressure of 1 atmosphere, for a temperature 2273 K with a value of the constant of 0.53 [27].

The effect of nitrogen on the solidification mode was also investigated [27]. For concentrations less than 0.33 wt.% N solidification commenced with the formation of δ dendrites and completed by the final solidification of liquid to γ. Between 0.33-0.36 wt.% N, a mixture of the above mentioned mode and another characterised by complete solidification to δ followed by solid state transformation to γ occurred. For the concentration range 0.36-0.45 wt.% N the latter mode dominates. This indicates, as mentioned earlier, that the solidification mode has been affected by Cr_{eq}/Ni_{eq} ratio rather than nitrogen content. Nitrogen concentrations greater than 0.45 wt.% resulted in macroporosity.

The occurrence of macroporosity can be rationalised using Sieverts law, applied at 2273 K and 1 atmosphere pressure with a gas constant value of 0.53, Fig. 3.15. At low values of N in the shielding gas, the solubility of N in the weld bead was much higher than predicted theoretically. This may well be because nitrogen is more readily ionised than argon and is therefore likely to concentrate in the centre of the arc column [49].

3.4.4 Properties of weld metal and the heat affected zone

The main reason for which duplex stainless steels have been used increasingly to replace austenitic steels is their improved resistance to stress corrosion cracking (SCC) in chloride containing environments, with the additional benefits of higher strength and adequate toughness. This combination of properties is only obtained by careful balancing of the δ to γ phase ratio. Any deviation from an optimum ratio inevitably causes detrimental effects.

The stress corrosion cracking resistance of duplex stainless steels is believed to be the result of either a "keying" mechanism by which the microstructure arrests failure mechanically [50] or an electrochemical mechanical coupling effect of the two phases present [51]. Although it is reported that welding had no significant effect on chloride induced stress corrosion cracking resistance at ambient pressure and above [52, 53], there are conflicting data. Heat affected zones with coarse grains are susceptible to SCC [54, 55]. Failure of weld metal at the fusion line by SCC when Ni-base filler material is used has been reported [56]. An adverse effect of the presence of a coarse ferritic heat affected zone on susceptibility to chloride SCC and in H_2S at 50°C has also been reported [55]. Post weld heat treatment at 950°C of a predominantly

Table 3.4: Summary of results of SCC tests on welded Fe-26Cr-6Ni-1.5Mo wt.% alloy [55].

Material thickness, (mm)	Welding process	Consumable type	Postweld heat treatment	Environment*	Samples failed**
10	MMA	Matching	None	A	1/3
				B	0/3
10	MMA	Matching	980°C/30min	A	0/3
				B	0/2
1.5	TIG	Autogenous	None	A	0/3
				B	1/2
1.5	TIG	Autogenous	980°C/30min	A	0/3
				B	0/2
10	MIG	Ni-base	none	A	-
				B	0/2
10	MIG	Ni-Base	980°C/30min	A	-
				B	0/2
1.5	MIG	Ni-base	none	A	-
				B	1/2
1.5	MIG	Ni-base	980°C/30min	A	-
				B	1/2

* A=40% $CaCl_2$ at 100°C: stressed at 70% tensile strength 440 – 470 N/mm^2

B= Vapour phase above 100 ppm NaCl solution at 225°C: stressed at 350 N/mm^2

** failed samples/tested samples: - = no tests

ferritic structure in the HAZ, was found to be beneficial in avoiding cracking, Table 3.4. [55,56,52]. The main problem is associated with the grain coarsening of δ and lack of sufficient transformation in the HAZ during cooling from high temperature. Nitrogen

reduces the interphase Cr segregation and consequently improves the corrosion resistance of γ [57]. It also enhances the formation of γ in weld metals. Weld metals of nitrogen enriched duplex stainless steels are less sensitive to stress corrosion cracking in chloride containing environments, Table 3.5.

Table 3.5: Summary of results of SCC tests in 40%$CaCl_2$ at 100°C at 90% yield stress on welded Fe-26Cr-6Ni-1.5Mo-N wt.% steels [57].

Consumable type	SamplesFailed*	Position of failure
19Cr/15Ni/3.5Mo	1/3	HAZ
18Cr/15Ni/4.5Mo/N	0/3	-
22Cr/12Ni/2.5Mo	0/3	-
20Cr/25Ni/4.5Mo/Cu	0/3	-
25Cr/22Ni/2Mo/N	0/3	-
25Cr/22Ni/2Mo	0/3	-
25Cr/5Ni/3Mo/Cu/N	2/3	HAZ (WM crack)
23Cr/9Ni/3Mo/Cu	2/3	HAZ
23Cr/9Ni/3Mo/Cu**	2/3	HAZ
23Cr/9Ni/3Mo/N	0/2	-
23Cr/6Ni/3Mo/N	0/2	-

* Samples failed/no. tested, - no failure after 2000 hrs, ** Preheated to 150°C.

The stress corrosion resistance of duplex stainless steel weld metal B, Table 3.6 with 0.03 wt.% N was found to be inferior when compared with weld metal A of higher N content but otherwise similar composition. This is because of the finer γ and Cr_2N precipitates in B. The impact toughness of weld A was found adequate for the temperature range studied, Fig. 3.16, with a ductile type fracture common except on some areas of the fracture surfaces where traces which may be associated with defects or brittle areas were observed [58].

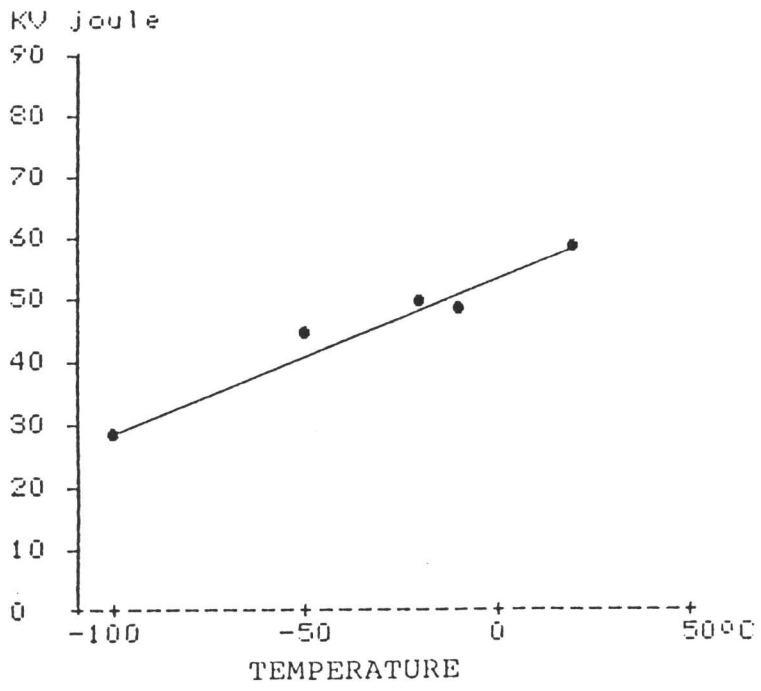

Fig. 3.16: Impact toughness as a function of temperature for weld metal "O.K 67.50" [58].

Table 3.6: Chemical composition (wt.%) and mechanical properties of the weld metals investigated in [58].

Electrode	C	Si	Mn	P	S	Cr	Ni	Mo	N	$\sigma(MPa)$	$t_{frac.}$ (hr)
A	.021	0.8	0.7	.01	.011	22.05	9.3	3.2	.097	650	67.7*
										570	**
B	.019	0.9	0.7	.025	.013	22.58	10.38	2.91	0.063	650	2.3
										570	217

* fracture occurred at the transition betweem the head and the gauge

** test interrupted without fracture after 720 hrs

Table 3.7: Concentrations in wt.% [59].

Material	C	Si	Mn	P	S	Cr	Ni	Mo	N
base metal	0.022	0.44	1.75	0.019	0.001	21.3	5.3	2.9	0.128
GTA weld	0.018	0.46	1.58	0.009	0.003	22.7	6.7	3.0	0.140
SMA weld	0.034	0.26	0.74	0.013	0.004	22.8	8.5	3.1	0.136

The pitting corrosion behaviour and low temperature toughness of nitrogen enriched duplex stainless steel weld metals (Table 3.7) has been investigated by Ogawa *et al.* [59]. Pitting occurs in the as welded structure initiating on Cr carbides within δ or on δ/γ interfaces and propagating with a preferential dissolution of δ. N improved the pitting corrosion resistance of the weld metal by retarding the carbide precipitation and improving the pitting resistance of γ, Fig. 3.17. The advancing pits were interrupted at the grain boundary in the nitrogen-enriched weld metals. They propagated preferentially in the grain boundary in the low nitrogen weld metals. The addition of Nb causes deterioration in the pitting corrosion resistance of the weld metal, due to the heavy precipitation of Nb-nitride at high temperature prior to, or during the δ to γ transformation, which reduced the beneficial effect of N on improving the corrosion resistance of γ and increasing the volume fraction of γ in the weld metal. This was also the case with titanium. Even copper, which improves the corrosion resistance in non-oxidising environments, was detrimental to chloride pitting corrosion resistance of both base and weld metals. Low temperature toughness (at $-60°C$) was largely affected by δ and its promoters chromium and molybdenum, Fig. 3.18. An increase in nickel was found to have a beneficial effect on low temperature toughness, Fig. 3.19; an increase by 3 wt.% Ni raised the toughness by 50 J at $-40°C$, lowered the ductile-brittle transition by 40°C, and changed the cleavage-like brittle fracture to a ductile one.

The effect of δ volume fraction on the impact toughness of austenitic and duplex stainless steel weld metals (Table 3.7) has also been investigated [45]. An increase in the δ content is found to decrease the toughness considerably at $-40°C$, Fig. 3.20.

3.5 Precipitates in Duplex Stainless Steel Weld Metals

Precipitation reactions have recently been reviewed in duplex stainless steels, Table 3.8 [60]. Chromium carbides ($Cr_{23}C_6$), chromium nitrides (Cr_2N, CrN), Chi phase (χ), sigma phase (σ) and other phases can be found in duplex stainless steel weld metals.

The precipitation behaviour of nitrogen alloyed Fe-Cr-Ni-Mo duplex stainless steels compared with that of a similar steel grade without nitrogen is shown in Fig. 3.21 [63]. After a solution annealing treatment for 30 minutes at 1050°C followed by quenching in water, the nitrogen alloyed steel 1 shows a precipitation free structure with about 0.6 volume fraction δ and 0.4 γ. At 800°C ageing temperature, precipitation

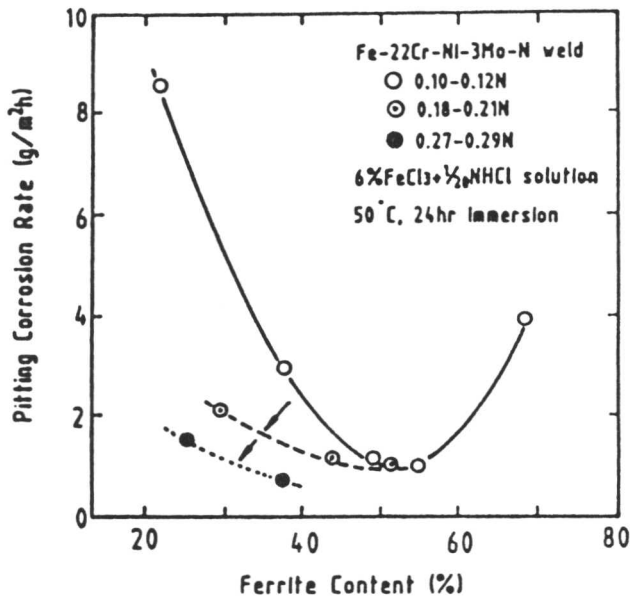

Fig. 3.17: The effect of ferrite content and nitrogen on pitting corrosion resistance of Fe-22Cr-Ni-3Mo-N wt.% duplex stainless steel weld metal [59].

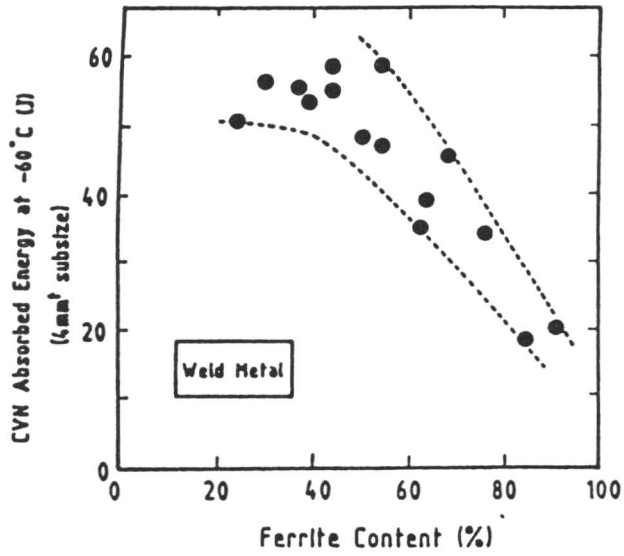

Fig. 3.18: The effect of ferrite content on low-temperature toughness of duplex stainless steel weld metals, composition range Fe, 22-28Cr, 5-10Ni, 1-7Mo, 0.1-0.27N wt.%) [59].

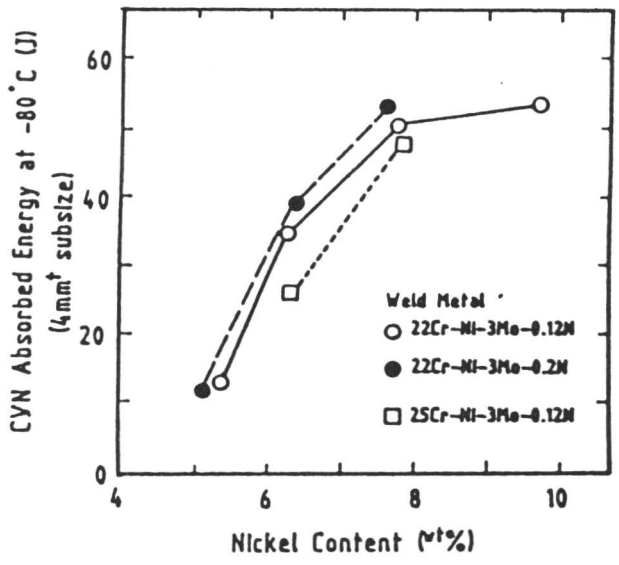

Fig. 3.19: The effect of nickel, chromium and nitrogen on the low-temperature toughness of duplex stainless steel weld metals [59].

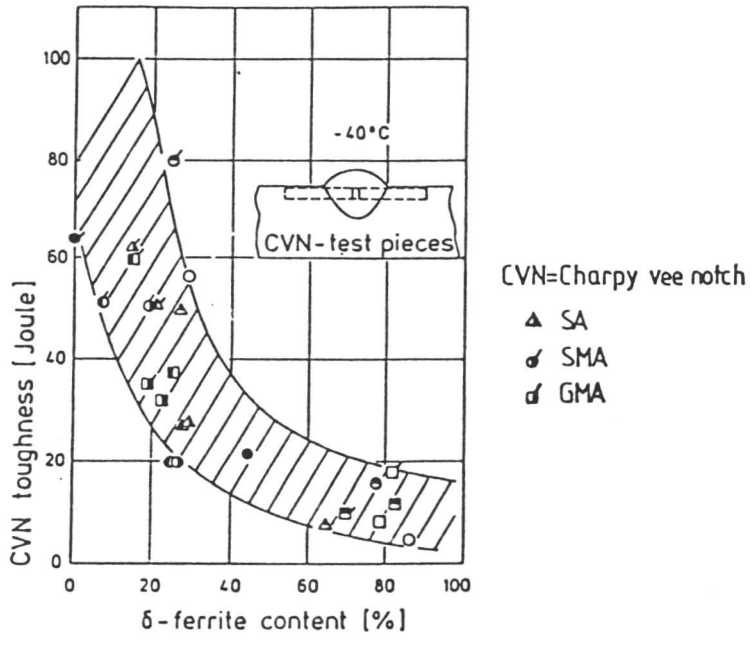

Fig. 3.20: The effect of δ-ferrite on weld metal toughness. Weld metal compositions and welding parameters in Table 3.2 [45].

Table 3.8: Precipitates in duplex stainless steel [60]

Phase	Crystal Structure	Lattice Parameters Å	Composition
$Cr_{23}C_6$	f.c.c.	a = 10.569	(63 5 18 14)†
		a = 10.680	$(Cr_{16}Fe_5Mo_2)\ C_6$
		a = 10.638	$(Cr_{17}Fe_{4.5}Mo_{1.5})\ C_6$
			$(FeCr)_{23}\ C_6$
M_7C_3	Pseudo-hexagonal	a = 13.9820 c = 4.5065	$(CrFe)_7\ C_3$
Sigma (σ)	Tetragonal	a = 8.828 c = 4.597	(29 5 55 11)†
		a = 8.799 c = 4.544	(8.35 30.84 – 8.35)†
		a = 9.188 c = 4.812	(FeCr) (FeMo)
			Fe(CrMo)
Chi (χ)	b.c.c.	a = 8.878	(21 5 52 22)†
	$\alpha - Mn$ structure	a = 8.92	$(Fe_{36}Cr_{12}Mo_{10})$
		a = 8.862	$((FeNi)_{36}Cr_{18}Mo_4)$
R Phase	Hexagonal	a = 10.937 c = 19.346	(25.6 – 44.8 27.8)†♠
Laves η	Hexagonal	a = 4.73 c = 7.72	(11 6 38 45)†
		a = 4.744 c = 7.725	(Fe_2Mo)

† Concentrations of Cr, Ni, Fe and Mo in wt.% respectively.

♠ Cobalt concentration 1.8 wt%.

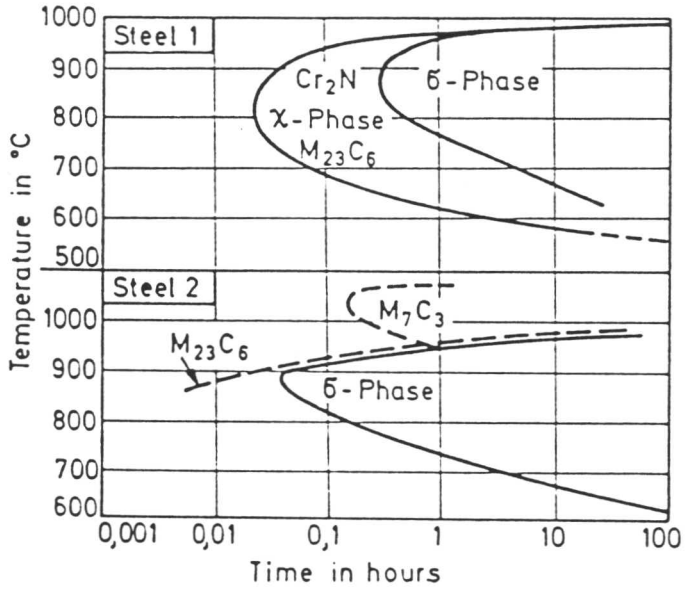

Fig 3.21: Time-temperature precipitation (TTP) diagrams of two austenitic-ferritic duplex stainless steels. Steel 1 according to Herbsleb and Schwaab [61], steel 2 to Jolly and Hochmann [62]. Solution annealing: steel 1 –1050°C/30 min., steel 2 –1150°C/60 min. Chemical composition in wt.%: 1 – Fe-0.028C-0.45Si-1.63Mn-21.8Cr-5.0Ni- 3.12Mo-0.113N and 2– Fe-0.028C-0.5Si-0.7Mn-20.9Cr-7.4Ni-2.3Mo-0.073N-1.4Cu.

started after only 2 minutes with the formation of Cr_2N at the ferrite grain boundaries together with the relatively coarser globular particles of χ phase. In addition, very small amounts of $M_{23}C_6$ carbides were observed. After about 20 minutes, sigma phase appears for the first time in the temperature range 800-900°C. The kinetics of precipitation in steel 2 were faster for sigma and more intense for carbides with the appearance of M_7C_3 carbides. The effect of precipitation on the corrosion resistance as evaluated by the Straus test suggests an improved resistance in the nitrogen alloyed steels since their limited amount of carbides and nitrides is not enough to cause sensitisation by Cr depletion. In the Huey corrosion test carried out in a strong solution of boiling nitric acid, strong corrosive attacks were observed associated with the precipitation of χ phase.

Ogawa and Koseki [59] investigated the microstructure of nitrogen-enriched duplex stainless steel weld metals (Table 3.7). In the δ phase of the as-welded structure, carbides, nitrides and carbonitrides were identified. For low nitrogen and high carbon weld metals strong X-ray peaks for $Cr_{23}C_6$ were obtained, while in low carbon and high nitrogen weld metals M_2N type nitrides and carbonitrides were identified. δ areas adjacent to γ were free of precipitates indicating a depleted region of carbon and nitrogen.

Precipitation reactions in melt runs made using the tungsten inert gas welding process, on an Fe-18Cr-12Ni-2.5Mo-0.06C wt.% alloy have been studied by Ritter *et al* [64]. This alloy, which normally solidifies by way of primary δ, was made to solidify by way of primary γ by adding nitrogen to the argon gas shield. Three different composition welds were produced by adding respectively 1, 3 and 6 vol.% nitrogen to the shielding gas. In all three welds intragranular phases were found distributed throughout the austenite and occasionlly at the δ/δ interfaces. These phases were complex and of two types. One type was a mixture of a phase rich in Mn, Si and Al and a phase high in Si. The other type also contained a phase high in Si, but with a Mn rich sulphide phase as the second component. In the welds made using the 3 vol. % nitrogen addition a third type of intragranular phase, identified by diffraction as $(Cr, Fe)_3P$ was observed.

Interfaces between eutectic ferrite and austenite in the welds were observed to be densely covered with small precipitates of χ-phase. These were thought to precipitate as a result from the supersaturation of Mo in the ferrite.

3.6 Empirical Estimation of the Microstructure of Duplex Welds

All approaches towards weld metal microstructure prediction are so far empirical estimations based on representing the influence of chemical composition of stainless steels, in the form of Cr equivalent, if they are ferrite stabilisers and Ni equivalent if they are austenite stabilisers.

The Schaeffler [65] diagram, Fig. 3.22, has been long used to estimate the volume fractions of the constituent phases of stainless steel weld metals as a function of the Cr and Ni equivalents. It was developed originally for the joining of dissimilar steel grades using stainless steel electrodes, in order to predict as to which alloying group the original austenitic weld metal *i.e.* the electrode material, would be transformed as a result of dilution with the differently alloyed base materials, and to estimate the residual ferrite in austenitic weld metals. The importance of estimating the residual ferrite content is driven from its effect on reducing the hot cracking susceptibility of austenitic weld metals. Due to constitutional reasons discussed earlier (see section 3.2.6), the austenite has a stronger tendency to form low melting phases and consequently, a higher tendency towards hot cracking.

The Schaeffler diagram was constructed on the basis of experimental tests, carried out on single pass non-weave bead weld deposit produced using 4.76 mm diameter uniform core austenitic stainless steel electrodes, on various base plate materials. Thus the original experiments did not consider different cooling rates and did not account for reheating which is important in multirun weld metals [66].

According to Schaeffler the scatter in the ferrite estimation is about 4%. This is believed to apply for ferrite contents up to 15% only. According to Mundt *et al.* [67], with higher ferrite contents, there is an increasing effect of the cooling rate on the δ to γ transformation with the possible deviation becoming larger and larger. Even with very low ferrite contents 1-5 % Suuatala *et al.* [68] found that the ferrite content is influenced by the welding speed.

Since constructed the Schaeffler diagram has undergone a series of modifications . It was first modified by Espy *et al.* [69] to account for the effect of Cu, N, V, and Al. An empirical formula for the calculation of the volume fraction of δ in a duplex-weld structure was derived from the Schaeffler diagram by Safarian [70].

$$V_\delta = 3[Cr_{eq}\ \text{wt.\%} - 0.93\ Ni_{eq}\ \text{wt.\%} - 6.7]$$

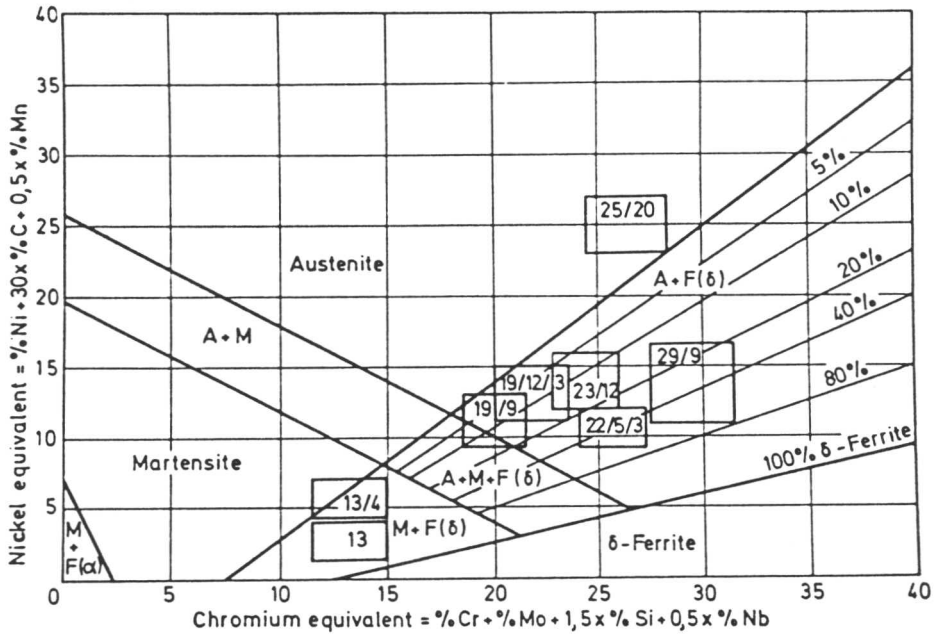

Fig. 3.22: Schaeffler diagram for stainless steel weld metal according to the AWS Welding Handbook [72]. The diagram shows the zones of various weld metals as deposited by coated electrode types. The alloy contents are stated in the order Cr, Ni and Mo in wt.%.

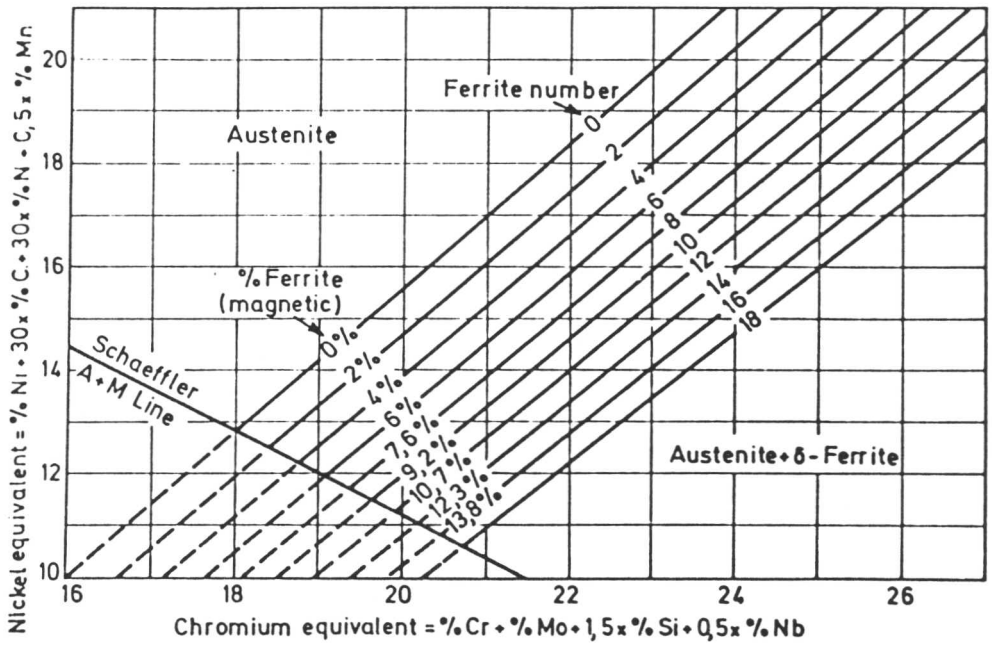

Fig. 3.23: Delong diagram revised in January 1973 for the determination of ferrite numbers in austenitic stainless steel weld metals [71].

Taking the effect of nitrogen on the volume fraction of δ in stainless steel weld metals into account, Delong [70] proposed a modified Schaeffler diagram, Fig. 3.23 attributing a factor of 30 for nitrogen (wt.%). The Delong diagram refers to a ferrite number (FN), which is a standardised method of evaluating the ferrite content developed by The Welding Institute using a magnetic measuring device.

Another approach for predicting the δ/γ balance in duplex stainless steel weld metal was proposed by Skuin and Kreyssing [29]. The ratio of Cr_{eq} to Ni_{eq} "P" was used to estimate the volume fraction of γ at room temperature.

$$P = \frac{Cr + 3Si + 7Ti + 12Al\,wt.\%}{Ni + 30C + 26N + 0.7Mn\,wt.\%}$$

A modification of the"P" ratio was proposed by Gooch and Honeycombe [28] including the effect of the Mo, and differently evaluating the influence of N and C on the estimated volume fraction of austenite.

$$P_{mod.} = \frac{Cr + Mo + 3Si\ (wt.\%)}{Ni + 15C + 10N + 0.7Mn\ (wt.\%)}$$

In their study to evaluate the effect of Mn and Ni on the type of solidification in stainless steel weld metals, Suutala *et al.* [73] correlated to a number of different formulae for the calculation of Cr and Ni equivalents. For the determination of the ferrite number FN they found the Schaeffler and Delong formulae quite suitable. To determine the boundary between the primary ferrite and primary austenite solidification, they recommended the formulae developed by Hammar and Svensson [74].

$$Cr_{eq} = Cr + 1.37Mo + 1.5Si + 2Nb + 3Ti\ wt.\%$$
$$Ni_{eq} = Ni + 0.31Mn + 22C + 14.2N + Cu\ wt.\%$$

In order to establish the effect of thirteen different alloying elements in terms of Ni and Cr equivalents in determining the δ content, Hall *et al.* [75] arrived at a different result, probably because of the overlapping effect of alloying elements caused by their interaction which may vary with their increased content.

Noble and Gooch [76] recently presented a new compositional factor (P*) for estimating weld metal austenite content within about 12% variation at 0.5 volume fraction austenite level over an arc energy range 0.3 to 4.2 kJ mm^{-1}, Fig. 3.24.

$$P^* = \frac{Cr + 1.5Mo + 2Mn + 0.25Si(wt.\%)}{2Ni + 12C + 12N(wt.\%)}$$

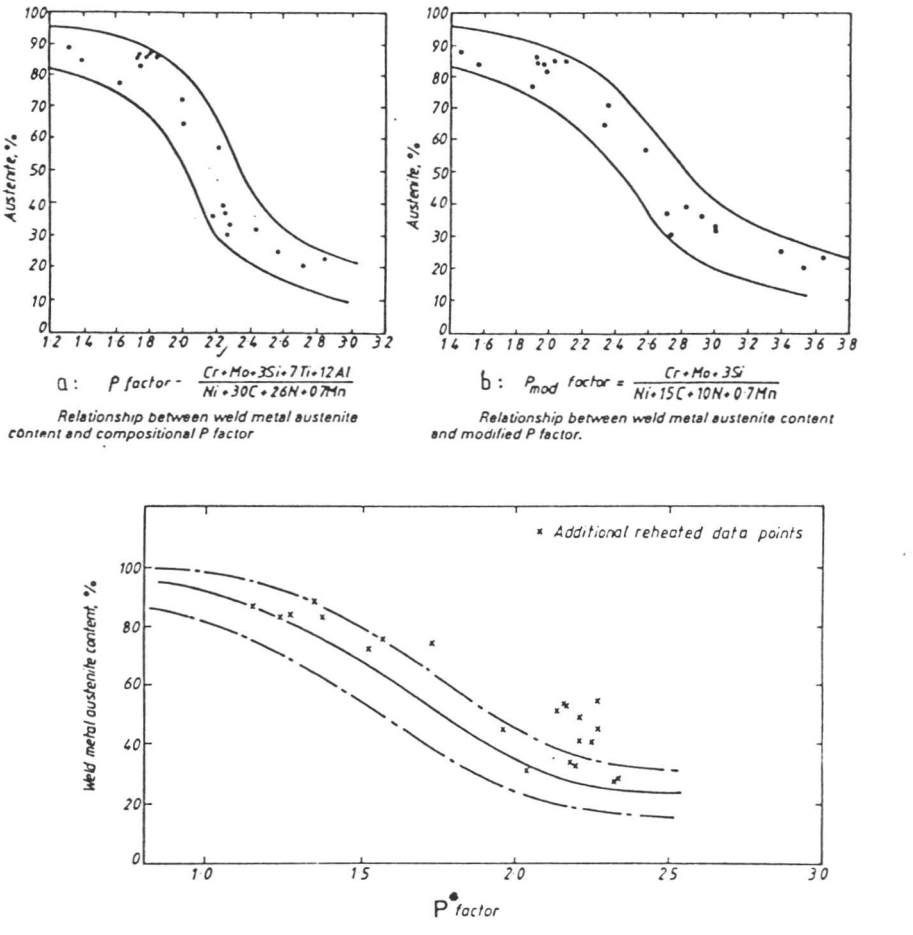

Fig. 3.24: The relationships between the compositional factors P, $P_{mod.}$ and P^* and the measured austenite content of the weld metal [76].

References

1. Wittke, K. (1968) Schwiessen-technik (Berlin), **18**, p. 295.
2. Savage, W. F., Lundin, C. D. and Aranson, A. H. (1965) Weld. J., **44**, Res. Suppl., p. 175s.
3. Folkhard, E. 'Welding Metallurgy of Stainless Steels' (1988) Wien-New York, Springer-Verlag publishers, p. 54.
4. Plockinger, E. and Straube, H. 'Die Edelstahlerzeugung (1965) Wien-New York, Springer, p. 728.
5. Folkhard, E. 'Welding Metallurgy of Stainless Steels' (1988) Wien-New York, Springer-Verlag publishers, p. 58.
6. Mitsche, R. and Niessner, M. 'Angewandte Metallographie' (1939) Leipzig, Johann Ambrosius Barth.
7. Baumel, A. (1976) Werkst. u. Korrosion, **27**, p. 687.
8. Weingerl, H. and Straube, H. (1976) Werkst. u. Korrosion, **27**, p. 69.
9. Folkhard, E. 'Welding Metallurgy of Stainless Steels' (1988) Wien-New York, Springer-Verlag publishers, p. 75.
10. Cieslak., M. J., Ritter. A. M. and Savage, W.F. (1982) Weld. J., **61**, Res. Suppl., p. 1s.
11. Blanc, G. and Tricot, R. (1971) Mem. Sci. Rev. Metallurg., **68**, p. 735.
12. Hoffmeister, H. (1973) Schweissen u. Schneiden, **25**, p. 164.
13. Heritier, J. and Levy, J. (1976) Mem. Sci. Rev. Metallurg., **73**, p. 523.
14. Takalo, T., Suutala, N. and Moisio, T. (1979) Met. Trans., **10A**, p. 1173.
15. Schurmann, E. and Voss, H.J. (1977) Arch. Eisenhuttenwes, **48**, p. 129.
16. Kulmburg, A., Bloch, R. and Swoboda, K (1966) Berg- u. huttenum. Mh., **111**, p. 420.
17. Eckstein, H. J. 'Warmebehandlung von Stahl. Metallkundliche Grundlagen (1969) Leipzig, VEB, p. 92, 130.
18. Fridberg, J., Torndahl, L.E. and Hillert, M. (1969) Jernkontor. Ann., **153**, p. 263.
19. Folkhard, E. 'Welding Metallurgy of Stainless Steels' (1988) Wien-New York, Springer-Verlag publishers, p. 50.
20. Tiller, W.A. (1959) J. Iron Steel Inst., **192**, p. 338.

21. Savage, W. F. (1980) Weld. World, **18**, p. 89.

22. Flemings, M. C. 'Solidification and Casting of Metals (1977) London, Metal Soc.

23. Wittke, K. (1966) Schweissentechnik (Berlin), **16**, p. 158.

24. Suutala, N., Takalo, T. and Mosio, T. (1979) Met. Trans., **10A**, p. 513.

25. Suutala, N., Takalo, T. and Mosio, T. (1979) Met. Trans., **10A**, p. 1183.

26. Suutala, N., Takalo, T. and Mosio, T. (1980) Met. Trans., **11A**, p. 717.

27. Valtierra-Gallardo, S., Hawkins, D. N. and Beech, J. (1986) Conf. Proc. 'Duplex Stainless Steel', The Hague, late paper.

28. Honeycombe, J. and Gooch, T. G. (1985) The Weld. Inst. Report 286/ 1985.

29. Skuin, K. and Kreyssing, T. (1978) Neue Hutte, **23** (1), p. 22.

30. Zitter, H. (1957) Arch. Eisenhuttenwes, **28**, p. 401.

31. Nippes, E. F. (1959) Weld. J., **38**, Res. Suppl., p. 1s.

32. Klug, P. (1980) Dr.-Techn.-Dissertation, Techn. Universitat Graz.

33. Espy, R. H. (1982) Weld. J., **61**, Res. Suppl., p. 149s.

34. Lippold, J. C. and Savage, W. F. (1979) Weld. J., **58**, Res. Suppl., p. 362s.

35. Velkov, K. and Schelew, A. (1982) Schweissentechn., (Berlin), **32**, p. 542.

36. Folkhard, E. 'Welding Metallurgy of Stainless Steels' (1988) Wien-New York, Springer-Verlag publishers, p. 71.

37. Folkhard, E. 'Welding Metallurgy of Stainless Steels' (1988) Wien-New York, Springer-Verlag publishers, p. 81.

38. Perteneder, E., Bloch, R. and Wedl, F. (1983) Metallographie, p. 345.

39. Folkhard, E. 'Welding Metallurgy of Stainless Steels' (1988) Wien-New York, Springer-Verlag publishers, p. 83.

40. Gooch, T. G., Conf. Proc. 'Duplex Stainless Steels', St. Louis, USA (1982) ed. R.A. Lula, Publ. by ASM, p. 573.

41. Flasche, L. H., Conf. Proc. 'Duplex Stainless Steels', St. Louis, USA, (1982) ed. R.A. Lula, Publ. by ASM, p. 553.

42. Svensson, L. E. and Gretoft, B., ESAB AB of Sweden, Internal report (1985).

43. Van-Nassua, L. (1982) Welding in the world, **20**, 1/2, p. 22.

44. Hoffmeister, H. and Mundt, R. (1981) Arch. Eisenhuttenwes., **52** (4), p. 159.

45. Hoffmeister, H., Mundt, R. and Berner, K.D. (1985) Mat. Tech., **56**, 3, p. 163.

46. Mundt R. and Hoffmeister, H., Conf. Proc. Stainless Steels '84, Göteborg, Sept. 1984, The Inst. of Metals, London (1985), p. 315.

47. Hertzman, S. et al. 'Duplex Stainless Steel', Conf. Proc., Oct. 1986, The Hague, Publ. by Nederlands Instituut Voor Lastechniek, p. 257.

48. Abron, R. H. and Bain, E. C. (1930) Trans. Amer. Soc. Steel Treating **8**, p. 837.

49. Eagar, T. W., Proc. Conf. 'Physical Metallurgy of Weldments', G.E.C., USA (1978) p. 31.

50. Shimodaira, S., Takano, M., Takizawa, Y and Kamide, H., 'Stress Corrosion Cracking and Hydrogen Embrittlement of Iron Base Alloys, Confs. Unieux Firminy, France, June 12-16, 1973, NACE (1977). Staehle, R.W., Hochmann, J., McCright, R.D. and Slater, J.E., p. 1003.

51. Flowers, J. W., Beck, F. H. and Fontana, M. G. (1963) Corrosion, **19**, p. 186t.

52. Nordin, S., Achema-Congress Frankfurt-am-Main, 1973.

53. Pleva, J. and Nordin, S., Conf. Proc. 'Duplex Stainless Stels', St. Louis, USA (1982), ed. R.A. Lula, Publ. by ASM (1983), p. 603.

54. Magnin, T. et al. 'Conf. Proc. Duplex Stainless Steel', St. Louis, USA (1982), Publ. by ASM (1983), p. 535.

55. Maruo, T. et al. 'Conf. Proc. Duplex Stainless Steel, St. Louis, USA (1982), Publ. by ASM (1983), p. 465.

56. Honeycombe, J. and Gooch, T.G., Welding Inst. Rep. 64/1978/M.

57. Dundas, H. J., Bond, A. P., Paper 206 NACE Corrosion '85, Boston March (1985).

58. Svensson, L. E. and Gretoft, B., Conf. Proc. 'Duplex Stainless Steel', Oct. 1986, The Hague, Publ. by Nederland Instituut voor Lastechniek, p. 288.

59. Ogawa, T. and Koseki, T., Conf. Proc. 'Duplex Stainless Steels', Oct. 1986, The Hague, Publ. by Nederland Instituut voor Lastechniek, p. 77.

60. Soylu, B. (1988) Ph.D. Thesis, University of Cambridge, Dept. of Mat. Sci. and Metallurgy.

61. Hershleb, G. and Schwaab, P. Conf. Proc. 'Duplex Stainless Steels', St. Louis, USA (1982), ed. R.A. Lula, Publ. by ASM (1983), p

62. Jolly, P. and Hochmann, J. (1973) Mem. Sci. Rev. Metallurg., **70**, p. 117.

63. Folkhard, E. 'Welding Metallurgy of Stainless Steels' (1988) Wien-New York, Springer-Verlag publishers, p. 119.

64. Ritter, A. M. et al. (1983) Met. Trans., **14A**, p. 37.

65. Schaeffler, L. A. (1949) Metal Progress, **56**, p. 680.

66. Folkhard, E. 'Welding Metallurgy of Stainless Steels' (1988) Wien-New York, Springer-Verlag publishers, p. 89.

67. Mundt, R. and Hoffmeister, H. (1983) Stahl u. Eisen, δ 103, p. 611.

68. Suutala, N. (1983) Met. Trans. A, **14A**, p. 191.

69. Espy, R. H., (1982) Wel. Jnl. Res. Suppl., **61** (5), p. 149s.

70. Safarian, D. (1959) Metallurgie de la Soudure, Dunod, Paris.

71. Delong, W. T. (1960) Metal Progress, **77**, p. 98.

72. Welding Handbook, Vol. 4 'Metals and Their Weldability (1972) Miami, Florida, American Welding Society.

73. Suutala, N. (1982) Met. Trans., **13A**, p. 2121.

74. Hammar, O. and Svensson, U. 'Solidification and Casting of Metals London, The Metals Society, p. 401.

75. Hull, F. C. (1973) Weld. J., **52**, Res. Suppl., p. 193s.

76. Noble, D.N. and Gooch, T.G. (1986) The Weld. Inst. Report 321/1986.

Chapter 4

EXPERIMENTAL TECHNIQUES

4.1 Introduction

In this chapter the materials, heat treatment and the experimental procedures will be described. Since the ultimate aim of this investigation is to lay the foundations for a model for the prediction of microstructure of duplex stainless steel weld metals, based on more rigorous phase transformation theory, the microstructure as well as the behaviour under isothermal heating and continuous cooling of both duplex stainless steel base metals and weld metal have to be considered in order to establish the effects of parameters such as, alloy chemistry, cooling rate, *..etc.*

4.2 Materials

The materials investigated are summarised in Table 4.1. Due to availability, the work started on a commercial duplex stainless steel base metal Fe-25Cr-5Ni-1.5Mo-0.03C wt% (SH). As time progressed, two weld pads WR2 and WR4 were received on which optical microstructure investigation was carried out. Two pure melts R2P and R4P of similar composition to WR2 and WR4 except for nitrogen and oxygen contents, were prepared in an induction furnace under vacuum, for comparative studies. A "buttered" duplex stainless steel weld (BW) was investigated under isothermal heating conditions, continuous cooling and ageing using optical and electron microscopy. An electron beam duplex stainless steel weld microstructure was also tested to explore the effect of very fast cooling rates. A weld fabricated throughout with duplex stainless steel (SP1) was also examined using optical microscopy to investigate the complete joint, *i.e.* weld metal, heat affected zone and parent metal. Weld metal W111 was investigated together with wrought alloy SH using dilatometry to enable the effect of δ-ferrite grain size and inclusions on the transformation behaviour to be investigated.

4.3 Welding

The weld pads WR2, WR4 and W111 were provided by ESAB of Sweden. WR2 was deposited on mild steel plate using the metal inert gas welding technique. WR4 was deposited on austenitic stainless steel plate using a submerged arc welding technique. BW is a buttered duplex stainless weld deposited using manual metal arc technique,

Table 4.1: Chemical composition (wt. %) of the wrought and welded duplex stainless steel alloys investigated. The nitrogen and oxygen concentrations are stated in parts per million by weight.

Material	C	Si	Mn	P	S	Cr	Ni	Mo	V	Nb	Ti	Al	Cu	N	O
SH	0.03	0.46	0.83	0.02	0.01	25.5	4.80	1.40	0.001	-	0.001	0.027	0.09	630	-
SHP	0.01	<0.01	<0.01	0.002	0.006	25.63	4.64	2.31	-	-	-	-	-	160	1700
W111	0.074	1.63	0.92	0.014	0.007	26.0	5.26	1.62	0.085	0.034	0.012	0.016	0.06	890	1120
WR2	0.02	0.43	1.52	0.013	0.003	22.76	7.8	2.87	0.03	0.003	0.003	0.023	0.06	1480	483
R2P	<0.02	0.35	1.32	-	-	23.4	7.5	3.5	-	-	-	-	-	-	-
R2PP	0.006	< 0.01	< 0.01	0.002	0.006	23.65	9.11	2.83	-	-	-	-	-	145	1600
WR4	0.02	0.48	1.11	0.024	0.014	23.10	8.79	2.98	0.09	0.008	0.003	0.027	0.01	786	1160
R4P	<0.02	0.47	1.03	-	-	22.8	7.1	3.0	-	-	-	-	-	-	-
*SP1**	0.023	0.44	1.31	0.029	0.009	22.2	5.4	2.69	0.04	<0.01	<.01	-	0.24	1020	140
*SP2**	0.021	0.43	1.30	0.029	0.009	22.0	5.4	2.69	0.04	<0.01	<.01	-	0.24	1040	140
BW	0.026	1.01	0.82	0.018	0.018	22.69	8.75	3.14	0.075	0.02	0.01	0.01	0.07	876	881
*M22***	0.021	0.49	1.64	0.019	-	22.50	7.9	2.92	0.05	<0.01	<0.01	-	0.06	1480	100
IC373	0.015	0.50	0.67	0.022	0.008	25.9	5.1	3.68	0.05	0.03	<0.01	-	1.83	1420	30
IC378	0.026	0.39	1.38	0.026	0.005	21.8	5.5	3.03	0.07	<0.01	<0.01	-	0.18	1400	60
IC381	0.025	0.48	1.92	0.026	0.006	22.1	5.8	3.17	0.13	<0.01	<0.01	-	0.07	1420	70
MELT 3	0.005	<0.01	<0.01	0.002	0.006	23.15	4.08	1.16	-	-	-	-	-	40	1800
MELT 4	0.006	<0.01	<0.01	0.002	0.006	18.34	7.7	0.01	-	-	-	-	-	52	618
MELT 5	0.01	<0.01	<0.01	0.002	0.006	18.32	4.6	2.38	-	-	-	-	-	70	953

* = Chemical composition stated is that of the pipe material and not the welds.

** = Filler metal used to deposit SP2

the parent plates, being of carbon steel and with wafers of duplex stainless steel placed on their surfaces prior to the weld deposition. Available relevant details for the above mentioned welds are shown in Table 4.2.

SP1 is a longitudinal seam weld in duplex stainless steel pipe material, the welding procedure being shown in Table 4.3. SP2 is a pipe weld deposited by a girth welding procedure, the procedure and other parameters being shown in Table 4.4. Both welds SP1 and SP2 were provided by the Welding Institute.

Table 4.2: Welding data for the investigated weld alloys.

Material	Voltage	Current	Speed	Joint	Welding Process	Shield Gas	Filler Material	Remarks
WR2	DC+ 27V	240A	-	Pad	MIG	16.86/ Ar/CO_2	ϕ 1.2 (mm)	15 layers on mild steel/ weaving tec-nichque
WR4	DC+ 27V	420A	-	Pad	SA	16.86/ 10.92	ϕ 3.0 (mm)	6 layers on SS233S
BW	28V	140A	4mm/sec	Butt-ISO	-		OK67.50 ϕ 4mm	1G-150°C interpass temperature
SP1				Square Butt	Automatic plasma for root and TIG		Sandvik 22-6-3	Root pass without fill-er - 2 passes No post-weld H. Treatment (seam welding)
SP2	DC- 9V for all passes	80A 80A 80A	50 40 40	Girth weld procedure	Manual TIG	Ar 8L/min	Metrode 22-8-3-L	Arc energy 0.86, 1.1, 1.1 for passes, vertical up, backing gas Ar-22l/min interpass temp. 150°C max.

4.4 Heat Treatment

To study whether the homogenised and deformed duplex stainless steel base metals had different transformation kinetics, some of the swaged (deformed) rods were held at 1250°C for three days. Prior to homogenisation each specimen was sealed in a silica tube under a partial pressure of argon (about 100 mm Hg) to prevent oxidation and decarburisation. The solution treatment was carried out in a resistance heated tube furnace. The temperature was monitored to within ±5°C using a Pt-Pt/13Rh wt.% thermocouple. The resulting δ-ferrite grain size was found to be coarse. Some of the solution treated specimens were reswaged and retreated again at 1150°C for 62 hrs following the same procedure mentioned earlier in order to obtain a finer δ grain size.

Table 4.3: Longitudinal seam welding procedure

Nominal pipe outside diameter	273 mm
Nominal wall thickness	5.0 mm
Joint preparation	Square butt
Number of passes	2
First pass	Automatic plasma arc weld with no filler metal
Second pass	Automatic TIG weld with SANDVIK
	(Fe-22Cr-6Ni-3Mo wt%) filler
No post weld heat treatment	

Table 4.4.a: Girth welding procedure

Welding process	Manual TIG
Filler rod type	Metrode 22.8.3.L
Filler diameter	2.4 mm
Shielding gas	Argon at 8 l/min
Backing gas	Argon at 22 l/min
Electrode	2.4mm diameter,
	$W - 2\%Th, 60^{\circ} vertex$
Pipe position	AWS 5 G (*i.e.* fixed horizontal)
Welding direction	Vertical up
Power source	d.c. electrode negative
Interpass temperature	150°C maximum

Table 4.4.b: Welding parameters

Run Number	1(root)	2	3	accuracy
Welding current, A	80	80	80	±10%
Arc voltage, V	9	9	9	-
Travel speed, (mm/min)	50	40	40	approximate
Arc energy, kJ/mm	0.86	1.1	1.1	-

Note: backpurge inserts set 50mm from joint line. 5min purging before welding. 100mm of weld area left open with remainder of joint sealed with tape. Backing maintained for all runs.

To determine the ferritisation temperature (T_δ) of duplex stainless steel base metals SH, R2P and R4P, four homogenised specimens of each alloy were sealed in quartz tubes as discussed earlier. Specimens were heated at 1200, 1250, 1300, 1350°C for 5 and 15 minutes intervals after which silica tubes were quickly broken and the specimens were plunged into iced-brine. The same heat treatment was repeated for swaged specimens.

Ageing heat treatments were performed on welded BW specimens for a variety of time intervals to simulate post weld heat treatment and to investigate the δ-ferrite to austenite transformation starting from a mixture of $\delta + \gamma$, and to study other precipitation reactions.

Long term ageing treatments were performed on specimens of alloys SH, SHP, WR4 IC373, IC373 and IC381 (chapter 7) in order to establish equilibrium phase fractions.

4.5 Optical Microscopy

For metallography, the specimens were hot mounted in acrylic, thin large sections of weld metals were cold mounted, and even larger specimens were prepared without mounting. All specimens were ground on silicon carbide paper to a depth sufficient to remove any unrepresentative surface. They were then mechanically ground down to 1200 grit emery paper, and finally polished with 6, 1 and $\frac{1}{4}$ micron diamond pastes. The specimens were then thoroughly cleaned with running cold water and washed with alcohol before drying.

Two etchants were used to reveal the microstructure, 25 wt% NaOH in aqueous solution for electroetching for 10 seconds at 4 volts, and Beraha's colour etchant 10ml HCl, 100ml H_2O and 0.5 to 1 gram $K_2S_2O_5$. The latter was always used in a freshly prepared condition and was discarded immediately after use.

4.6 Dilatometry

All dilatometry was performed on a Theta industries high speed dilatometer (Fig. 4.1). Specimen sizes were chosen to satisfy the cooling rates required and to avoid exceeding the transducer (length measuring device) limits. Because of the high

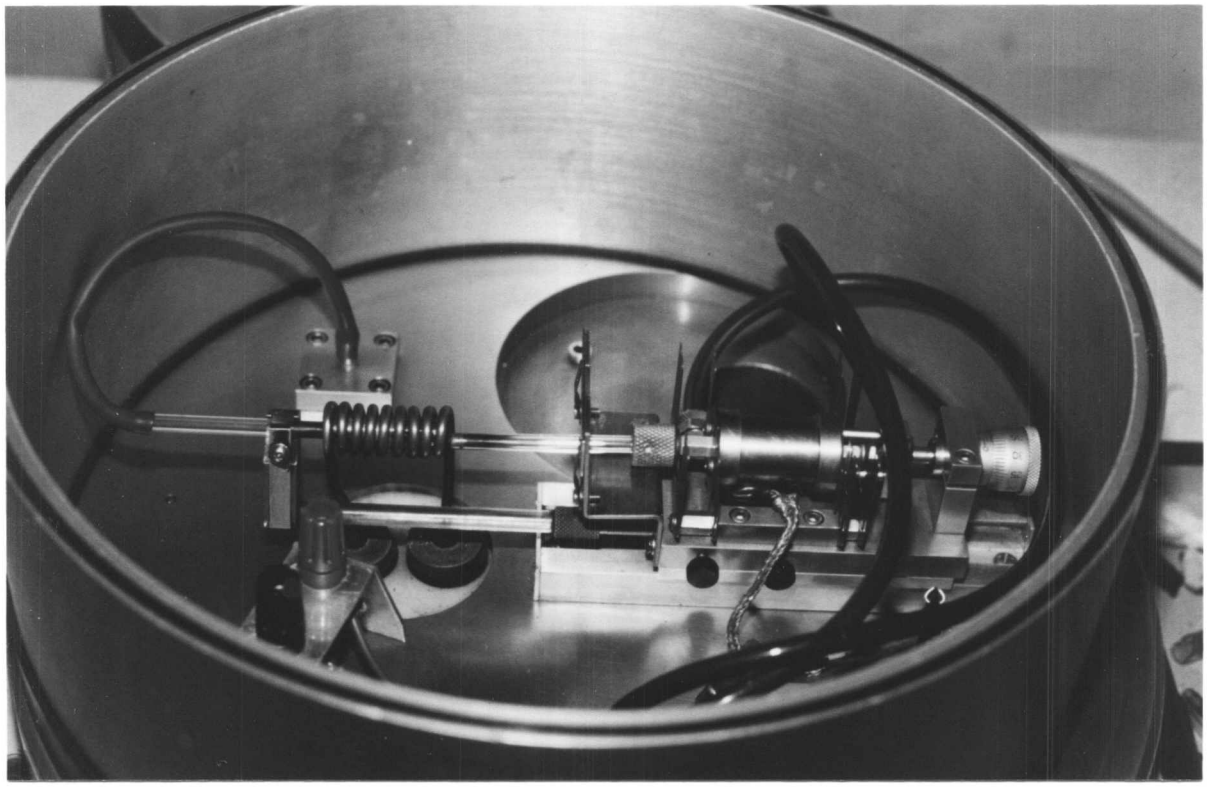

Fig. 4.1: Test chamber of the Theta Industries high speed dilatometer.

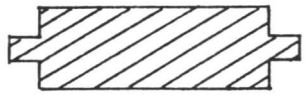

Fig. 4.2: A longitudinal cross section of the modified dilatometric specimen to prevent slipping and misalignment.

ferritisation temperature (> 1300°C) encountered in both isothermal and continuous cooling experiments, the shape of the generally used cylindrical specimens was modified to ensure alignment between the tips of the silica anvils and to prevent slipping, Fig. 4.2, and for the same reason, the computer program used in the analysis of dilatometer output also had to be modified to cope with higher temperatures. Specimen size was about 3.2mm diameter and 12mm length. Hollow specimens of 1.5mm bore diameter were sometimes used to ensure rapid cooling. Heating was carried out under vacuum and cooling after isothermal treatments was by introducing a jet of helium gas to the specimen.

For continuous cooling treatments a DATA TRACK PROGRAMME was used to follow a preplotted cooling curve on a rotating drum. This system allowed constant cooling rates from the ferritisation temperature to be maintained without the use of the helium quenchant at cooling rates slower than 8°C/sec. At cooling rates between 8°C/sec and 20°C/sec, gas quenchant was needed to maintain linear cooling rates. At cooling rates faster than 20°C/sec, constant cooling could not be maintained.

For isothermal experiments, a manual temperature control device was used to quench the specimen from its ferritisation temperature (about 1300°C) to the preset isotherm required. Rapid quenching was achieved by flushing a stream of helium gas through the specimen. This should be done carefully to avoid temperature overshooting by cutting off the quenching gas at a pre-set temperature above the isothermal transformation temperature.

The change in length of the specimen is transmitted to the transducer and nominally magnified 104 times. Both change in length and temperature are monitored on a chart recorder which moved with a pre-set speed. However calibration was always carried out for both magnification and chart speed to get more accurate results. A microcomputer is attached to the equipment which enables the collection of length change and temperature down to 10 msec intervals and was recently fitted with an interface to enable even smaller intervals to be accessed and to provide controlled cycles of heat treatments.

4.6.1 Ni Plating

Nickel plating is usually applied to carbon or low-alloy steel samples to suppress surface nucleation of ferrite mainly by preventing oxidation and possibly by reducing decarburisation and denitridisation. Ni plating was attempted in this project, (although it was borne in mind that it may enhance the nucleation of austenite) to investigate its

effect on the δ-ferrite to austenite transformation.

Both solid and hollow samples of duplex stainless steel weld metal W111 were nickel plated. The plating was carried out in two steps: (a) striking in (250 mg nickel sulphate, 27ml concentrated H_2SO_4 and water, all amounting 1 litre) solution at 50°C with a current density of 7.8 mA/mm^2 for six minutes; (b) plating in a solution made of 140g anhydrous sodium sulphate, 15g ammonium chloride, 20g boric acid and distilled water to add up to 1 litre in all, at 50°C with a current density of 0.4 mA/mm^2, for 15 minutes. The layer thickness after plating would be about 0.08 mm.

During heating at the ferritisation temperature (1300°C $\pm$ 10), the nickel plated specimen was observed to melt at the plated surface after which the specimen slipped in the protective quartz tube and the experiment was terminated. Observation of the melted surface Fig. 4.3 revealed a solidified microstructure. EDX microanalysis test results carried out on the same specimen showed an increase of nickel content in the region adjacent to the plating (Ni $\approx$ 13 wt%)

It is believed that the presence of a gradient of nickel along the cross section may have caused the formation of a eutectic with a melting point perhaps near the ferritisation temperature applied and it is possible that the spot welded point of the thermocouple may have played a role perhaps by picking up copper from the spot welding machine electrode. Hence, nickel plating was not used in subsequent dilatometric studies.

4.7 X-Ray Lattice Parameter Measurements

To check for the effect of alloying elements in duplex stainless steel and to provide data for the analysis of dilatometric results, it was necessary to measure accurately, the lattice parameter of δ-ferrite. A homogenised specimen of alloy SH (1250°C for 72 hr) was finely ground using a precision grinding machine to 1mm $\times$ 1mm $\times$ 1.5cm size and mechanically polished down to 1 micron using diamond paste. The specimen was then chemically polished in (25 ml HF + 25 ml H_2O_2 + 50 ml distilled water) solution to remove any surface deformation, after which it was placed in a diffractometer specimen holder and irradiated using a copper target X-ray source operating at 40kV and 30mA. The diffraction profile was recorded between 10 and 140°2θ at 1°2θ intervals. Peak positions were plotted against $\sin^2\theta$ and the lattice parameter was

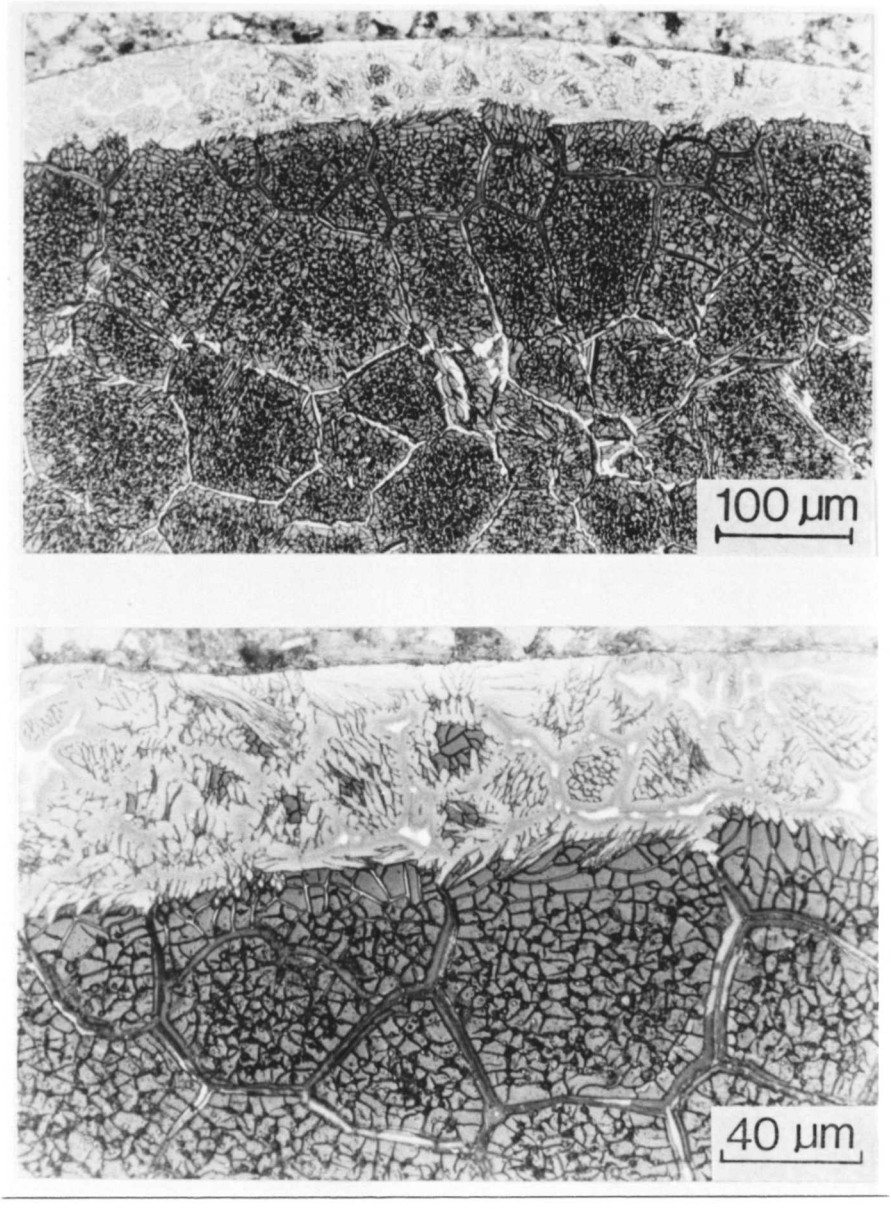

Fig. 4.3: Micrographs showing the microstructure of nickel plated dilatometric specimen after a failed isothermal treatment due to surface melting and subsequent slipping.

out at an accelerating voltage of 20kV and with the specimen tilted at an angle of 45° to the beam, enabling the X-rays to reach the silicon detector. The electron probe beam diameter size was about $1\mu m$. Standard correction procedures for the effects of atomic number, absorption and flourescence (ZAF) were used in the analysis of results [2]. The technique is unable to measure the carbon and nitrogen concentrations.

4.11 Transmission Electron Microscopy

Transmission electron microscopy was carried out on thin foil specimens using a Philips EM 400T electron microscope operated at 120 kV. Thin foil specimens were prepared from 0.25 mm thick discs slit using a high precision slitting wheel and coolant to avoid heating during slitting. The discs were thinned down to 0.05mm, by low pressure abrasion on silicon carbide paper. The final thinning was carried out in a twin jet electropolisher. The polishing solution was a mixture of 7% perchloric acid and 23% glycerol in ethanol at -5 to $-7°C$, at an applied voltage of 30 to 40V. Some difficulty was faced when electropolishing welded metals as the inclusions tended to fall out and with specimens aged for long time periods precipitates such as sigma phase were often observed to be heavily etched.

4.12 "Seescan" Image Analysis

In addition to dilatometry, the volume fractions of austenite were measured from optical specimens using the mean lineal intercept and image analysis methods. The metallographic image istransferred by the means of a video camera from either a photograph or directly from the specimen to a TV screen. To allow it to be converted to computer format for processing, the image is first digitised. It is changed from a continuously varying signal to an array of points, where each point is assigned a grey level. The task programming language (TPL) used permits 128 grey levels, where 0 represents black and 127 represents white [3].

The array is assigned coordinates; the origin is in the top left hand corner Fig. 4.4 (this is because of the way in which TV rate signals are scanned), and the TPL assigns an X axis of 0 to 255 and a Y axis of 0 to 255.

The volume fraction is measured by means of a frame measurement made on regions delineated by a circular or rectangular frame. The processed image is thresholded; a process by which the number of pixels within a range of grey shades in the frame is calculated. The total area of all the the regions within the frame that have been selected using a grey scale threshold are also determined to enable fractions to be cal-

References

1. Cullity, B. D. 'Elements of X-Ray Diffraction' (1978) London, Addison-Wesley Publishers, p. 350.

2. Reimer, L. 'Scanning Electron Microscopy' (1985) Berlin, Springer-Verlag publishers, p. 365.

3. 'Seescan Image Analysis Instruction Manual' (1988) University of Cambridge, Dept. of Mat. Sci. and Metallurgy.

Chapter 5

EXPERIMENTAL STUDIES ON THE DEVELOPMENT OF MICROSTRUCTURE IN DUPLEX STAINLESS STEEL WELD METALS

5.1 Solidification

All duplex stainless steel multirun welds studied in this project were found to solidify completely to δ-ferrite as the primary phase, by epitaxial cellular growth from the solid base plate at the fusion surface. The resulting microstructure was found to consist of columnar grains which grew continuously across the weld cross-section, from the root bead to the top bead (Fig. 5.1). The same δ grains are able to propagate across several beads because there is always some δ left untransformed even at room temperature, and this can continue to grow as yet another layer is deposited. This contrasts with low-alloy welds, in which the δ-ferrite transforms completely to austenite on cooling, and hence has to be renucleated as a new layer is deposited so that there is no continuity of the columnar grain structure across the beads. The top bead, which is deposited last, is usually named the "as-welded" region since it is the only unreheated part of the weld, and its microstructure is shown in Fig. 5.2.a. It consists of columnar δ-ferrite grains decorated with more or less continuous layers of allotriomorphic austenite, with networks of Widmanstätten austenite emanating from the allotriomorphs. The apparent length of these plates was found to vary from 3 μm to about 400 μm, the latter being the approximate width of the δ-ferrite columnar grains. Under electron microscopy, Widmanstätten plates were observed to possess a widge shaped tip similar to its counterpart in low-alloy steel (Fig. 5.2.b).

Fine intragranular austenite particles were often observed within the interior of the δ-ferrite grains. Subgrains were also found, particularly in the banded regions of the as-welded microstructure. Such banding is caused by solute segregation during nonequilibrium solidification.

In the reheated zones (Fig. 5.3), the volume fraction of the austenite was always found to be higher than that of the as-welded region. The difference was dependent on the distance of the reheated zone from the subsequent welding pass; this follows from the fact that this microstructure is a function of the temperature field experienced at each point in the reheated zone. Apart from the allotriomorphic austenite, two further distinctive morphologies could be observed in the reheated zones. One of these

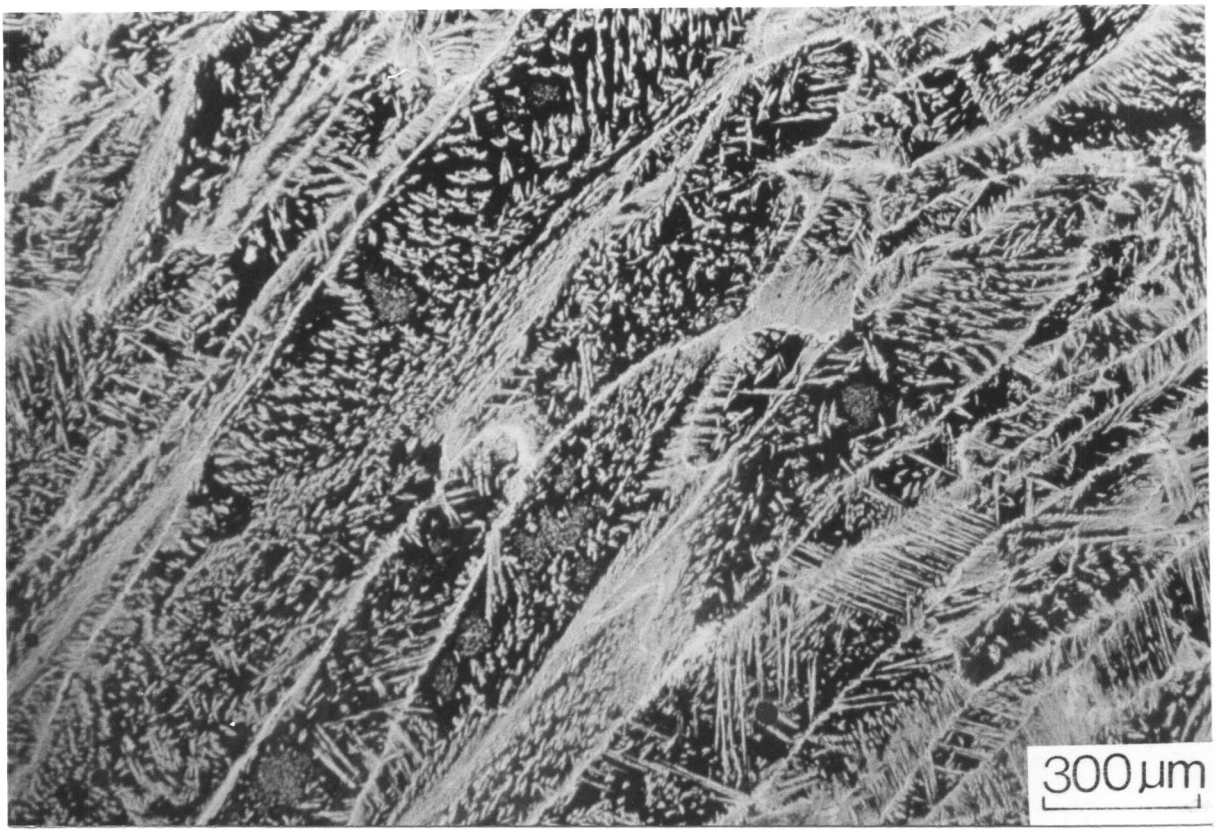

Fig. 5.2.a: The microstructure of the last bead to be deposited (*i.e.*, the as-welded microstructure) of alloy WR4. The lighter etching phase is the austenite.

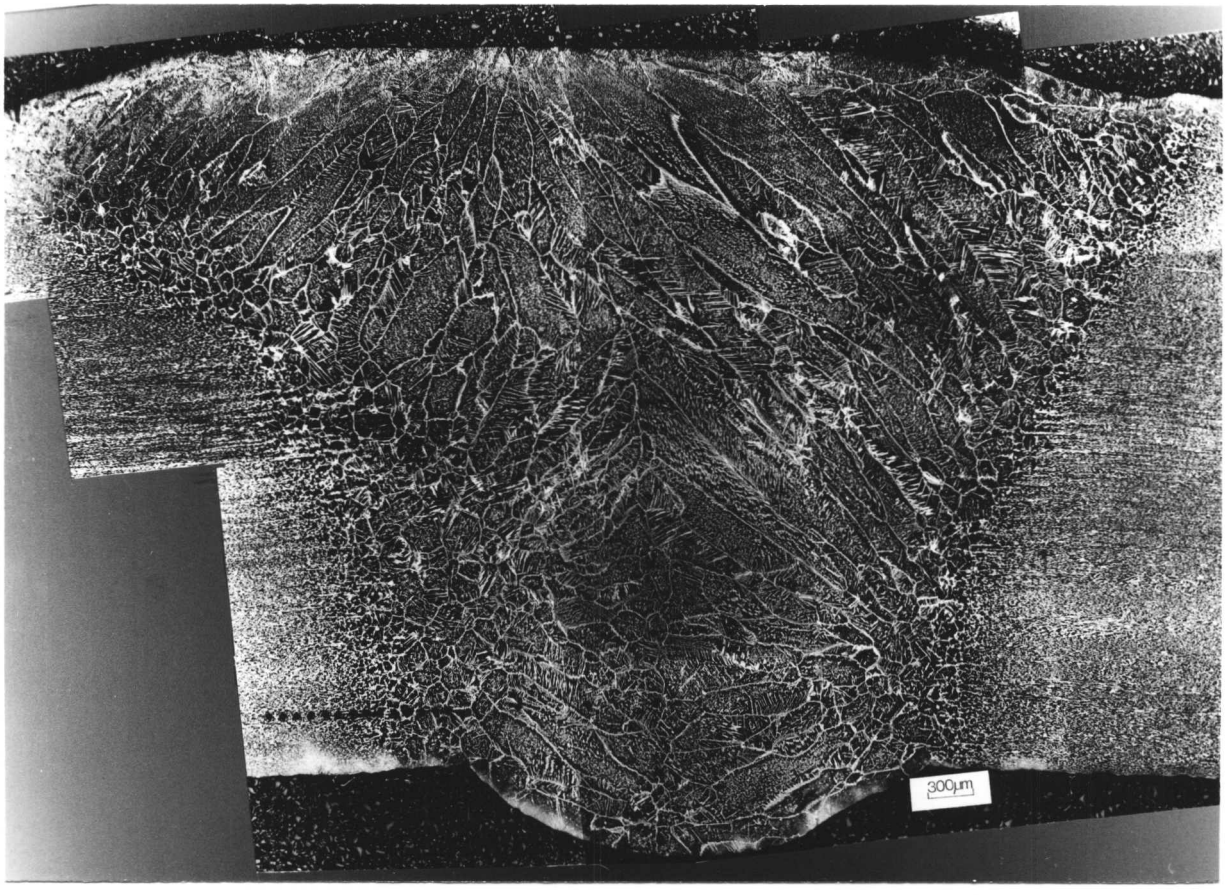

Fig. 5.1: Composite optical micrograph of a complete weld cross section in sample SP2, displaying clearly the epitaxial growth from the heat affected zone and the continuity of the columnar δ-ferrite grains across different layers. The austenite is the light etching phase and the δ-ferrite is the darker phase.

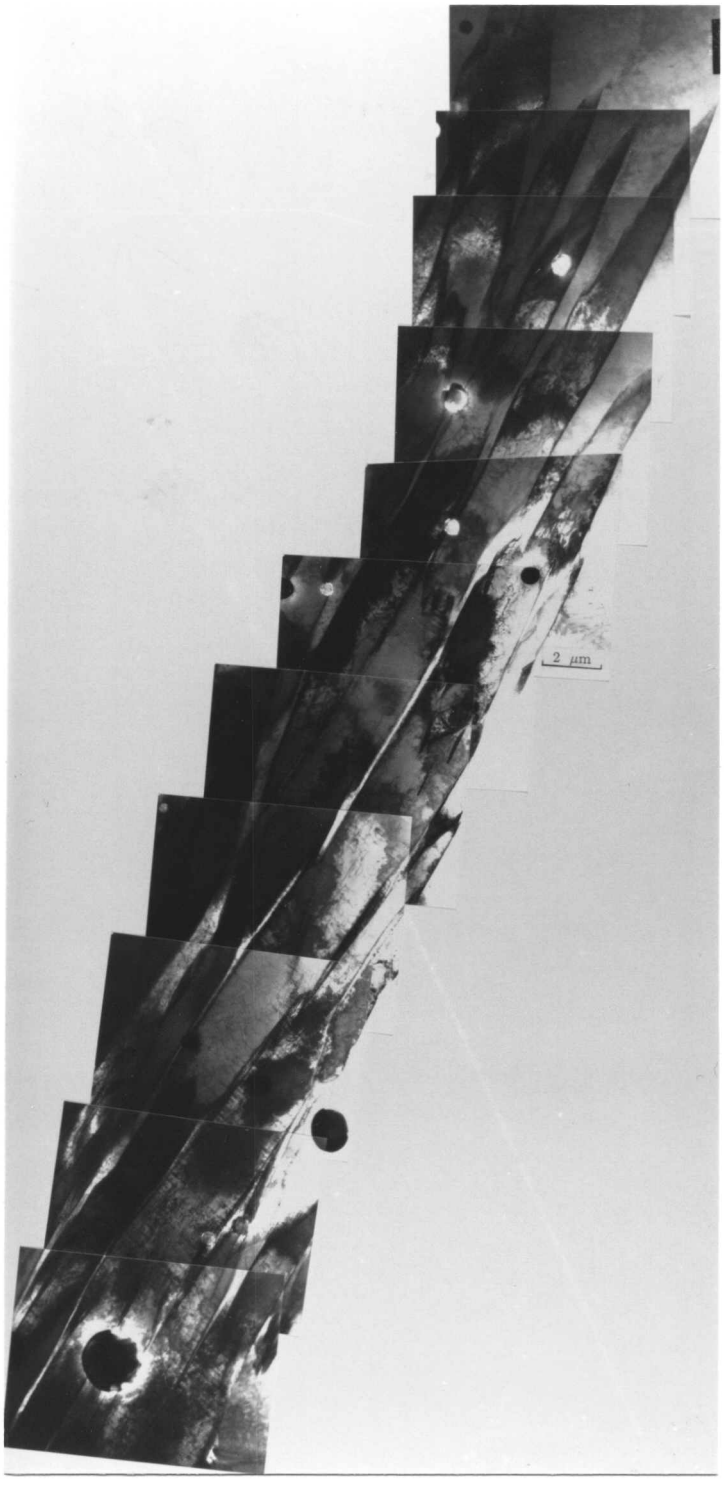

Fig. 5.2.b: Composite TEM micrograph of Widmanstätten austenite plates observed in the as-welded region of sample BW.

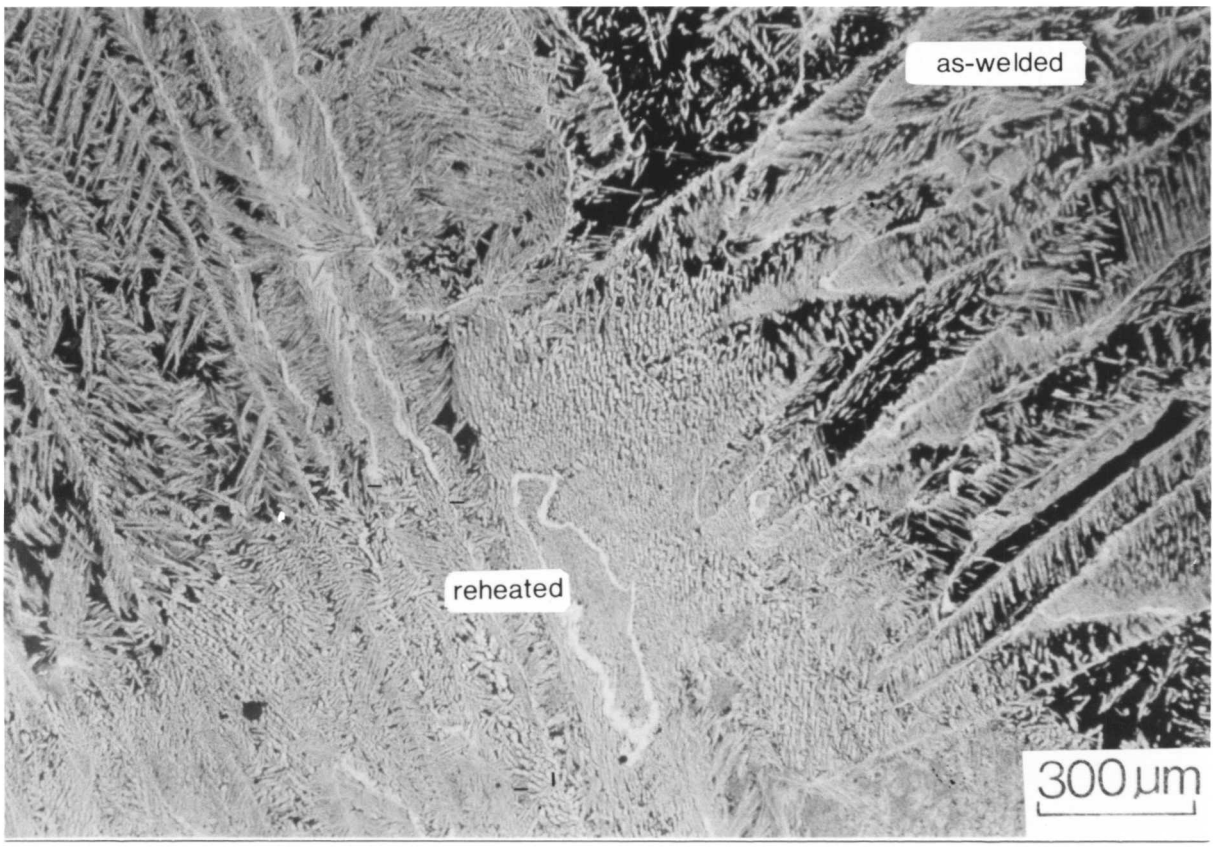

Fig. 5.3: The microstructure of the re-heated zone of alloy WR4. The lighter etching phase is austenite.

is the large austenite particles of parallelpiped cross sections and planar interfaces, sections which are believed to be of the Widmanstätten austenite particles which originate from the γ allotriomorphs. The second morphology consists of very fine acicular austenite particles formed intragranularly with a morphology of thin plates. A few particles of this morphology were observed in the as-welded zone as mentioned earlier in this chapter.

Most of the acicular austenite was observed to form on nonmetallic inclusions, Fig. 5.4.a. The detailed morphology and nucleation of these fine austenite particles and their interlocking microstructure are illustrated in Fig. 5.4.b and Fig. 6.47 (chapter 6). The morphology resembles that of the acicular ferrite formed in HSLA weld metals, justifying the nomenclature "acicular" austenite by analogy. One further comparison that can be made with acicular ferrite in low-alloy welds is as follows. Chart *et al.* [1] have shown that the chance of observing an inclusion in a plate on a two dimensional random section can be rather small. It is given approximately by the cubic root of the ratio of inclusion volume to plate volume. This means that under typical conditions, for low alloy steels, only about 13% of the plate sections observed might exhibit an inclusion, even though all plates may in reality contain such inclusions. All the same, the chance of observing the nucleating inclusions appears rather large for the duplex stainless steel as illustrated in Fig. 5.5. This must be a consequence of the higher inclusion contents of duplex stainless steels and of the relatively smaller volume per plate of acicular austenite associated with the high chromium content.

As mentioned earlier, in duplex stainless steel the dominant solidification mode is to primary δ-ferrite. However, deposition of duplex stainless weld metal on a dissimilar base plate, such as carbon steel or austenitic stainless steel, can alter the solidification mode. This matter has been investigated by Suutala *et al.,* [2] (chapter 3). In the buttered duplex stainless steel weld metal BW, a drastic change of microstructure was observed across the field from the weld metal to the carbon steel base metal ranging from a mixture of δ-ferrite and austenite, to martensite, to pearlite and ferrite. At the fusion boundary, a narrow zone of almost fully austenitic metal, followed by a mixture of austenite and "skeletal" ferrite was observed (Fig. 5.6). A change in the δ-ferrite from "skeletal" to vermicular to lathy morphologies was also noticed. Layers of martensite were observed to form between the mixtures of austenite and fine δ-ferrite which formed at the early stages of solidification (Fig. 5.7). It

Fig. 5.4.a: Optical micrograph showing the microstructure of the as-welded top layer of alloy BW. The light etching phase is the austenite.

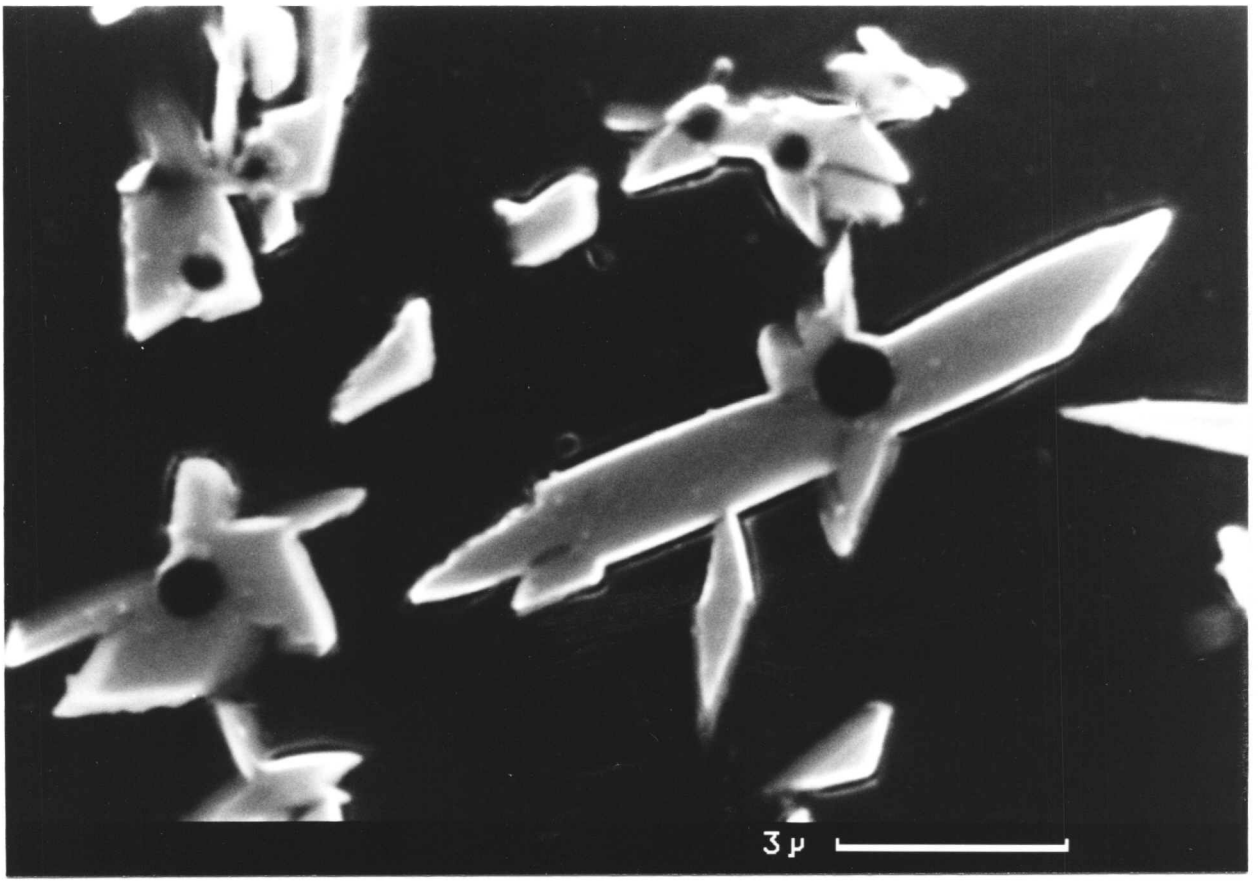

Fig. 5.4.b: Scanning electron microscope image of acicular austenite plates formed on inclusions in alloy BW. Note the presence of inclusions in the austenite clusters.

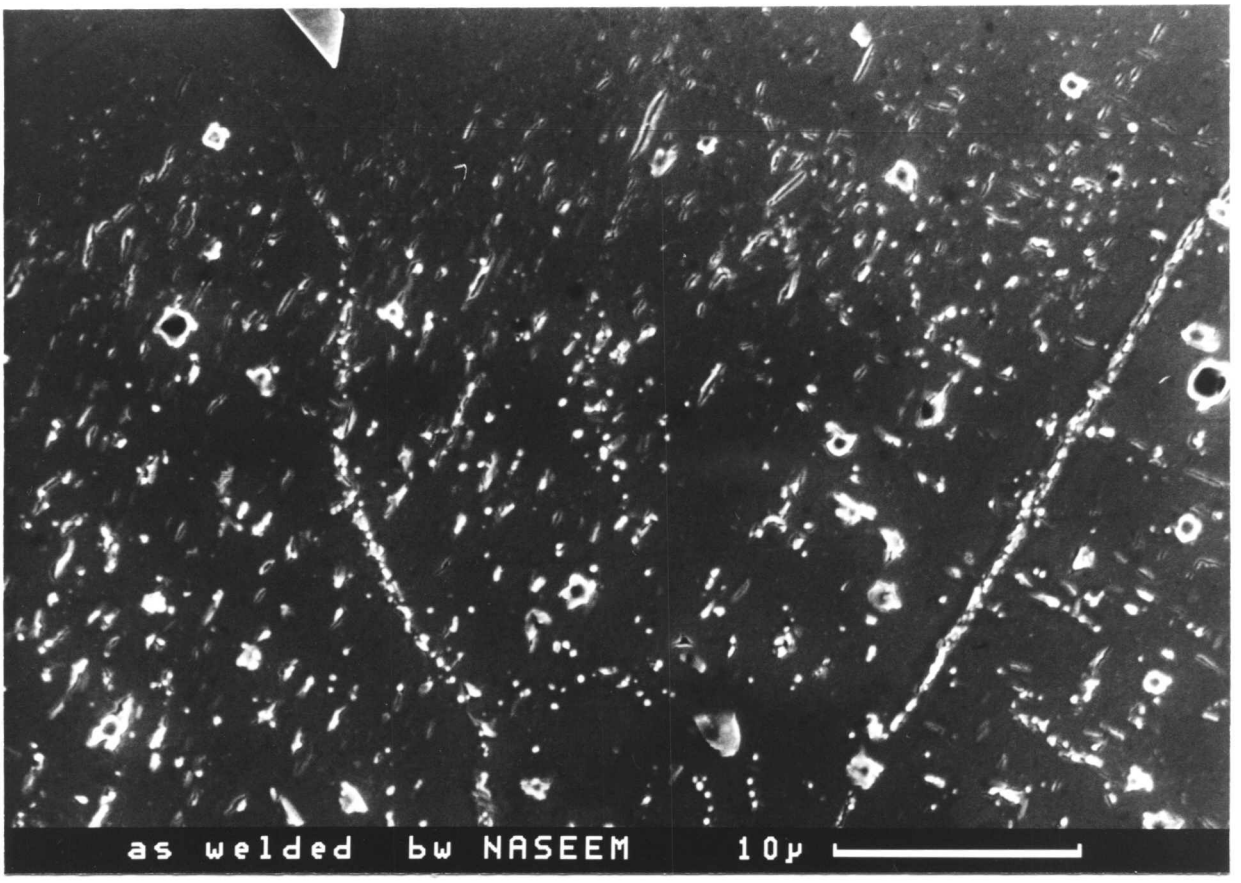

Fig. 5.5: Scanning electron microscope image of the microstructure of the banded zones of the as-welded top layer in alloy BW. The austenite is the white etching phase and the δ-ferrite is the black phase.

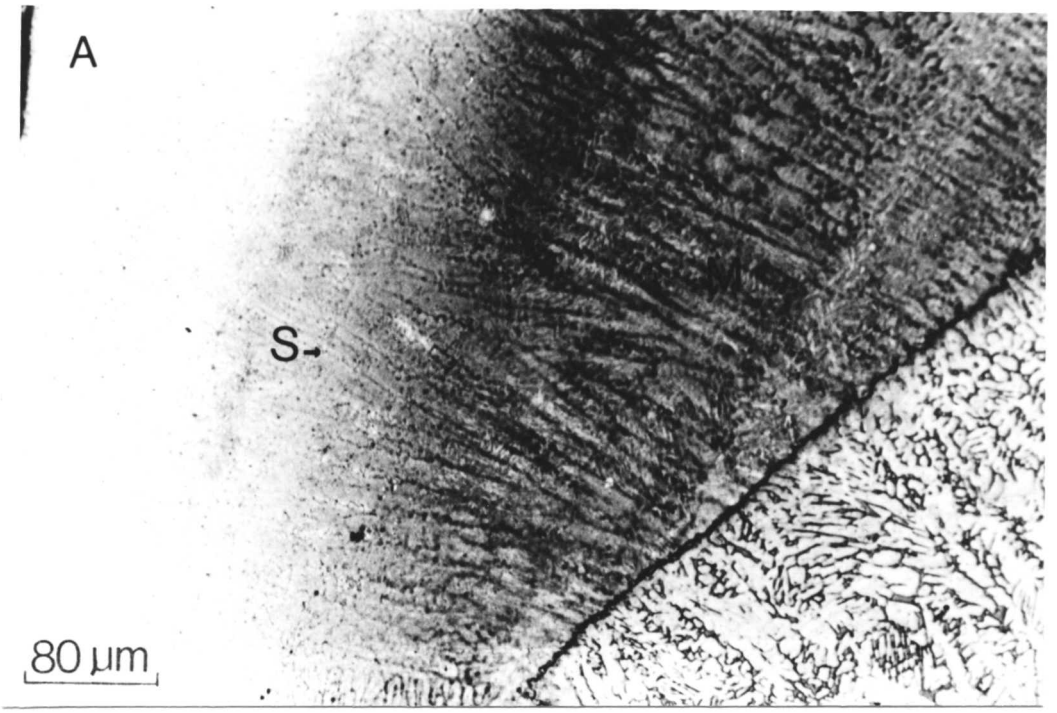

Fig. 5.6: Optical micrograph showing the formation of a narrow zone of a fully austenitic microstructure (A) at the fusion zone (left), followed by a mixture of austenite and skeletal δ-ferrite (S), in alloy BW.

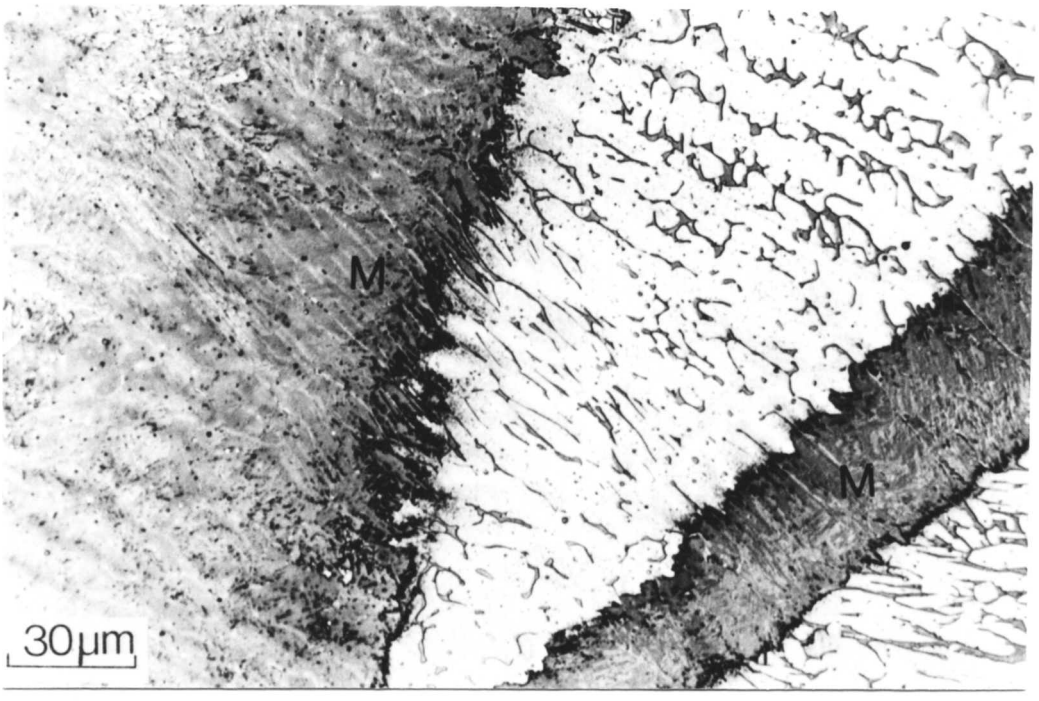

Fig. 5.7: Optical micrograph showing a martensite band (M) in the vicinity of the fusion surface, as a result of dilution of solutes across the interface during the nonequilibrium solidification of weld metal BW.

is believed that this martensite was formed from a region solidified to primary austenite as a result of dilution with the base plate. The microanalysis test results (Table 5.1) provide additional evidence on this point; the chromium and molybdenum contents in the martensitic region were found to be smaller compared with those of the δ-ferrite in the adjacent region. The effect of dilution of the interstitial solutes, particularly carbon, must also be important since it's concentration is expected to be higher in the regions which solidified first in the vicinity of the fusion surface. While carrying out a surface relief experiment on a sample of alloy BW, in an attempt to characterize the mechanism of $\delta \rightarrow \gamma$ transformation, an invariant-plane strain surface relief characteristic of displacive transformation, was observed in the martensitic region (Fig. 5.8), consistent with the above discussion. The measured hardness of the observed martensite was 720 HV5.

Table 5.1: Effect of dilution on composition of BW (atomic%). The atomic percent value stated ignores the presence of any interstitials. (Accuracy $\pm 2\%$)

Region	Fe	Cr	Ni	Mo	Mn	Si
martensite	72.1	15.7	5.5	1.4	0.75	0.94
δ-ferrite	68.7	22.7	4.2	2.4	0.79	1.1
austenite	69.7	19.6	7.15	1.36	1.02	1.05

Duplex stainless steel weld pad WR2, which was deposited on an austenitic stainless steel using a manual MIG welding process, was found to have undergone a change in the weld pool chemistry, caused by dilution with the base plate, and an accompanying change in solidification mode. It is believed that solidification commenced with the formation of primary δ-ferrite, but completed by an interdendritic eutectic solidification mechanism, as a result of the enrichment of the liquid metal ahead of the interface by the austenite forming elements such as nickel and carbon which have a limited solubility in the δ-ferrite. On further cooling, the last solidified austenite grows very quickly at the expense of the primary δ-ferrite leaving behind a δ-ferrite distribution exhibiting a vermicular shape (Fig. 5.9). Subsequent passes of WR2 weld metal changed back to the dominant primary δ-ferrite solidification mode as a result of diminished dilution.

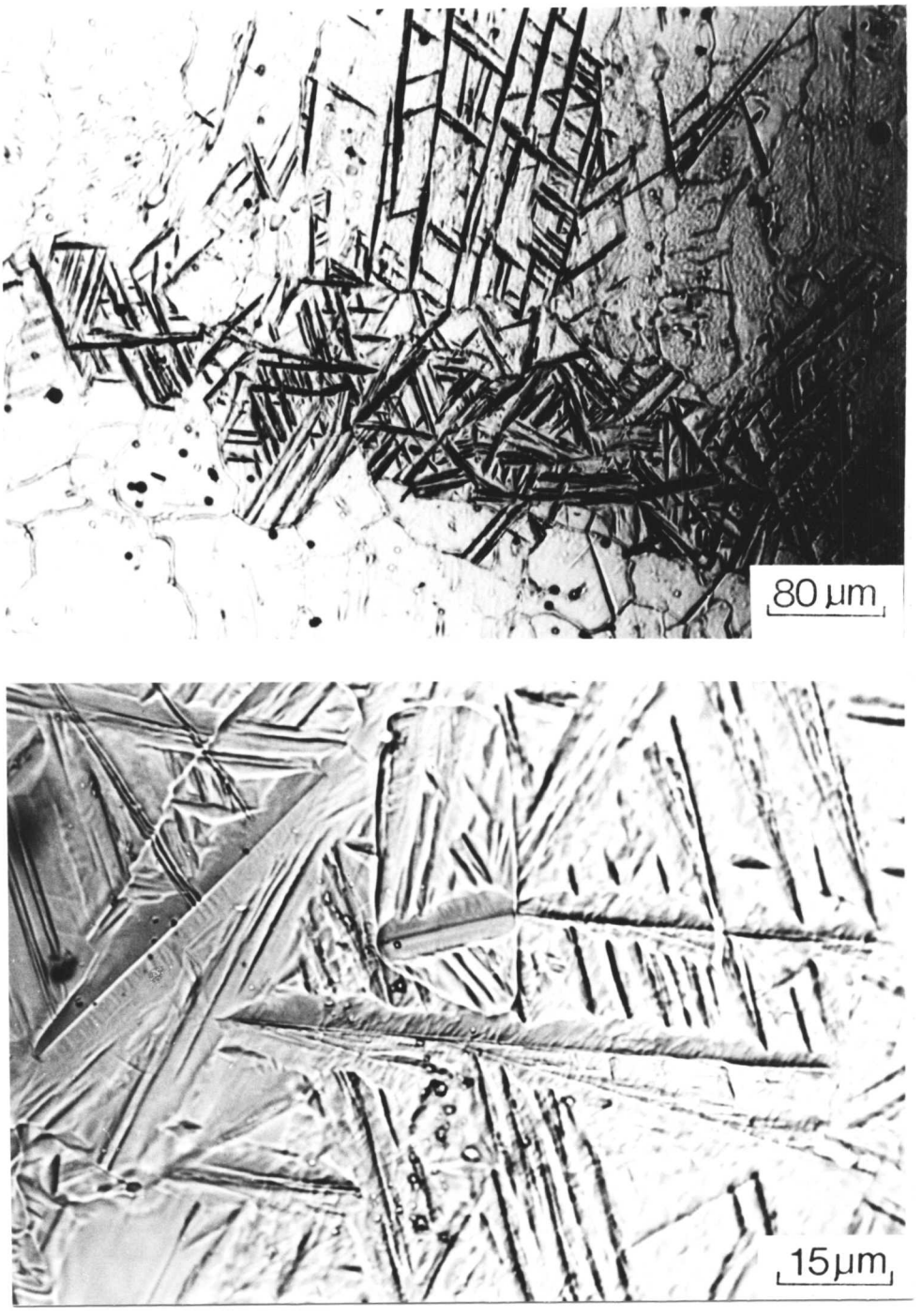

Fig. 5.8: Micrograph showing the tent shaped surface relief associated with the martensitic bands found near the fusion line in alloy BW. The specimen 10 × 10 × 10 mm in dimension, was heated at 1320°C for 5 minutes, isothermally transformed at 1000°C for 15 mins then quenched in iced brine.

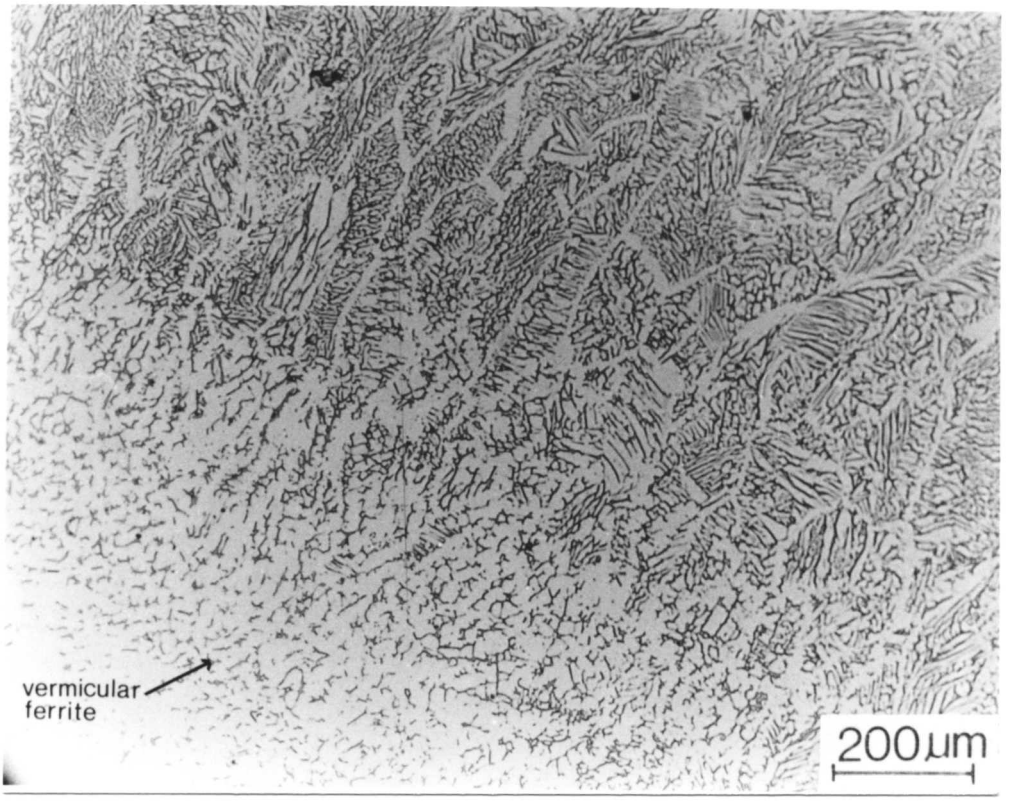

Fig. 5.9.a: Optical micrograph displaying the change of δ-ferrite morphology in alloy WR2 from a vermicular to a lathy shape as a consequence to the change of solidification mode from primary δ-ferrite + interdendritic austenite at the fusion line to just δ in the subsequent passes.

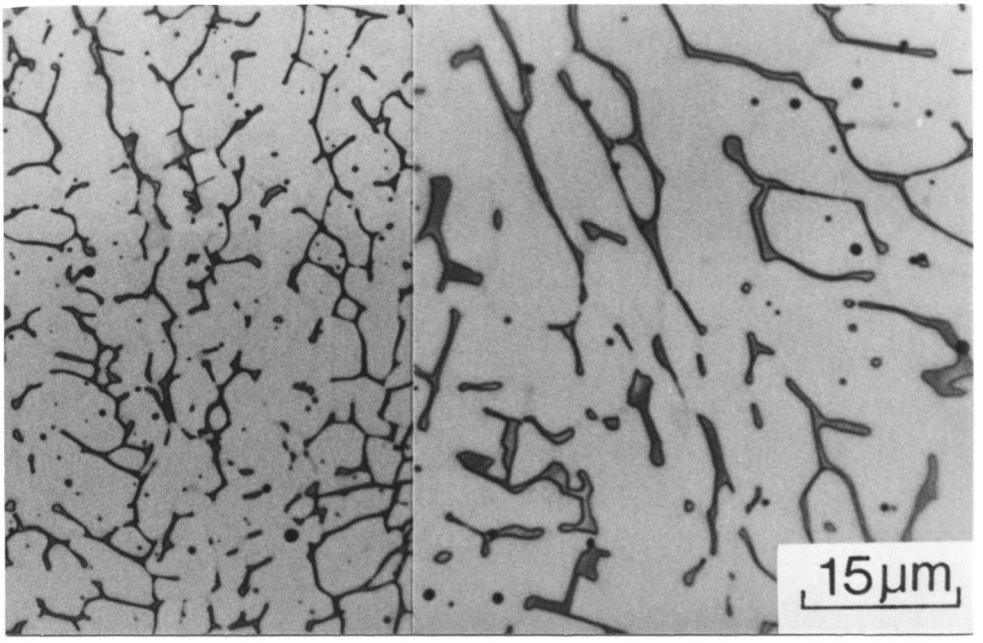

Fig. 5.9 b: Optical micrograph showing the vermicular ferrite morphology in weld metal BW. The dark etching phase is δ-ferrite.

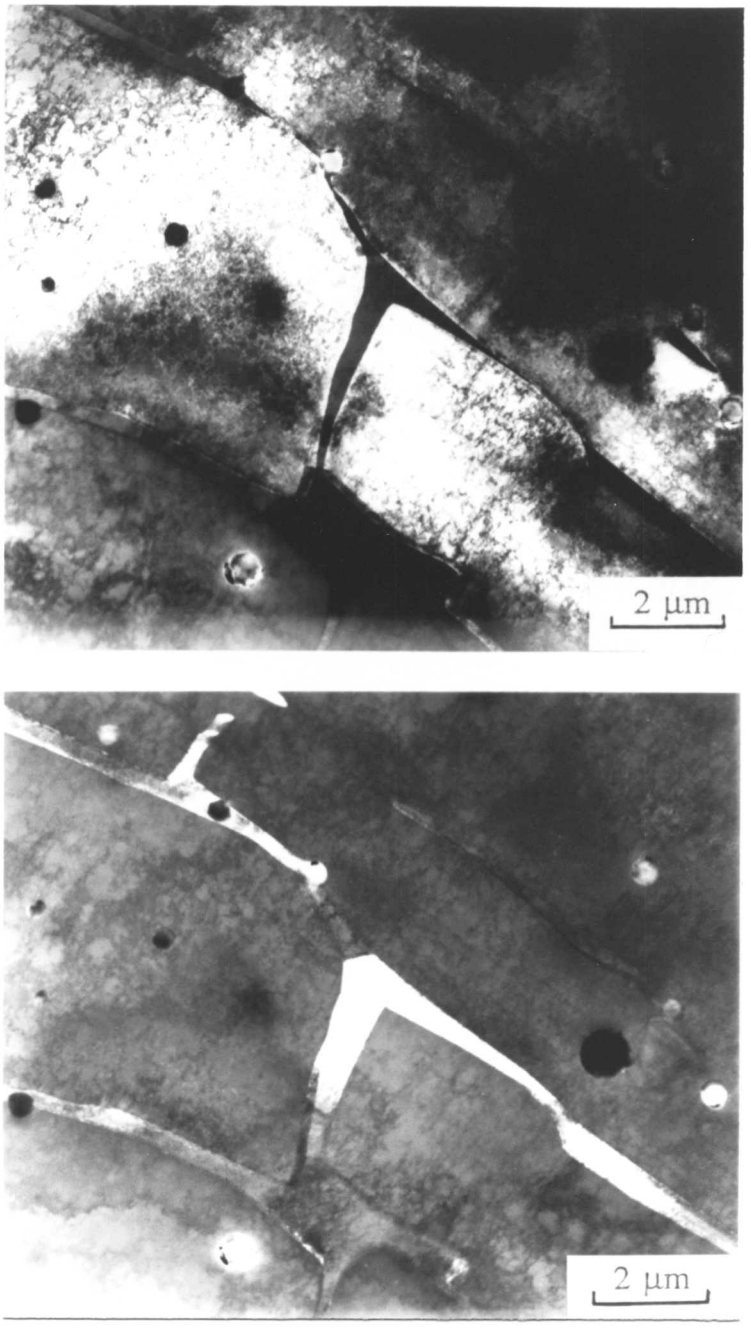

Fig. 5.9 c: TEM bright and dark field images of the vermicular ferrite morphology in duplex stainless steel weld metal.

5.2 The Overall δ-Ferrite Content

The volume fractions of the δ-ferrite to be expected in the welds studied were estimated using the Schaeffler [3] diagram; the results are presented in Table 5.2. The estimated values seem to agree reasonably with those measured, using the image analysis method explained in chapter 4, to within 5 %. For the two pass weld metal SP1, a difference of 0.25 in the measured volume fraction of ferrite was obtained between the top and root bead. In the multirun submerged arc weld metal WR4, a difference of 0.2 volume fraction δ-ferrite was obtained between the as-welded and reheated zones. Similar results were obtained with the other weld metals tested. It is quite obvious that the Schaeffler diagram, which is based solely on the effect of the weld metal chemistry and which does not account for the effects of the cooling rate and the thermal cycles experienced by the reheated zones, can not be expected to be the best tool for the prediction of the microstructural constituents in duplex stainless steel weld metals. Another factor which is believed to be of importance in the metallurgy of duplex stainless steel weld metals in general, and which is not accounted for in the Schaeffler diagram, is the effect of the inclusions on the development of the microstructure. Weld metals usually contain relatively high volume fractions of inclusions owing to the fact of their rather high oxygen contents. The size and shape of the inclusions varies with the oxygen content and the welding processes [4]. It is believed that many of these finely dispersed inclusions are beneficial in providing heterogeneous nucleation sites for favoured phases, such as acicular ferrite in high strength low alloy (HSLA) weld metal [4,5]. In this project, as mentioned earlier, most of the fine acicular austenite formed in the as-welded microstructure was found to grow from inclusion nucleation sites.

Table 5.2: Estimated and measured δ-ferrite volume fractions.

Specimen	estimated	measured as-welded	measured reheated
SP1	0.58	0.65 ± 0.04	0.42 ± 0.03
WR4	0.54	0.57 ± 0.04	0.28 ± 0.02
BW	0.63	-	-
WR2	0.60	-	-

5.3 Microanalysis

As a consequence of the non-equilibrium conditions under which solidification and subsequent solid state metallurgical reactions take place in weld metals, phenomena such as microsegregation occur which may lead to the development of inferior mechanical properties. To investigate the degree of chemical heterogeneity in the duplex stainless steel weld metals, microanalysis surveys were carried out using the EDX facility of the scanning electron microscope "S4". The results obtained are illustrated in Fig. 5.10. The results for iron, chromium, nickel, molybdenum, silicon and manganese demonstrate that significant chemical variations exist all across the top and root beads of the cross section as a result of microsegregation in the two-run weld metal SP1. The interesting result is that apart from iron and molybdenum the substitutional solutes did not seem to partition to any great extent between the γ and δ phases. This may be a consequence of their low partition coefficients or may be a kinetic effect which will require further investigation. In fact, an examination of the data for an element like Mn or Ni shows that there are cases where sometimes the parent phase is richer in solute whereas on other occasions the product phase is enriched.

These data are difficult to interpret from a fundamental point of view, since they probably represent superimposed effects of segregation and partitioning, combined with continuous cooling transformation behaviour. Nevertheless, the case for molybdenum is clear in that it exhibits a large tendency to partition into the δ-ferrite, and the results serve to illustrate the expected level of heterogeniety. It is notable that the difference in molybdenum concentrations in δ and γ is complemented by approximately equivalent though opposite differences in their corresponding iron concentrations. This is again consistent with the observation that the other alloying elements do not partition to any large extent under the circumstances of the weld fabrication.

Similar results on segregation and partitioning behaviour were obtained for the as-welded region of multirun weld metal BW (Fig. 5.11). Microanalysis test results of welded alloy WR4 (Table 5.3) revealed no considerable partitioning in the substitutional solutes apart from molybdenum, which supports the hypothesis forwarded

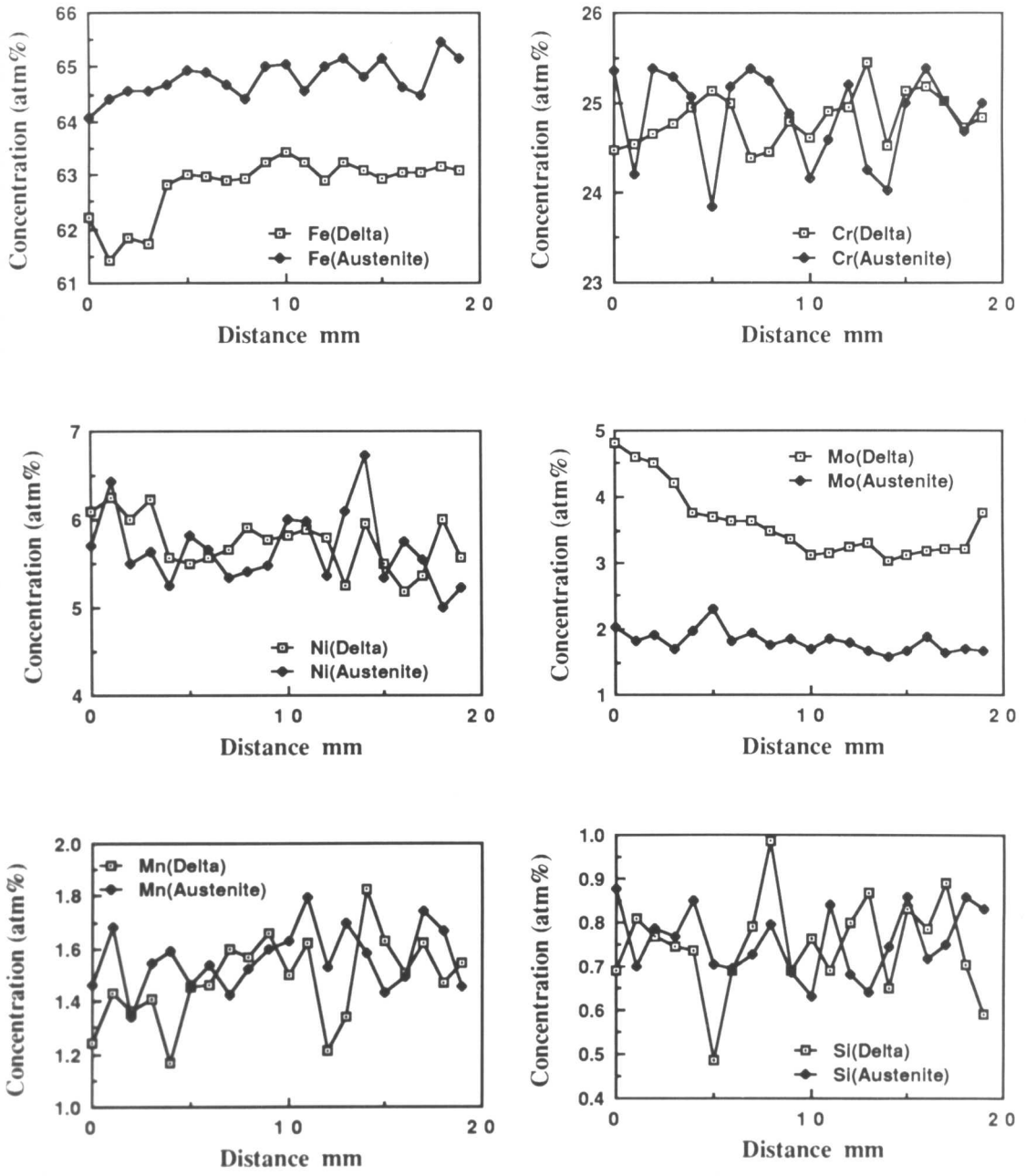

Fig. 5.10: Microanalysis survey of substitutional solutes carried out on a cross section of two-run weld metal SP1, from top down to root bead. Microanalysis results were obtained from EDX technique using S4 ' scanning electron microscope in which the presence of any interstitials is ignored. The standard errors 2σ are: Fe ($\pm$0.5), Cr ($\pm$0.4), Ni, Mo, & Mn ($\pm$0.2), Si ($\pm$0.05) atm.%.

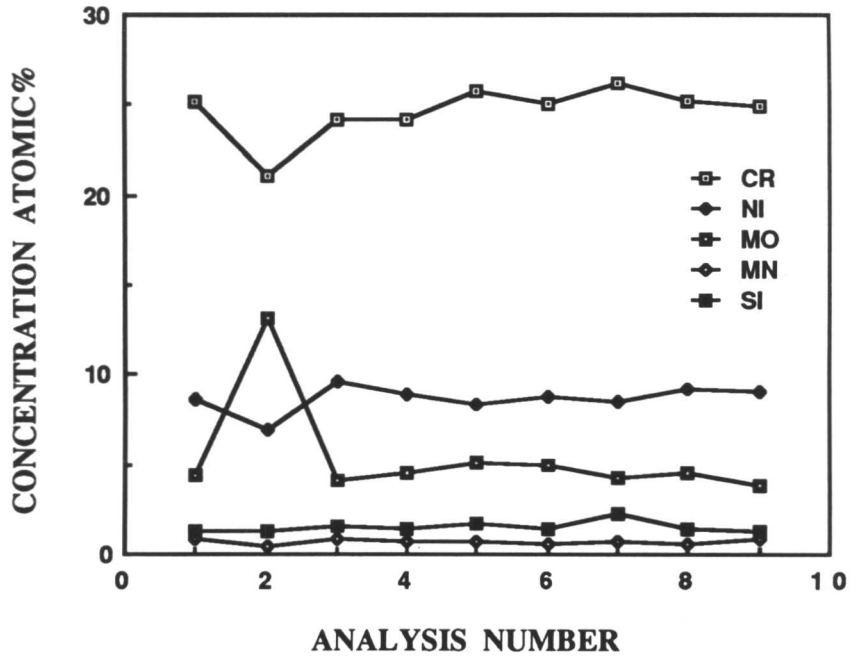

Fig. 5.11: Microanalysis survey of substitutional solute in atomic percent from the top bead downwards carried out on a cross section of buttered weld BW. The concentrations shown ignore the presence of any interstitials. The results were obtained by EDX analysis on a scanning electron microscope. The standard errors 2σ are: Fe (± 0.5), Cr (± 0.4), Ni, Mo, & Mn (± 0.2), Si (± 0.05) atm.%.

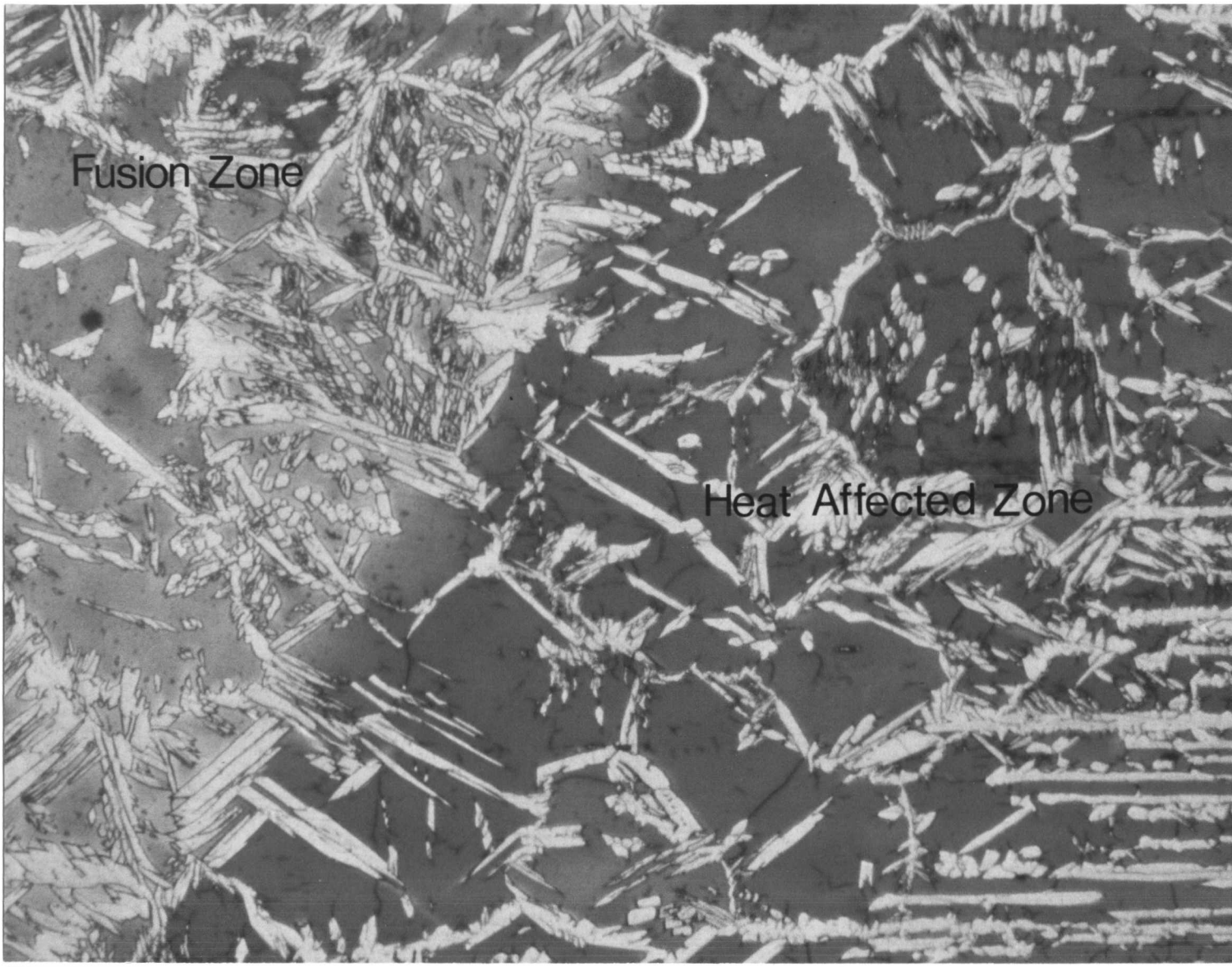

Fig. 5.12 a: The microstructure of the weld zone, heat affected zone and the base plate in weld metal SP1. sub-grains of δ-ferrite in the heat affected zone. The light etching phase is austenite.

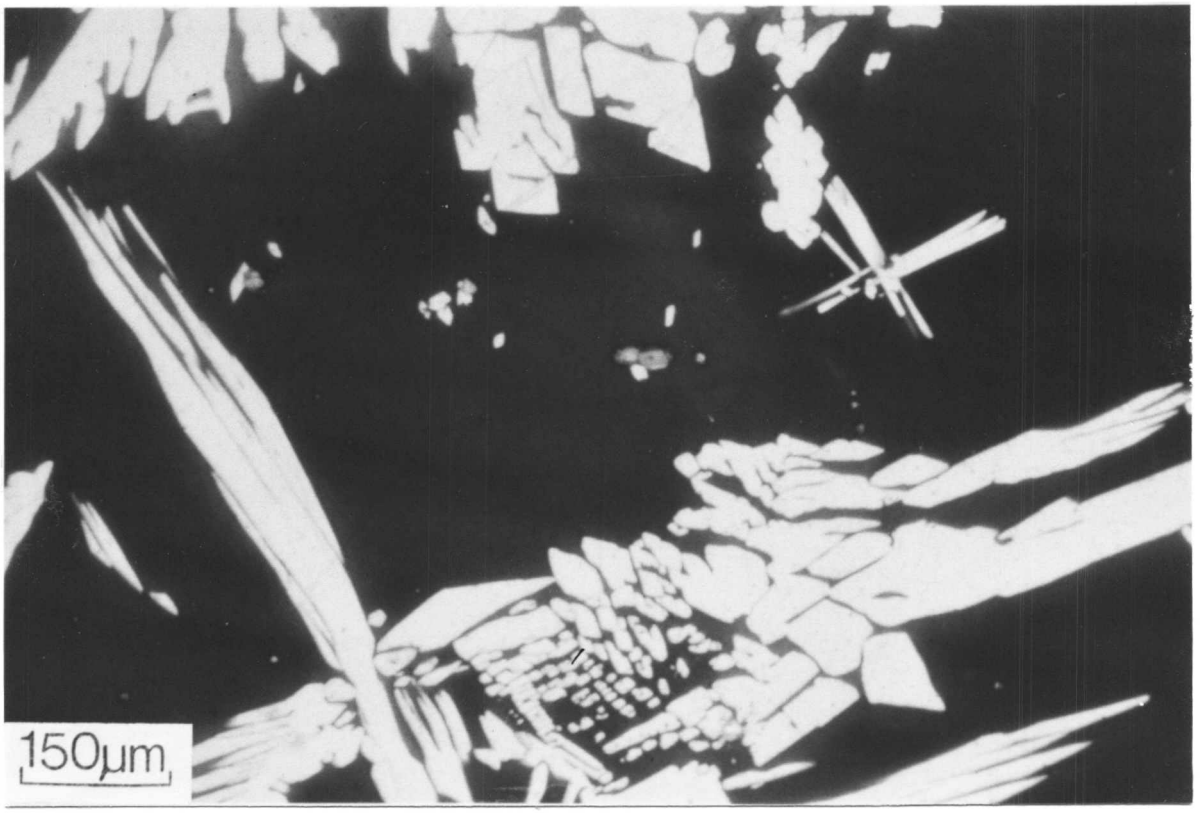

Fig. 5.12.b: Formation of austenite particles on inclusions in the heat affected zone of weld SP2.

per unit volume, for the formation of austenite. Indeed, Fig. 5.12 a shows clearly that most of the available sites are rapidly exhausted as layers of allotriomorphic austenite saturate the δ/δ grain boundaries.

The partially ferritised region in the parent plate is adjacent to the grain growth region. It usually still possesses some of the microstructural features of the original parent metal: elongated austenite and δ-ferrite grains, the only difference being the spacing of these elongated grains in the transverse direction. The width of this region depends mainly on the temperature isotherm reached during heating and whether it is high enough to cause any deviation from the equilibrium volume fractions of the two phases. It is generally accepted that as long as the austenite particles are not dissolved on heating, there is little or no δ-ferrite coarsening [7].

5.5 Microstructure - Hardness Relationship

The microhardness surveys carried out on the weld metals under investigation, and their heat affected zones are shown in (Figs. 5.13 & 5.14). They demonstrate the importance of the microstructural constituents on the related properties of the weld metals and their heat affected zones. A higher volume fraction of δ-ferrite in the top bead and the heat affected zone correspond to a higher hardness. A higher austenite content in the root beads and the reheated zones of the multirun weld metals is associated with a decrease in hardness. A trend indicating that the higher the austenite content the lower the hardness can be deduced from the results shown in Figs. 5.13 & 5.14, although weld metal BW produced by a manual metal arc welding technique does not seem to follow this trend, perhaps because of the variations in welding parameters associated with the technique, as reflected on the microstructural constituents. Nevertheless, the results of microhardness tests carried out on individual phases (Table 5.4) show that the δ-ferrite is harder than austenite in most of the specimens tested apart from SP1 in the as-welded top layer. The difference between the ferrite and austenite hardnesses is not large possibly because of higher hardness of austenite due to precipitation events occuring within the austenite. Recent investigation [8] on the effect of molybdenum in nitrogen-enriched duplex stainless steel, using atom probe field ion microscopy, revealed the existence of Mo-N complexes within the austenite phase. The dense despersion of these complexes within the austenite is believed to be responsible for the large strengthening of nitrogen-enriched duplex stainless steel.

a

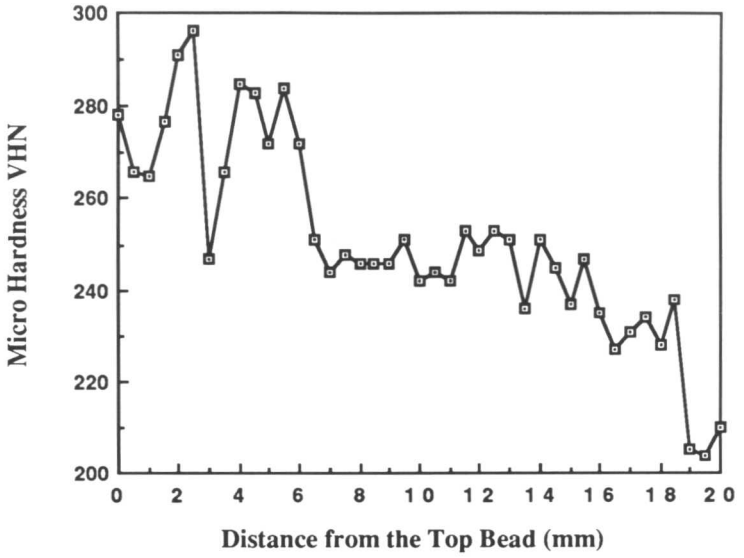

b

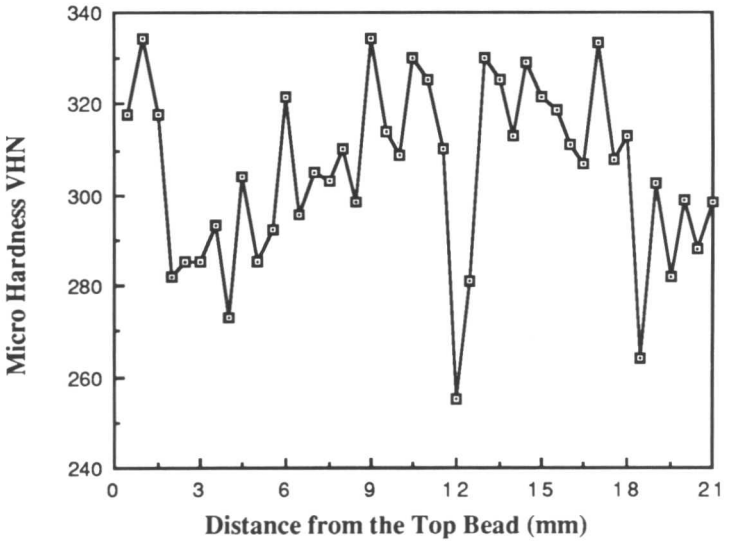

Fig. 5.13: Microhardness survey from the top to the root bead:

(a) Weld metal WR4;

(b) Weld metal BW. The indentation force was 0.98 N.

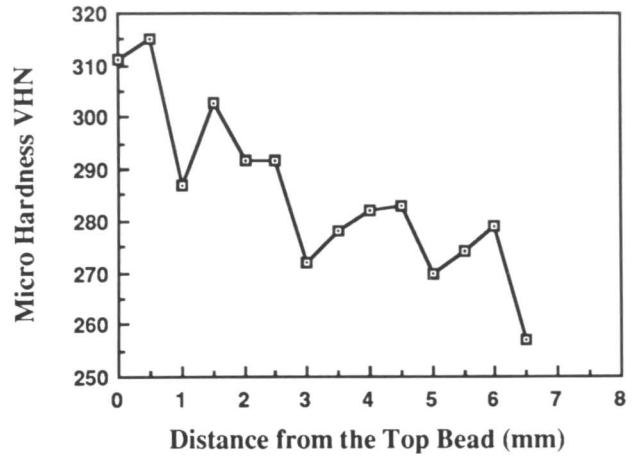

a

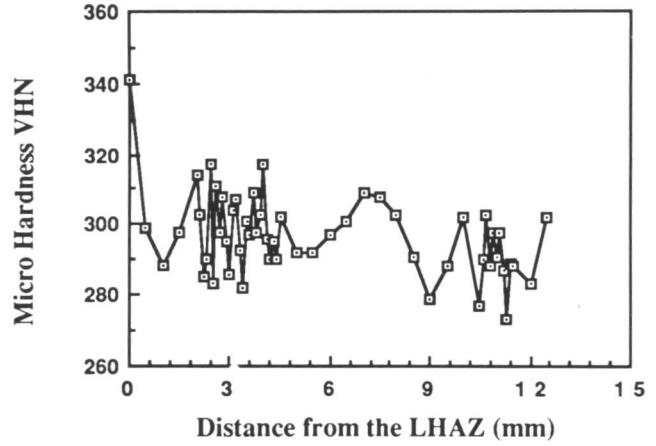

b

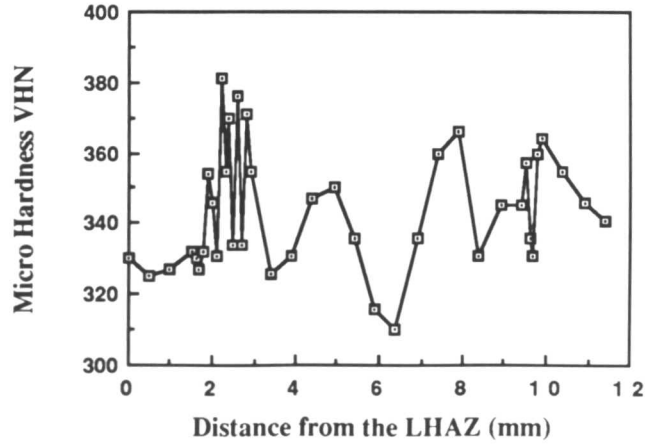

c

Fig. 5.14: Results of microhardness surveys carried out on:

(a) SP1 two-run weld, from the top to the root bead.

(b) SP1 two-run weld, across the heat affected zone.

(c) SP2 three-runs weld, across the heat affected zone.

Table 5.4: The measured mean Vickers microhardness of individual phases.

Material	Condition	Force (N)	VHN δ	VHN γ
WR4	As welded	0.981	283 ± 8	276 ± 4
WR4	As welded	0.4903	313 ± 7	309 ± 7
WR2	As welded	0.981	296 ± 10	260 ± 13
SP2	As welded	0.981	295 ± 9	289 ± 5
SP2	HAZ	0.981	284 ± 8	276 ± 7
SP1	As welded	0.4903	298 ± 14	308 ± 17

5.6 Inclusions

Due to their high oxygen content, weld metals usually contain a relatively large volume fraction of inclusions, mainly oxides, when compared with the wrought base plates. The number of inclusions has been shown to correlate with the oxygen content of the weld [4]. During electric arc welding of stainless steel, oxygen will enter the weld metal either from the electrode coating, *e.g.* the silicates contained therein, or by contact with the surrounding air when melting with a long arc. Welding under vacuum is not used widely, except in some cases with autogeneous electron beam welding.

The effect of inclusions on the mechanical properties has long been a subject of investigation and concern. It is believed that inclusions have a detrimental effect on the weld metal toughness [9] and fatigue strength when present in high fractions and large sizes on the one hand, but it is also clear that finely dispersed small inclusions are beneficial as they provide preferred intragranular nucleation sites for favourable phases such as acicular ferrite in HSLA steels [10,11,12]. Evidently, TiO_2 inclusions formed during welding have a beneficial effect on the toughness of the heat affected zone [13]. According to Folkhard [10,] the hot cracking resistance of stainless steel weld metals is not normally influenced in a detrimental way by its oxygen content, because the fine oxide inclusions of the main deoxidising agents, manganese and titanium, as well as the chromium, generally have little influence on the low melting phases responsible for such cracking. The mechanism by which inclusions influence the mechanical properties is still not fully understood. Inclusions in the weld metal BW were in the as welded condition observed to enhance the δ to γ solid state transformation. The TEM micrographs shown in Figs. 5.15, 5.16, provide clear evidence of the heterogeneous nucleation of austenite on inclusions. It is also believed that the stress field developed around the

inclusions during quenching of the weld metal provides additional nucleation sites for the austenite (*e.g.* dislocations).

Preliminary investigation of the chemical composition of the inclusions in the isothermally heat treated W111 weld metal suggests that the inclusions may enhance the formation of austenite by depleting the matrix around them of chromium and silicon, *i.e.* the inclusions contain a relatively high concentrations of Cr and Si (Fig. 5.17).

a

b

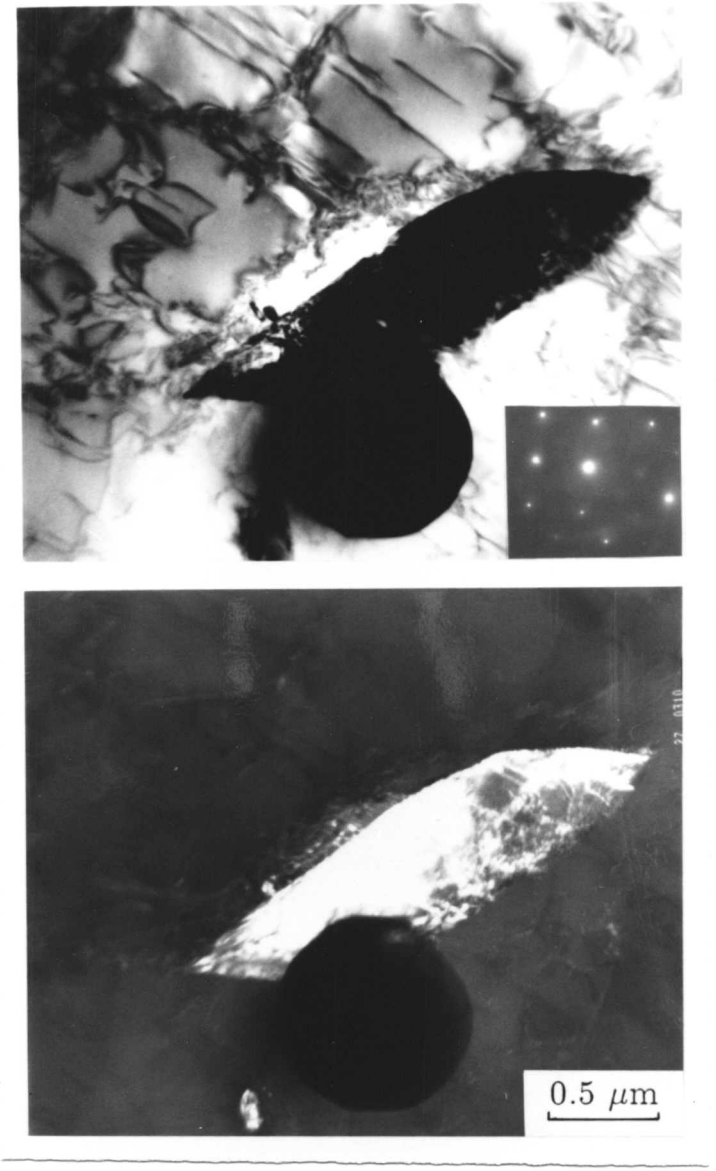

Fig. 5.15: Transmission electron microscope images showing the formation of an austenite particle on an inclusion in the as-welded layer of weld metal BW:

a) bright field image;

b) dark field image.

SADP zone axis $[\bar{2}33]_{\gamma}$.

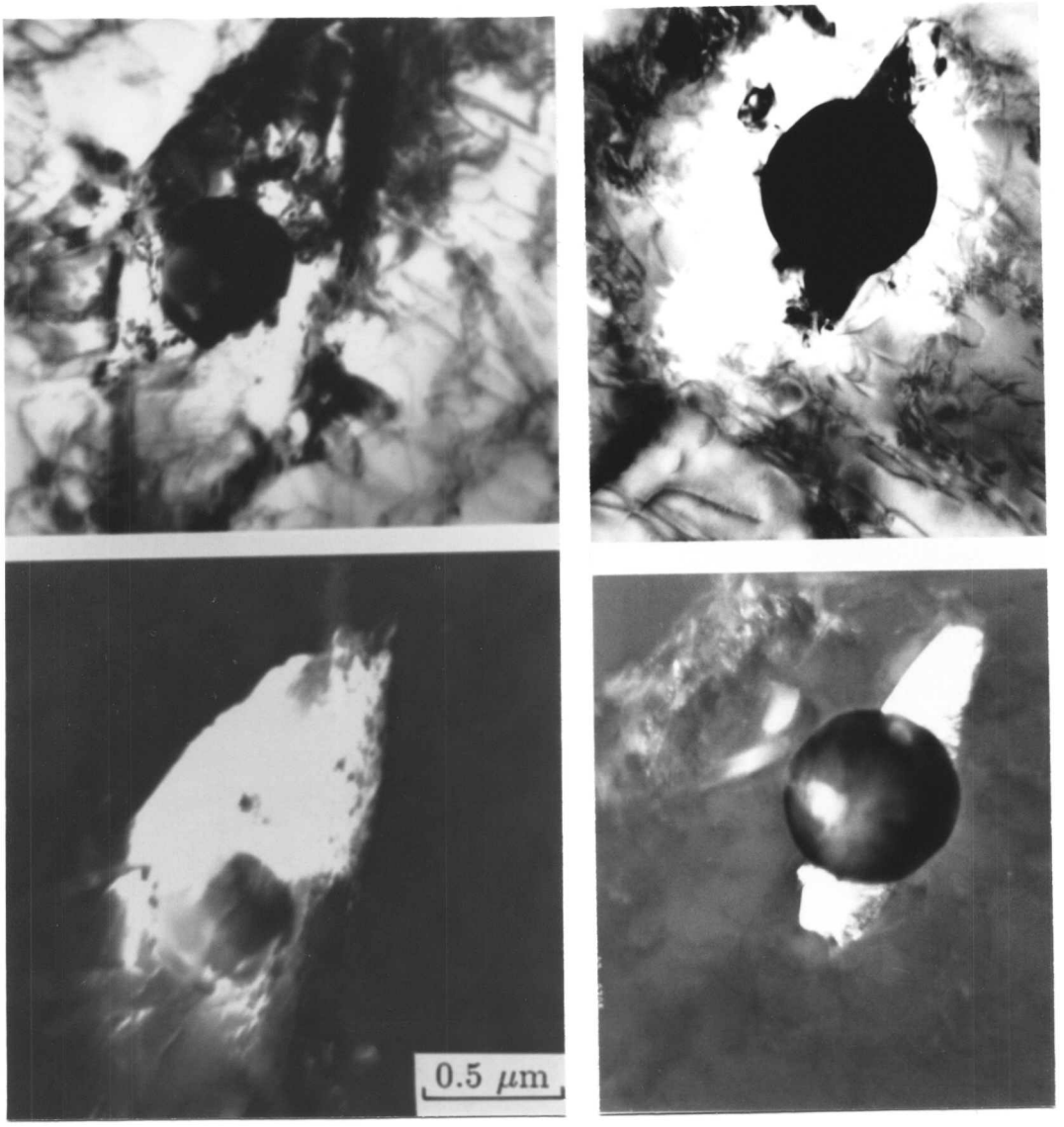

Fig. 5.16: Transmission electron microscope bright and dark field images showing the formation of austenite particles on inclusions in the as-welded layer of weld metal BW.

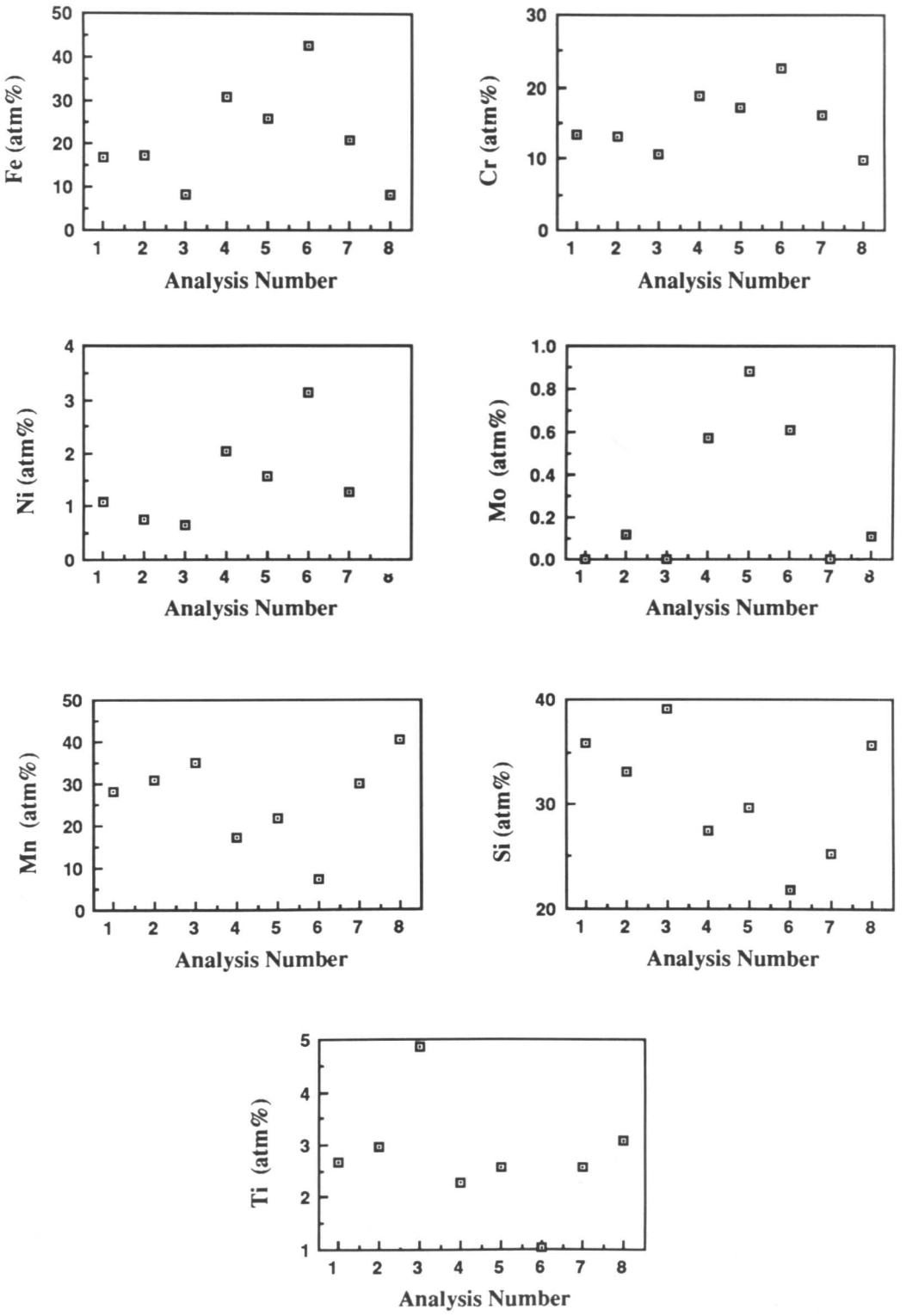

Fig. 5.17: Concentrations of substitutional solutes in inclusion as obtained from micro-analysis test carried out using the EDX microanalysis attached to a scanning electron microscope. The results shown ignore the presence of any interstitials. Standard errors (2σ) are: for Fe, Cr Mn and Si (± 0.5), for Ti and Mo (± 0.2).

5.7 Conclusions

(a) The primary crystallisation of duplex stainless steel welds and pads studied in this project occurs by epitaxial cellular growth of δ-ferrite from the solid base plate at the fusion surface. During cooling, a rapid solid state transformation of δ-ferrite to austenite takes place. The decomposition of δ starts at elevated temperatures, as high as 1200°C, depending on the chemical composition and the degree of undercooling. It begins with the formation of continuous thin layers of allotriomorphic austenite decorating the boundaries of the columnar δ grains. These δ grains were always observed to be continuous across the successive weld passes, emphasising the fact that δ exists at room temperature. From the allotriomorphic austenite a network of Widmanstätten austenite sideplates was observed to form, accounting for the biggest share of the total austenite content. Within the interior of the δ grains, "acicular" austenite is often found to nucleate intragranularly on non-metallic inclusions. In the as-deposited regions of the weld metal a large fraction of the acicular austenite is formed on inclusions. The reheated zones of the weld deposits have higher volume fractions of austenite compared with the as-deposited regions. The austenite particles in the reheated zones were found to have an almost equiaxed morphology.

(b) The heat affected zones in duplex stainless steels turn out to be rather narrow, consisting firstly of a grain growth zone characterised by coarse δ-ferrite grains decorated with allotriomoprhic layers of austenite, some austenite plates and some intragranularly nucleated particles formed on inclusions; the volume fraction of austenite in this region is low compared with the weld zone. Beyond this is the partially ferritised zone with a microstructure similar to that of the base plate, the major difference being the spacing of the grains which is a function of the distance from the fusion zone and the peak temperature reached during heating.

(c) The effect of the alloy chemistry on the volume fraction of the δ-ferrite as represented in the literature by the Schaeffler diagram and other compositional parameters, appears to provide an acceptable method for the estimation of microstructure in the as-deposited region of the weld zone, but not in the reheated or heat affected zones.

(d) The welding of duplex stainless steel to a dissimilar metal such as a carbon steel or austenitic stainless steel has the effect of diverting the solidification mode from

a completely δ-ferritic solidification mode to one in which it is partially ferritic or even to a primary austenitic mode, depending on the degree of dilution with the base plate. It also led to the formation of martensitic layers in the vicinity of the fusion surface and to ferrite morphologies other than those associated with a ferritic solidification. This in turn may have a negative effect on the susceptibility to hot cracking and on the mechanical properties of the welding joint.

(e) Microanalysis data revealed the existence of microsegregation across the top and root beads of the weld deposits. The interesting result is that substitutional alloying elements, except iron and molybdenum, did not appear to partition between the austenite and δ-ferrite phases. This may be attributed to the partitioning coefficient being close to unity or perhaps to kinetics reasons which need further investigation. The difficulty in interpreting the microanalysis data arises from the overlap between segregation occurring during solidification, and partitioning during solid state transformation.

(f) The hardness of the weld metal is found to be a function of the microstructural constituents of the microstructure. It increases with the δ-ferrite volume fraction.

(g) In the as-deposited layers of the welds, inclusions provide additional heterogeneous nucleation sites and enhance the formation of "acicular" austenite. The mechanism by which austenite forms on inclusions is not yet established.

References

1. Chart et. al., (1975) International Metallurgical Review, vol. **20**, p. 57.

2. Suutala, N., Takalo, T. and Mosio, T. (1979) Met. Trans., **10A**, p. 513.

3. Schaeffler, L. A. (1949) Metal Progress, **56**, p. 680.

4. Liu, S. and Olson, D. L., June (1986) Weld. J. Res. Suppl., Vol. **65**, No. 6, p. 139s.

5. Yang, J. R. and Bhadeshia, H. K. D. H. (1987) 'Advances in Welding Science and Technology', Conf. Proc. Ed. David, S. A., ASM, Ohio, p. 187.

6. Sato, K., and Terasaka, M. (1986) 'Proc. XIth Int. Cong. on Electron Microscopy' Kyoto , p. 1603.

7. Honeycombe, J. and Gooch, T. G. (1985) The Weld. Inst. Report 286/ 1985.

8 Wahlberg, G., Rolander, U. and Andren, H. O. (1987) Internal Report, Charlmers University of Technology.

9. Snyder J. P. and Pense, A. W., July (1982) Weld. J. Res. Suppl. Vol. **61**, No. 7, p. 201s.

10. Folkhard, E. 'Welding Metallurgy of Stainless Steels' (1988) Wien-New York, Springer-Verlag publishers, p. 47.

11. Abson et al., (1978) 'Trends in Steels and Consumables for Welding', Int. Conf. Proc., (The Weld. Inst., London), p. 75

12. Jang, J. and Indacochia, J. E. (1987) J. of Mat. Sci., **22**, p. 689.

13. Chijiiwa, R. et al. February, (1988) 7th Int. Conf. 'Offshore Mechanics and Arctic Engineering (OMAE)', Houston, Texas, USA.

Chapter 6

KINETICS AND METALLOGRAPHY OF THE δ-FERRITE TO AUSTENITE TRANSFORMATION IN DUPLEX STAINLESS STEEL WELDS

Since the $\delta \rightarrow \gamma$ solid state transformation plays a crucial role in determining the volume fraction of austenite at ambient temperature in duplex stainless weld metals, the emphasis in this chapter will be on this transformation under isothermal heating conditions. The kinetics of the $\delta \rightarrow \gamma$ reaction are believed to be very rapid, the reaction terminating in some duplex alloys in less than 100 seconds. As discussed earlier in chapter 2, the available overall transformation kinetics data for the $\delta \rightarrow \gamma$ transformation are not very extensive. Furthermore, the results are on occasion in dispute, especially as far as the start of the transformation is concerned, and in the details of the over all transformation kinetics. In this chapter, the behaviour of the $\delta \rightarrow \gamma$ reaction is approached using dilatometry, and an attempt is made to interpret the resulting data theoretically. The morphologies of the transformation products are investigated using optical and electron microscopy, and the overall volume fractions are analysed using a number of methods including image analysis, a lineal intercept method, X-ray and dilatometry.

6.1 Transformation Behaviour of DSS Wrought and Weld Alloys

The classification of microstructure purely on the basis of morphology can be very useful in establishing structure - property relationships on an empirical basis. In order to be able to predict the microstructure a detailed and quantitative understanding of the mechanism of transformation is needed. The aim here is to gather quantitative data on the transformation behaviour of duplex stainless steel base metal and also weld metal.

6.1.1 Isothermal dilatometry

Duplex stainless steel wrought metals SH, SHP and weld metals BW and WR4 were studied isothermally using dilatometry. To obtain the δ phase, specimens of alloy SH were solution treated at 1300°C for 5 min, whereas those of alloys BW and WR4 were ferritised at 1350°C for 5 min, since the higher nitrogen and nickel levels in the latter alloys cause some of the austenite to remain stable at temperatures beyond 1300°C.

It was found that alloy SHP, which contained Ni, Mo and Cr as the major alloying conditions, could be quenched from the single δ-ferrite phase field to ambient temperature without transformation. The δ-ferrite could therefore be retained by quenching to ambient temperature (Fig. 6.1). Consequently, the transformation to austenite could then be studied by rapidly heating the 100% retained δ-ferrite samples to the isothermal transformation temperature of interest. This could not be done with alloys SH, BW, and WR4, which due to their fast $\delta \rightarrow \gamma$ transformation kinetics, had to be transformed by quenching to the isothermal transformation temperature directly from the δ phase field (T_δ). The quenching was accomplished using a helium gas quench facility on the dilatometer.

To measure absolute length changes, the length sensitive device (transducer) was calibrated by measuring the expansion coefficients of pure nickel and platinum rods prior to the experiments. A typical form of the length and temperature data as monitored on the dilatometer during isothermal transformation is shown in Fig. 6.2. The isothermal transformation curves of relative length change as a function of time are shown in Fig. 6.3. The $\delta \rightarrow \gamma$ transformation is associated with a decrease in volume since the close-packed structure of austenite is relatively denser. The packing density of b.c.c. and f.c.c. crystal structures are 0.66 and 0.74 respectively in a hard sphere model.

For welds metal specimens BW and WR4 isothermally transformed at 900°C , the specimen dimensions were observed to increase after about 200 seconds of $\delta \rightarrow \gamma$ reaction. This is because of the intervention of σ phase reaction; its precipitation is expected to cause an expansion because of its lower density compared with that of ferrite and because the $\delta \rightarrow \gamma$ transformation is in these alloys expected to be completed after 200 seconds. In many cases, the transformation of $\delta \rightarrow \gamma$ in alloys BW, WR4, and SH was found to be extremely rapid; for alloys WR4 and BW some transformation occurred during the quench when the isothermal transformation temperature was less than 1000°C. It was therefore not possible to detect an "incubation" period experimentally for the construction of isothermal transformation diagrams. The temperature overshoot during quenching was in some cases large enough to conceal the transformation start time. These difficulties did not arise for alloy SHP, which

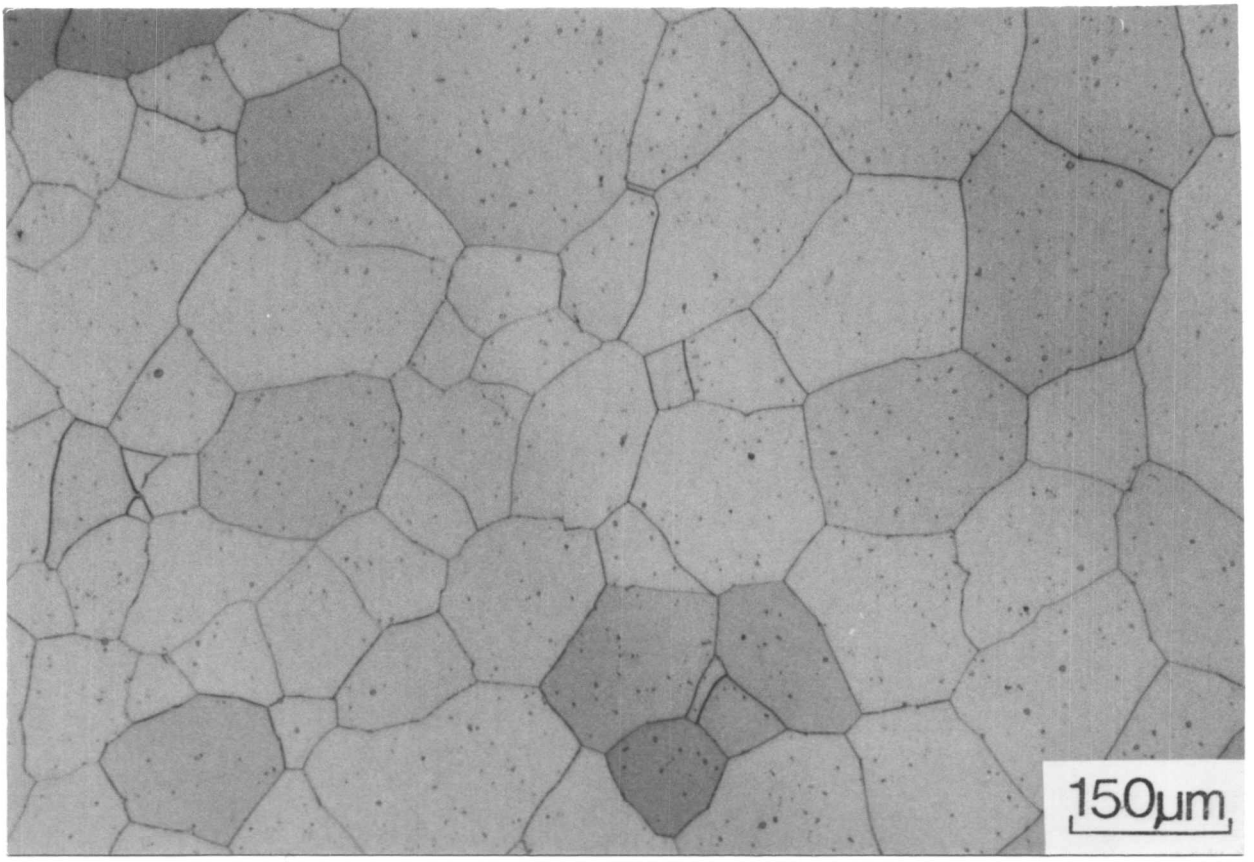

Fig. 6.1: Optical micrograph showing a fully ferritic microstructure obtained after quenching a solution treated sample of wrought alloy SHP ($T_\delta = 1150°C$).

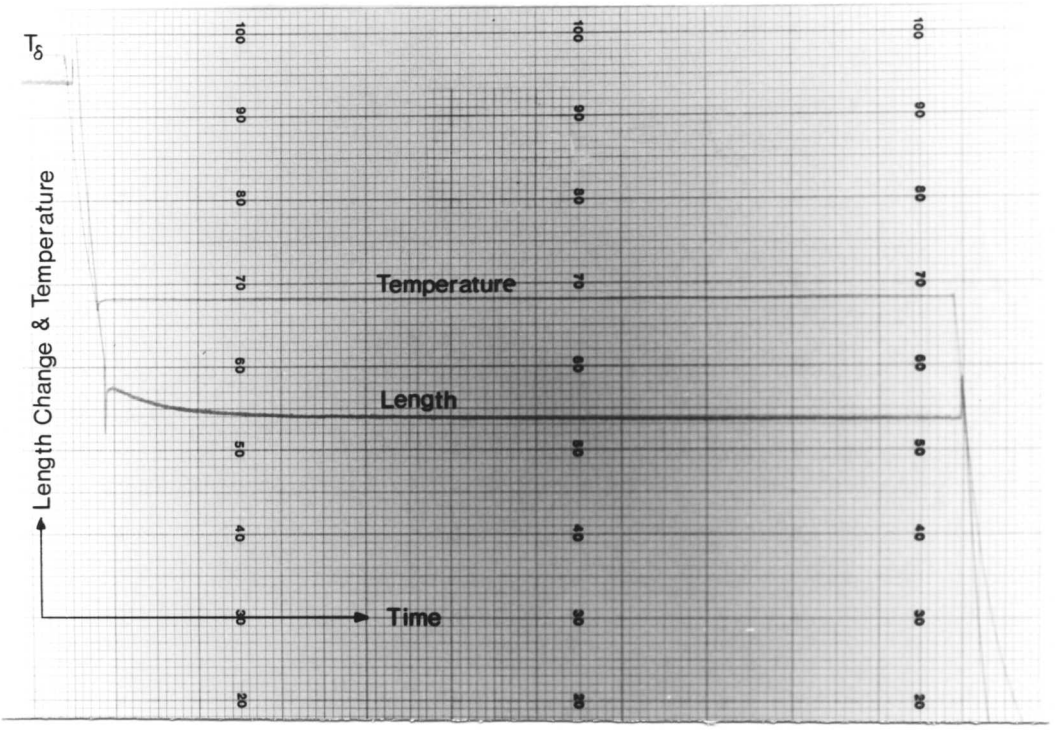

Fig. 6.2: Showing a typical form of length and temperature profiles, as monitored on the dilatometer during isothermal transformation of duplex stainless steel.

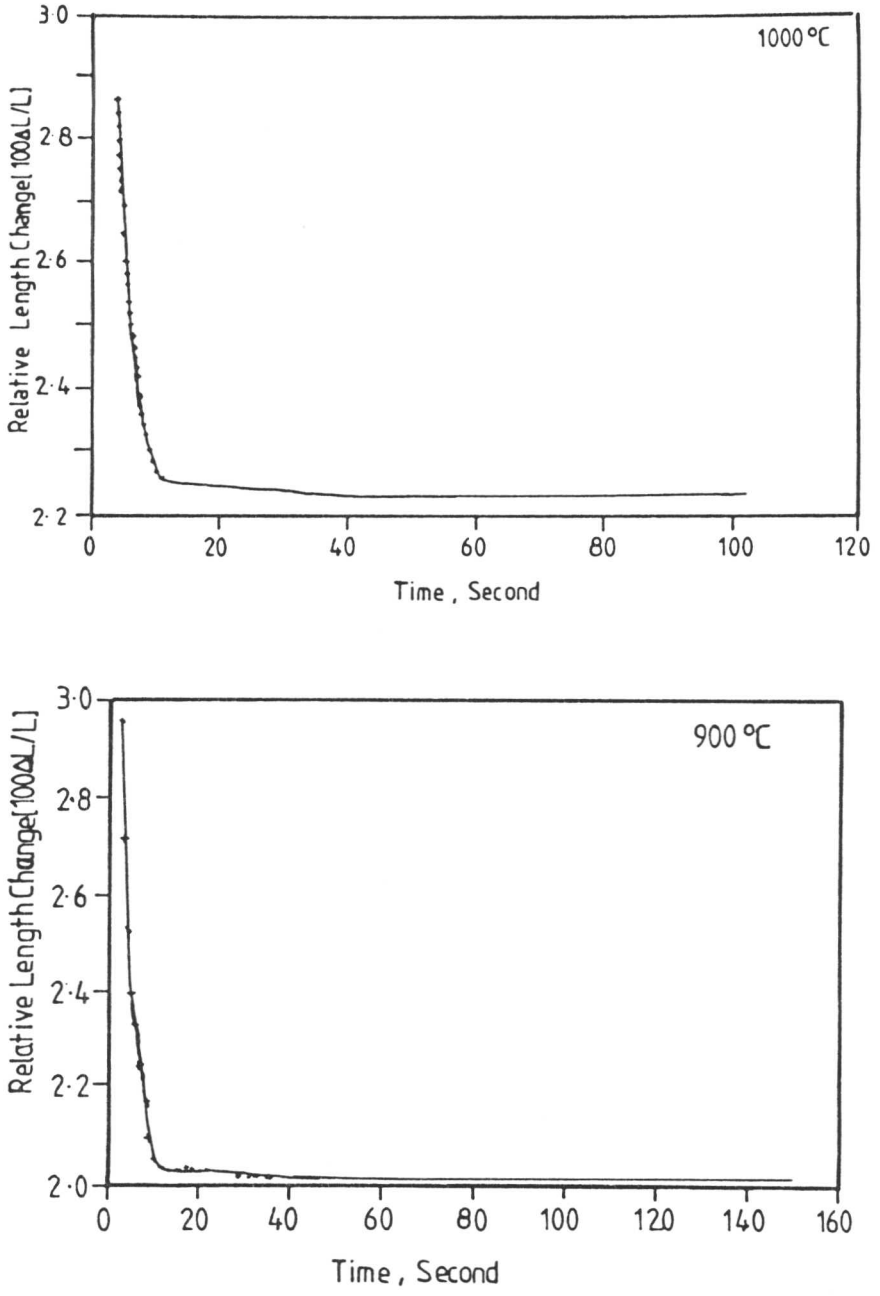

Fig. 6.3: Showing relative length change versus time profiles for isothermal transformation of alloy SH specimens at 1000 and 900°C, obtained using dilatometry. (T_δ = 1300°C, Ferritisation time = 5 mins.)

could be up-quenched to the isothermal transformation temperature it was possible to identify an incubation period for the 900 and 800°C transformation temperatures, as they were typically more than 100 seconds.

6.1.2 The Volume Fraction of Austenite

The major interest of this work is the prediction of microstructure in duplex stainless steel weld metals and particularly its austenite volume fraction. In this section, a formula for the calculation of the volume fraction of austenite at ambient temperature after isothermal heat treatment is derived, based on relative length change data obtained using dilatometry.

The following analysis of the volume fraction of austenite is carried out assuming that the composition of the product phase is the same as that of the parent, since most of the dimensional change is due to the change in crystal structure rather than the relatively small changes in lattice parameters due to composition change. For example, it can be estimated that a change as large as 5 wt% in the chromium concentration will only affect the typical calculated volume fraction of austenite by 4%. To do this calculation properly, it is necessary to be able to predict the composition of ferrite from first principles even if the transformation does not occur under equilibrium conditions. Nonequilibrium transformations are the rule rather than exception for weld deposits.

Irrespective of the transformation mechanism, for small changes, the relative length change $\frac{\Delta L}{L}$ will almost be equal to one third the relative volume change $\frac{\Delta V}{V}$.

$$\frac{\Delta L}{L} \simeq \frac{1}{3}\frac{\Delta V}{V}$$

The relative length change associated with the $\delta \rightarrow \gamma$ transformation is given by:

$$\frac{\Delta L}{L} = \frac{1}{3}\frac{[(1-V_\gamma){a_\delta}^3 + \frac{1}{2}V_\gamma {a_\gamma}^3] - {a_\delta}^3}{a_\delta^3}$$

$$V_\gamma = \frac{6a_\delta^3 \cdot \frac{\Delta L}{L}}{(a_\gamma^3 - 2a_\delta^3)} \tag{6.1}$$

where,

V_γ = volume fraction of austenite calculated for the isothermal transformation temperature.

$(1 - V_\gamma)$ = volume fraction of δ-ferrite.

a_δ = lattice parameter of δ-ferrite at the isothermal temperature.

a_γ = Lattice parameter of austenite at the isothermal temperature.

After making the appropriate substitutions, equation (6.1) can be solved to give the volume fraction of austenite at ambient temperature after isothermal transformation.

6.1.3 Lattice Parameters and Thermal Expansion Coefficients

In order to calculate the volume fraction of austenite by solving eq. (6.1), the thermal expansivities of δ and γ and their lattice parameters are needed. To determine the expansivities, a fully austenitic stainless steel and a fully ferritic experimental stainless steel (Fe-23Cr-3Mo wt%) specimens were heated from ambient temperature to about 1300°C at a heating rate of $8°Cs^{-1}$ and then cooled to ambient temperature at the same rate, using a dilatometer. The relative length versus temperature curves obtained showed that the expansivities of both δ, and γ, and particularly δ, are temperature dependent, Fig. 6.4. Third order polynomial equations were fitted to the experimental curves and the expansivities of δ and γ for the temperature range 200 to 1300°C were established as shown below:

$$e_\delta/°C^{-1} = 0.8839 \times 10^{-5} + 60.9698 \times 10^{-10}T - 327.52308 \times 10^{-15}T^2 \qquad (6.2)$$

$$e_\gamma/°C^{-1} = 1.507829 \times 10^{-5} + 104.45473 \times 10^{-10}T - 420.515 \times 10^{-14}T^2 \qquad (6.3)$$

where T is in °C.

Accordingly the lattice parameters of δ and γ as a function of temperature are given by:

$$a_\delta = a^\circ{}_\delta (1 + \int_{20}^{T} e_\delta \, dT) \qquad (6.4)$$

$$a_\gamma = a^\circ{}_\gamma (1 + \int_{20}^{T} e_\gamma \, dT) \qquad (6.5)$$

where a° is the (measured) lattice parameter of δ-ferrite or austenite at ambient temperature.

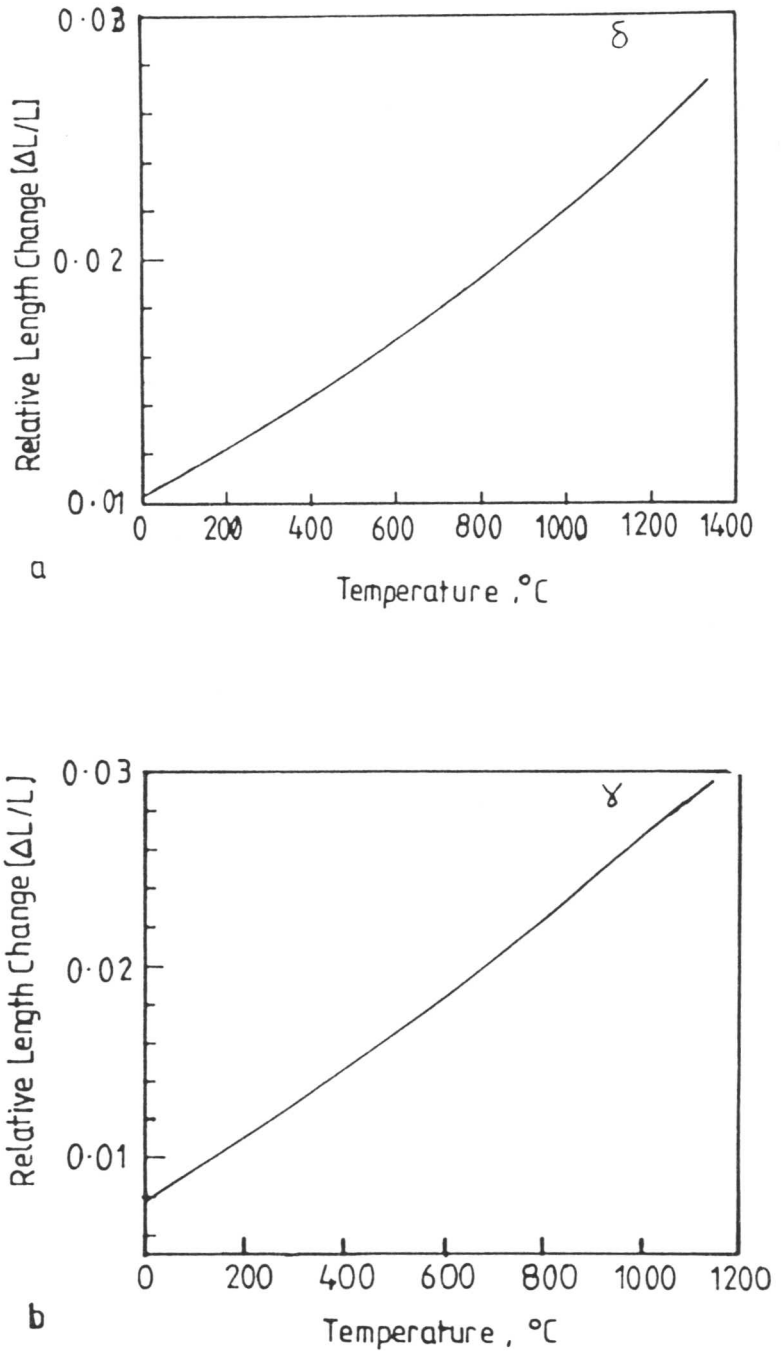

Fig. 6.4: Showing the graphs of relative length change versus temperature, from which expansivities were obtained as a function of temperature:

(a) for δ-ferrite,

(b) for austenite.

The ambient temperature lattice parameter measurements (using CuK_α and CrK_α radiation) were carried out using either a Debye Scherrer powder camera or a diffractometer. The experiments were carried out on a solution treated duplex stainless steel wrought alloy (SH) and welded alloys BW and W111. The specimens were chemically polished to remove any effects due to surface deformation before measurements. A least squares extrapolation method (Fig. 6.5), using the 011, 002, 112, 022, 013 peaks was used to obtain an accurate δ-ferrite lattice parameter. The lattice parameter of austenite a_γ° was taken from recent work [1] on Fe-Cr-Ni alloys, which also takes into account the effect of carbon and nitrogen. A computer program (Appendix 1) was written to solve eq. 6.1 with the appropriate substitutions to obtain the volume fraction of austenite V_γ at ambient temperature after isothermal treatment from the measured maximum length change (Fig. 6.6). Results are presented in Table 6.1, together with optical measurements of the volume fractions of austenite using the lineal intercept method. The correlation of dilatometric data with optically measured volume fractions was found to be satisfactory for temperatures between 800 and 1000°C. This was not the case for 1100°C possibly because of creep effects interfering with the transformation data at high temperatures. Nevertheless, the volume fractions measured using dilatometry is likely to be more accurate, since very fine austenite particles cannot be measured accurately by optical means.

6.1.4 Effect of Chemical Composition on Lattice Parameters

It has been assumed so far that the volume fraction of austenite can be calculated assuming composition invariant transformation. It is in fact likely that in many cases, alloying elements do partition during transformation, and any change in concentration can be expected to be reflected in a corresponding change in the lattice parameter. The effect of interstitials on the austenite lattice parameter was investigated recently by Ledbetter *et al.* [1] who found that the carbon and nitrogen effects on a_γ° can be represented by:

$$a_\gamma^\circ = 0.35866 + 0.000783X_C + 0.000861X_N \tag{6.6}$$

where X_C and X_N are in atomic %, and a_γ° is in nm.

The work of Ledbetter *et al.* was on austenitic stainless steels, and shows a larger effect of nitrogen than that of carbon on the a_γ°. The equation is a reasonable approximation

for the austenite lattice parameter in duplex stainless steels. Results of austenite lattice parameters measurements of some of the wrought and weld metals investigated in this project, using the powder diffraction method and diffractometer scanning are shown in Table 6.2.

Table 6.1: Measured volume fraction of austenite at ambient temperature after isothermal treatment.

Specimen	D* μm	T_δ (°C)	T_{iso} (°C)	$t_{T_{iso}}$ (mins)	V_γ L.I.	V_γ Dilat.
SH	220 ±17	1300	800	5	0.19 ± 0.038	0.17
SH	232 ±10	1300	900	5	0.24 ± 0.042	0.19
SH	227 ±15	1300	1000	5	0.19 ± 0.039	0.21
SH	195 ±13	1300	1100	5	0.06 ± 0.022	0.11
SH	600 ±23	1300	900	15	0.11 ± 0.031	0.12
SH	576 ±17	1300	900	60	0.28 ± 0.041	-
SH	621 ±19	1300	1000	60	0.09 ± 0.029	0.12
SH	545 ±29	1300	1100	60	0.02 ± 0.012	-
R4P	-	1250	800	15	-	0.33
R4P	-	1250	900	15	-	0.31
R4P	-	1250	1000	15	-	0.31

Where

T_{iso} = isothermal transformation temperature

D* = average grain size of primary δ measured by lineal intercept method

L.I. = lineal intercept

Dilat.= measured by dilatometry.

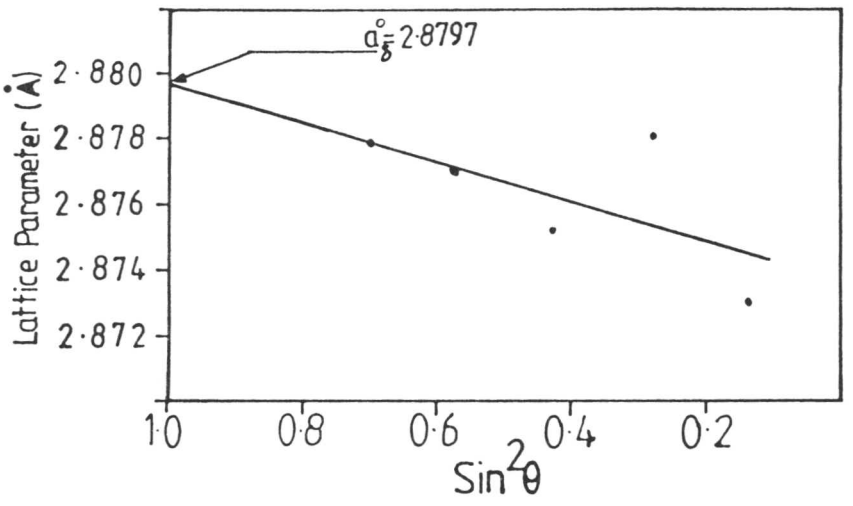

Fig. 6.5: Extrapolation of δ-ferrite lattice parameter against $\sin^2\theta$.

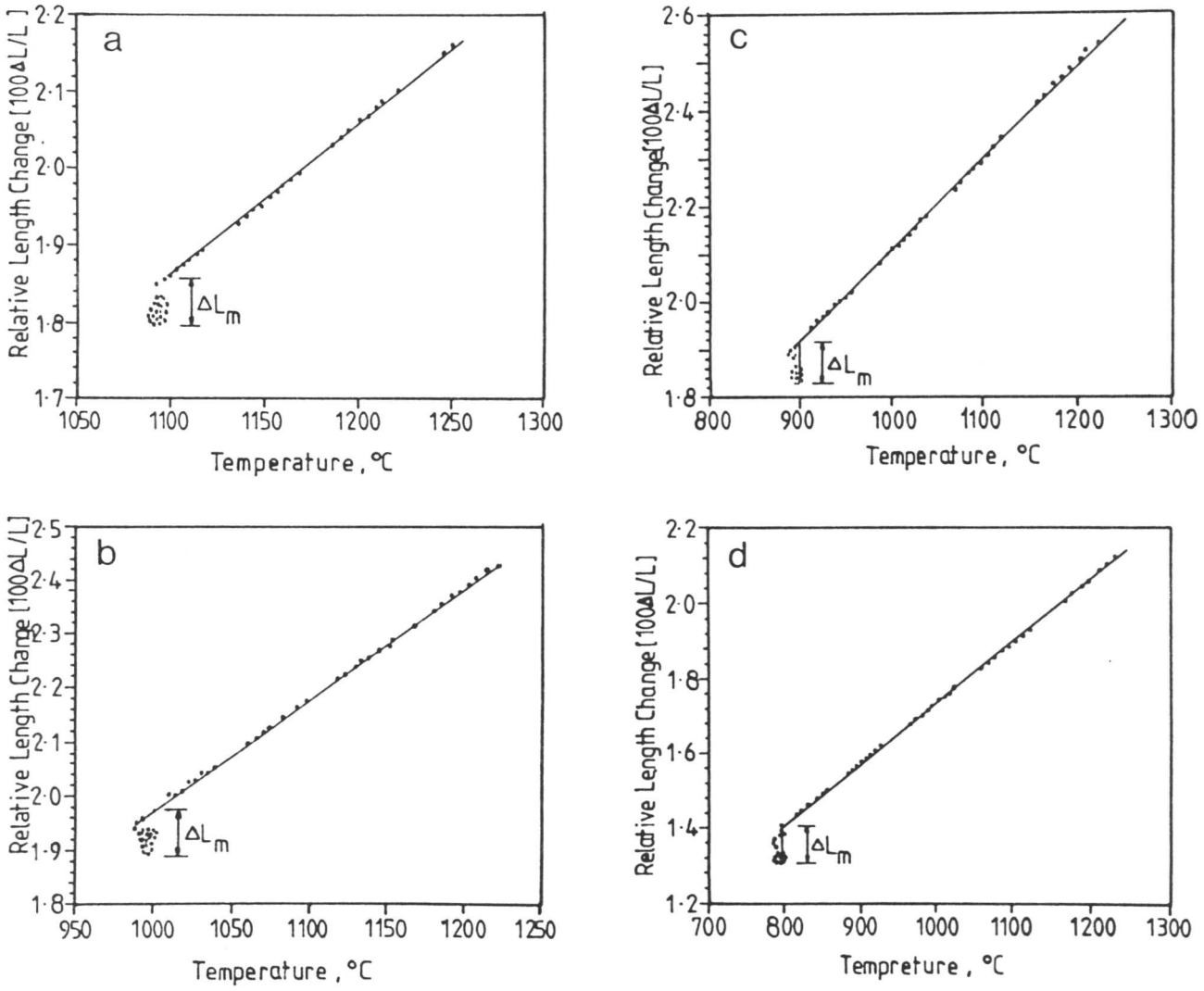

Fig. 6.6: The relative length change due to transformation as a function of temperature, for isothermal transformation of alloy SH at 1100 (a), 1000 (b), 900 (c) and 800°C (d) for 5 mins., obtained from dilatometric experiments. (T_δ = 1300°C, ferritisation time = 5 mins., ΔL_m = maximum relative length at the isothermal transformation temperature)

Table 6.2: Measured lattice parameters of δ and γ.

Material	a_γ° (nm)	a_δ° (nm)
SH	0.3600 ± 0.0018	0.2879 ± 0.0012
W111	0.3602 ± 0.0018	0.2873 ± 0.0014
BW	0.3600 ± 0.0013	0.2874 ± 0.0012

The lattice parameters of austenite as calculated according to equation 6.6 (a_γ^c) are shown in Table 6.3. A comparison of a_γ° with a_γ^c would show simply that equation 6.6 to some extent underestimate the austenite lattice parameter when calculated with the bulk concentrations of carbon and nitrogen of the duplex alloy. This result led us to consider a calculation of the lattice parameter of austenite using the equilibrium concentrations of interstitials carbon and nitrogen in the austenite at the solution treatment temperature (a_γ^{c*}). a_γ^{c*} compared with a_γ° gave a slightly better correlation. The small differences between the calculated and measured lattice parameters of austenite could possibly be due to an effect of substitutional alloying which still as yet not resolved in duplex stainless steel. Nevertheless, the equation used still provides reasonable estimates of the lattice parameters, within the limits of errors associated with the experimental technique.

Table 6.3: Calculated lattice parameter of austenite according to equation (6.6)

Material	C (atomic%)	N (atomic%)	a_γ^c (nm)	a_γ^{c*} (nm)
SH	0.138	0.248	0.3590	0.3593
BW	0.119	0.346	0.3591	0.3593
WR4	0.244	0.313	0.3592	0.3592

where,

a_γ^c is the calculated lattice parameter of austenite with bulk alloy concentration and

a_γ^{c*} is the calculated lattice parameter of austenite with equilibrium interstitials concentrations at the solution treatment temperature.

6.2 Isothermal Transformation Diagrams

Isothermal transformation diagrams of the volume fraction of austenite versus time for different transformation temperatures were constructed, to illustrate the course of the $\delta \rightarrow \gamma$ transformation. The computer program used to calculate the maximum volume fraction of austenite from the maximum measured relative length change, was modified to calculate the volume fraction for each time interval from the difference in the relative length change as time progressed. The problem which was faced in doing this was that the incubation time as mentioned earlier often could not be detected because of the very fast $\delta \rightarrow \gamma$ reaction, especially with the weld metals. It was then difficult to determine the value of the reference point from which successive relative length values, corresponding to each time increment, could be measured. An approximation was made, as shown in Fig. 6.7, by taking the point of intersection of the straight line representing the quench from T_δ to the isothermal temperature, and a vertical line passing through the isothermal temperature in a relative length versus temperature diagram, as the reference point before the start of reaction. The time at which the isothermal temperature was attained was taken as the reference time. For the SHP (wrought steel), for which a reliable incubation time could be obtained, that time was taken as the reference time and its corresponding relative length change was taken as the reference length l_o.

6.2.1 Isothermal Transformation Diagrams for Alloy BW

An isothermal transformation diagram of the volume fraction of austenite as a function of time is presented in Fig. 6.8. The samples were ferritised from the initial welded condition and then directly isothermally transformed at the required temperature as described previously. The tests were carried out for the temperatures 800, 900, 1000, and 1100°C. The results suggest a C-curve behaviour for the $\delta \rightarrow \gamma$ transformation in duplex stainless steel weld BW, with the "nose" of the curve being at about 900°C. The reaction kinetics were found to be very fast and the transformation terminated after about 90 seconds at 900°C and about 120 seconds at 1000°C without even reaching completion. As expected, the maximum volume fraction of austenite obtained was found to increase with decreasing isothermal temperature except for transformation at 900°C . At the even lower transformation temperature of 800°C, the reactions seemed to occur in two stages, an initial rapid reaction followed by a temporary lull and then further reaction leading to austenite formation. This may be attributed

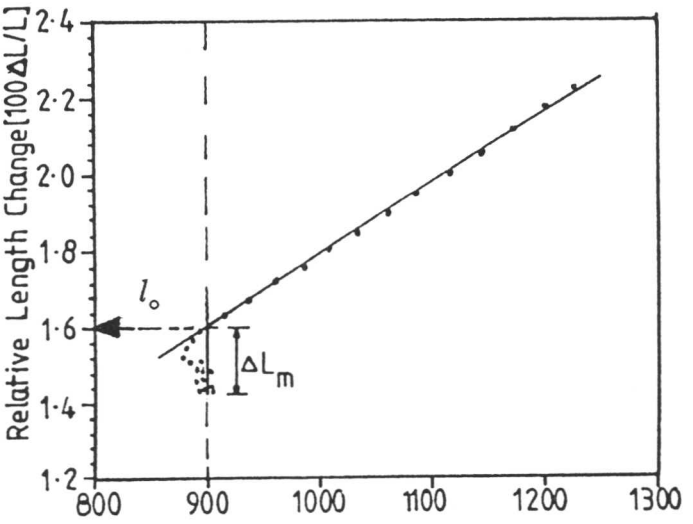

Fig. 6.7: Showing the method for the determination of l_o from a relative length versus temperature profile recorded dilatometrically, as the point of intersection of a straight line representing the quench from T_δ to the isothermal temperature, and a vertical line passing through the isothermal temperature.

a

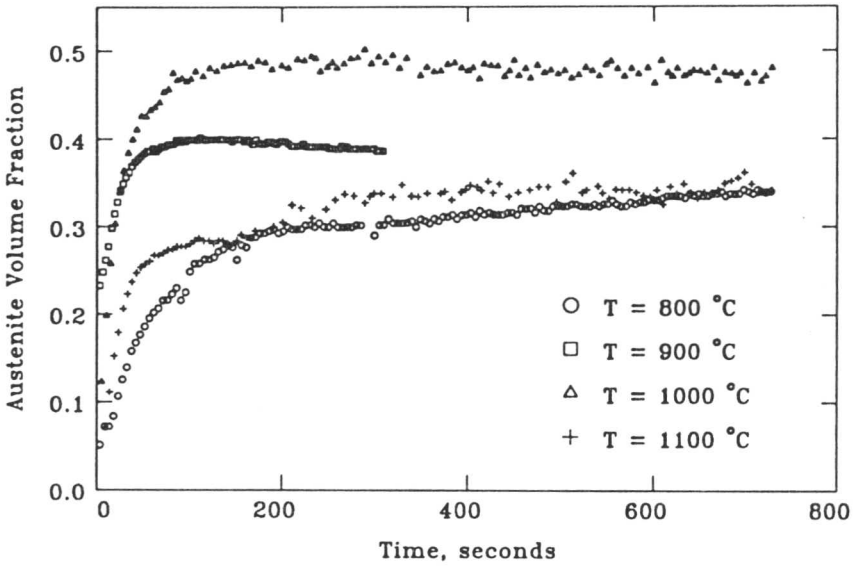

b

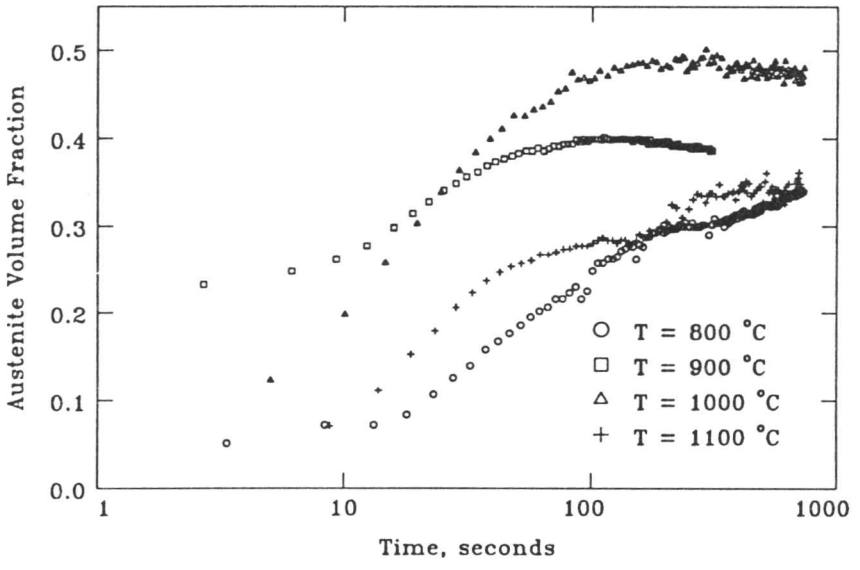

Fig. 6.8: Showing isothermal transformation diagrams of the volume fraction of austenite as calculated from the measured length change, obtained from dilatometric experiments, versus $\delta \rightarrow \gamma$ reaction time, for samples of welded alloy BW.
(a) reaction time, linear scale; (b) reaction time, log scale.

to the existence of two separate C-curves for the two different morphologies of austenite observed, the details of which will be discussed later. The $\delta \rightarrow \gamma$ did not seem to terminate after 1000 seconds of reaction at 800°C.

6.2.2 Metallography of Alloy BW after Isothermal Transformation

Over the whole of the temperature range studied, the $\delta \rightarrow \gamma$ transformation started with the formation of allotriomorphic austenite (γ_a) at the δ/δ grain boundaries, followed by the nucleation and growth of secondary Widmanstätten austenite (γ_w) from the austenite allotriomorphs. Intragranularly nucleated austenite (γ_{intra}) was also observed within the interior of the coarse ($\approx 300\mu$m grain size) δ grains. The dominant morphology at 1100 and 1000°C was the secondary γ_w which is believed to have formed intergranularly. The cross sections of the Widmanstätten austenite sideplates were found to be between parallelpiped and irregular shapes with faceted interfaces as illustrated in Figs. 6.9 & 6.10. The rate of transformation at 1000°C was found to be faster, giving a higher volume fraction of austenite after a 1000 seconds of reaction. At 900°C, the γ_a layers formed at the δ/δ boundaries were thinner, non-uniform and discontinuous (Fig. 6.11). σ phase was observed to form on the δ/γ boundaries at the expense of the δ-ferrite, its preferred nucleation site being the original δ/δ boundaries. It also formed intragranularly at the δ/γ boundaries of the larger austenite particles as illustrated in Fig. 6.11. The maximum volume fraction of austenite after 1000 seconds of reaction was found to be less than that observed after transformation at 1000°C.

At 800°C the amount of the Widmanstätten austenite was less than that observed at the higher isothermal temperature, and the plates tended to be shorter in length for the same reaction time. The dominant phase was intragranularly nucleated austenite. Two morphologies of the intragranular austenite were observed, one coarse with irregular shape, and the other fine but having a rod like morphology (Fig. 6.12). This may explain the two stage reaction isothermal diagram discussed in the previous section. σ phase precipitation was also observed at this isothermal temperature.

The microstructure of a specimen isothermally transformed at 700°C (Fig. 6.13), displayed clearly the difference between the parallelpiped cross sections of the Widmanstätten austenite and the fine plates of "acicular" austenite. The dominant morphology observed after transformation at this temperature was the intragranular austenite. The higher volume fraction of Widmanstätten austenite observed in comparison